Establishment of Soft-Landing Isolation Technique for Gas-Phase Synthesized Clusters in Organic Monolayer Matrices

A Dissertation Submitted to Keio University in
Partial Fulfillment of the Requirement for
the Degree of Doctor of Philosophy

Fiscal Year 2008

Shuhei Nagaoka

Acknowledgement

The research presented in this dissertation is the author's work which was performed at Nakajima laboratory in the Department of Chemistry, Faculty of Science and Technology, Keio University.

First of all, the author would like to express his deepest gratitude to Professor Atsushi Nakajima for the useful discussions, and the continuing support and kind guidance during the author's five years at Nakajima Laboratory.

Next, the author would like to acknowledge Professor Satoshi Yabushita, Professor Kimihisa Yamamoto, and Associate Professor Yasuaki Einaga for taking the time for the discussion and to review the early drafts of this dissertation.

Thirdly, the author would like to give his thanks to Associate Professor Masaaki Mitsui for the useful discussions and kind guidance during the author's five years at Nakajima Laboratory.

The author also express his appreciate to Professor Hiroshi Onishi for his suggestion regarding surface science technique, and Professor Uzi Even for his great helps for designing a mass spectrometer system. The author is also very grateful to Mr. Ken-ichirou Inoue, Shingo Doi, Eiji Okada, Takeshi Matsumoto, and Ms. Kaori Ikemoto for sharing experiment times pleasantly and for their great helps during the present work, and to all the member in the Physical Chemistry Research Group of Professor Nakajima and Professor Yabushita for their kindness and cooperation. For having grand time together during the life as a researcher and as an academic student, the author would like to thank Ph. D candidates, class of 20th of Department Chemistry, and all the friends of Keio Academy.

Finally, the author would like to express his wholehearted gratefulness to his parents and sister for continuous support and hearty encouragement.

This work is partly supported by the 21st Century COE program "KEIO LCC" from the Ministry of Education, Culture, Sports, Science, and Technology, and the author expresses his gratitude to research fellowship from Japan Society for the Promotion of Science for Young Scientist.

Yokohama, Japan

February 2008

Shuhei Nagaoka

Contents

CHAPTER 1

General Introduction

Gas-Phase Chemistry

Chemistry; it is defined in Oxford dictionary as the scientific study of the structure of substances, how they react when combined or in contact with one another, and they behave under different conditions. By another of saying, the author defines chemistry that the branch of science to understand *movement of electrons* in aggregate of atoms, which is interacting with photon, electron, and other aggregates. The aggregates include atoms, molecules, clusters, and their assemblies, i.e. gas, liquid, and solid-state matter. For instance, chemical reaction of two aggregates can be realized in the course of electron transfer between the aggregates, and the functionality (e.g. optical or magnetic response) of substances can be determined by electronic behavior after the interaction with photon or perturbation of magnetic filed. Thus, understanding of the movement of electrons reaches fruition of fine-control of chemical reaction process as well as chemical property and functionality of substances, which are ultimate goals of chemistry.

The movement of electrons or particles in atomic scale is described by quantum theory which freshman in department of chemistry will first study among the other chemistry classes. Historically, chemistry has been developed experimentally with the study of solution-phase reactions. It is, unfortunately, disconsolate to fundamentally understand the electronic movement of chemical reaction in solution phase because the reaction system is excessively complicated due to the environmental factors of solvent molecules.

Over the three decades, development in vacuum technology opens up new possibility to research chemistry in gas phase. Elemental chemical reaction and dynamics free from environmental factors have been finely understood in gas phase so far as represented by Nobel Prize for D. R. Herschbach, Y. T. Lee, and J. C. Polanyi in 1986. Thus, the gas-phase chemistry provides an opportunity to look at the substance of chemistry, i.e. electronic

movements and dynamics during chemical reactions.

Advent of Functional Clusters

With the development of laser-vaporization technique and molecular beam method, various kinds of materials assembled from finite-sized clusters were generated in a gas phase. So far, numerous experimental and theoretical studies have unveiled that the gas-phase synthesized clusters possess novel size-specific properties, which are distinctly different from those of corresponding bulk materials.

In many cases, gas-phase clusters show surprising geometric structure, which have the ability to generate unusual physical and chemical properties unrealizable in the condensed-phase materials. Functionality of materials will be, as noted above, largely governed by electronic structure and movement in the substances. Moreover, movements of the negative-charged electrons are certainly dictated by placement of positive-charged nucleus in the potential field. Thus, geometric structure (i.e. nuclear configuration) most likely affects the functionality of the substance so that the novel structures of the gas-phase clusters have the potential to exhibit unprecedented functionalities.

In 1985, Smalley and co-workers discovered a remarkably stable cluster consisting of 60 carbon atoms, a so-called "Buckminster-fullerene", in a mass spectrum, which is obtained after supersonic expansion of laser-vaporized carbon species.[1,2] The C_{60} forms an unique football-shape truncated icosahedral structure, i.e. a polygon with 60 vertices and 32 faces, 12 of which are pentagonal and 20 hexagonal, and 60 carbon atoms are placed at each vertex of this structure. This unfamiliar truncated icosahedral structure has not been confirmed in a bulk carbon material, and is, of course, different from crystal architecture in the other carbon allotrope of diamonds and/or graphite. The novel structures of gas-phase synthesized

clusters are also founded in a series of metal elements; for instance, a tetrahedral geometry (pyramid shape) of a 20-atom gold cluster (Au_{20}) was uncovered by Wang and co-workers.[3] While a closed electron configuration with a large energy gap between the highest occupied molecular orbital (HOMO) and the lowest unoccupied molecular orbital (LUMO) is a prerequisite for chemical stability of a cluster, Au_{20} has an extremely large energy gap, which is even greater than that of C_{60}. Such highly stable gas-phase clusters are expected to possess novel chemical and physical properties so that they have been regarded as promising building blocks for application of nanostrucured cluster-based functional materials.

One of the advantages of the gas-phase synthetic procedure is exclusion of environmental factors such as counter ions and solvent molecules. Therefore, the gas-phase can be useful chemical reaction field to synthesize unprecedented chemical compounds that is not proficiently produced by solution-phase conventional chemical technique. Over the past decade, chemical reaction of laser-vaporized metal atoms with organic molecules in a molecular beam has produced a wide variety of novel organometallic complexes in the gas phase. In 1994, Kaya and co-workers produced complexes of vanadium (V) atoms with benzene molecules in the gas-phase, and they found the magic numbered behavior of $V_n(benzene)_{n+1}$ (n = 1–5) which implies that the V–benzene complex forms multiple-decker sandwich structure, where metal atoms and benzene molecules are alternatively stacked in a one-dimensional fashion.[4,5] After that time, the formation of the one-dimensional multiple-decker sandwich structure of the V–benzene complexes was evidently confirmed by ion mobility measurement by Bowers and co-workers.[6] Furthermore, Kurikawa *et al.* studied the reaction of a series of 3d-transition metals (M = Sc–Ni) with benzene molecules.[7] They found the multiple-decker sandwich structure for the early transition metals of M = Sc, Ti, and V, and a rice ball structure, where benzene molecules cover the central metal cluster,

for the late transition metals of M = Fe, Co, and Ni. After the discovery of these uniquely structured $M_n(benzene)_m$ complexes, a wide variety of experimental and theoretical efforts have been devoted to their characterization.

In the case of $V_n(benzene)_{n+1}$ sandwich complexes, for instance, it has been found that they possess a quasi-band electronic structure, as a result, the ionization energies of the sandwich complexes drastically decrease with growth of their size. Furthermore, it has been recently demonstrated that $M_n(benzene)_{n+1}$ complexes have unique size-dependent ferromagnetic properties.[8,9] For $Sc_n(benzene)_{n+1}$ and $V_n(benzene)_{n+1}$ complexes, the magnetic moments increase monotonically with the cluster size, and the ground electronic state of $Ti_2(benzene)_3$ complex has been reported as quintet. Hence, it is anticipated that they become one of the most promising candidates for use as building blocks in nanoscale spintronic devices.

Chemistry and Physics of Clusters at Surfaces

In order to utilize the fascinating clusters for the nanostructured functional materials, it is absolutely imperative to extract the clusters isolated in gas phase onto/into a suitable media. Since the clusters possess size-specific properties, the extraction via mass selection of gas-phase clusters is also required to effectively exploit their abilities for the functional materials.

In 1997, Heiz *et al.* presented an innovative scientific instrument,[10,11] which provides nondissociative deposition of mass-selected cluster ions produced in the gas-phase onto a pertinent substrate, a so-called soft-landing apparatus. Surface modification via soft-landing of gas-phase clusters is expected to be one of the emerging approaches in designing novel cluster-based materials with desirable properties. Thus, with the advent of the soft-landing

technique, physical properties and chemical reactivity of the gas-phase synthesized clusters supported on solid surfaces have been extensively investigated over the past decade.

Research on catalytic properties of metal clusters soft-landed on metal-oxide surfaces has currently become one of the most active scientific fields since the discovery of catalytic activity of gold clusters supported on a magnesia surface. [10–13] In contrast to the inert nature of gold as bulk material, Haruta and co-worker have found that nanosize particles of gold supported on various oxides exhibit an enhanced catalytic activity, in particular for the low temperature oxidation of carbon monoxide (CO) in the late 1980s.[14] By use of soft-landing technique, Heiz and co-worker examined the catalyzed combustion of CO on size-selected gold clusters, Au_n ($n \leq 20$), supported on a magnesia (MgO) surface for the first time. They discovered that size-dependent catalytic activity of Au_n/MgO for CO oxidation, and found that Au_8 is the smallest catalytically active size. A charging of the metal cluster, caused by the partial transfer of charge from an F-center of the surface into the deposited cluster, underlies the catalytic activity of the Au_8 clusters. The F-centers further serve to strongly anchor the deposited clusters, thereby effectively inhibiting their diffusion and coalescence on the surface. They further demonstrated that the catalytic activity could be changed by impurity doping into the supported gold clusters, i.e. modification of their electronic structure through incorporation of judiciously chosen impurity atoms in otherwise inert clusters. These results provides evidence that the clusters possess novel size-specific and composition-dependent properties even supported on a solid surface, and these supported clusters have the capacity to be applied for nanoscale functional materials.

Recently, micromechanical sensor for studying thermodynamics of catalytic processes on size-selected clusters at surfaces has been developed by Antonitti *et al.*.[22] They use the micromechanical bimetallic cantilevers as the transducers of a calorimeter in order to

supersensitively detect heats of the surface reaction. As a result, a minimum power of 120 nW is measurable with a submillisecond response time, corresponding to a limit detection in the femtojoule range. Using this high sensitive micromechanical sensor, they have successfully extracted the reaction heats of catalytic processes on clusters supported on an oxide surface as well as information on the heat release during the cluster deposition time.

Understanding of optical properties and magnetic response of the clusters anchored on surfaces has been devoted in a frontier of the research in creation of new cluster-based materials. There is fundamental and technological interest in the optical and magnetic response of clusters, evolution of the properties with size, and possible use of these nanosystems as optically and photochemically active materials as well as nanoscale spintronic devices. However, extremely sensitive spectroscopic tool is required to investigate the electronic structure and magnetic response of the size-selected, supported clusters and nanoparticles. Indeed, the preparation of monodispersed samples requires low concentrations ($< 5 \times 10^{13}$ sites/cm^2) of clusters or nanoparticles to keep them well separated and to avoid aggregations on the surface. The conventional electron spectroscopy, e.g. ultraviolet and/or X-ray photoemission spectroscopy (UPS, XPS) and electron-energy-loss spectroscopy (EELS), mostly used in surface science researches will be at the limit of detection under such low coverage. Thus, new development of high-sensitive spectroscopy is highly desired so as to elucidate the optical and magnetic behavior of the supported clusters.

Recently, optical absorption spectra of gold atom and dimers on amorphous silica (SiO_2) obtained by use of cavity ringdown spectroscopy (CRDS) in the visible range.[23,24] Use of CRDS, which is one of the most extremely sensitive spectroscopic tools to obtain optical absorption spectra, makes possible to study optical properties of highly dispersed clusters at

surface coverages as low as 10^{11} particles/cm^2 order. Schütz and co-worker, on the other hand, measured photoelectron spectra of platinum atom and clusters soft-landed on a graphite surface by use of a synchrotron radiation source.[25] They demonstrated the change in core-level electron binding energy of supported Pt atoms and clusters with respect to that at bulk platinum, which presumably induced by considerable cluster-surface interactions.

The availability of synchrotron radiation source has given a chance to magnetic properties of the supported clusters. In free cluster beams (gas-phase clusters), the magnetic moments of size-selected clusters have been clarified in Stern-Gerlach experiments, which cannot be, however, applied in the field of surface science and solid-state matter. The high-intensity X-ray radiation source with variable photon energy and polarization enables the X-ray magnetic circular dichroism (XMCD) measurements, which are, recently, extendedly devoted to characterize the orbital and spin moments in magnetic clusters supported on the surfaces.[26-31]

On a related note, the adsorption properties of 1D organometallic sandwich complexes on metal surfaces have been studied by physical vapor deposition onto the surface under ultra-high vacuum (UHV) conditions.[17-19] In strong contrast to the supported metal clusters, organometallic clusters are considered to be rather unstable with respect to bare metal surfaces. Indeed, Blass *et al.* demonstrated that a Cr(benzene)$_2$ sandwich complex chemisorbed on a Ni(100) surface dissociates its ligand–metal bond due to a strong perturbation from the Ni(100) surface.[18] Thus, to support organometallic complexes on a substrate, the use of chemically inert substrate is required to reduce such metal surface perturbations. However, a study of the adsorption of ferrocene, Fe(C_5H_5)$_2$, on a relatively inert Ag(100) surface showed that ferrocene adsorbs molecularly on an Ag(100) surface, but the weak adsorbate–surface interaction permits the thermal desorption of the adsorbed

ferrocene at temperatures as low as 200 K. This desorption occurs because of the small desorption activation energy (or adsorption heat).[19] Therefore, ingenious cluster-supporting substrates or matrices, realizing both a small structural perturbation (i.e. maintenance of the sandwich structure) and a high adsorption heat (i.e. a high desorption temperature) of the supported organometallic sandwich clusters, are highly desired to research the physics and chemistry of the *intact* organometallic complexes at surfaces, and also to accomplish their application for the functional materials .

Organic Surfaces: Progress and Applications

Bare surface of metals and metal oxides tend to be adsorbed adventitious organic materials readily because these adsorbates makes the free energy of the interface between the metals or metal oxides and the ambient environment lower. These adsorbates also alter interfacial properties and can have a significant influence on the stability of surfaces of the metals and metal oxides, i.e. the organic material can act as a physical or electrostatic barriers to decrease the reactivity of the surface atoms. Thus, the organic surface provided by adsorption of organic materials on the metal and metal oxide surfaces is attractive alternative target to support chemically reactive and/or thermally unstable clusters such as organometallic complexes.

Self-assembled monolayers (SAMs) provide a convenient, flexible, and simple system with which to tailor the interfacial properties of metals, metal oxides, and semiconductor. SAMs are organic assemblies formed by the adsorption of molecular constituents from solution or gas phase onto the surface of solids; the adsorbates organize spontaneously into crystalline or semicrystalline structures. The molecules and ligands that form SAMs have a chemical functionality (or headgroup) with a specific affinity for a substrate; in many cases,

the headgroup also has a high affinity for the surface and displaces adsorbed adventitious organic materials from the surface. There are number of headgroup that bind to specific metals, metal oxides, and semiconductors. The most extensive studied class of SAMs is derived from the adsorption of alkanethiols on gold, silver, copper, palladium, and platinum. The high affinity of thiols for the surfaces of noble and coinage metals make it possible to generate well-defined organic surfaces with useful and highly alterable chemical functionalities displayed at the exposed interface.

Recently, Cooks and co-workers have described a technique to support gas-phase ionic species on a solid surface.[20] They have achieved trapping of gas-phase polyatomic ions using a SAM of fluorocarbon as the supporting matrix. They have also shown that the soft-landed bulky polyatomic ions can penetrate into the SAM and they are sterically trapped inside the SAM, while retaining their charge. Another important ability of the SAM has been demonstrated, in that it can serve as a effective buffer layer like a rare gas matrix, dissipating the kinetic energy of the projectiles. For example, Day *et al.* have performed a detailed study of a rare gas collision with *n*-alkanethiolate SAMs and found that the long-chain alkanethiolate SAM effectively dissipates the translational energy of the projectile atom.[21] They estimated that more than 80% of the incident energy of the projectiles transferred to internal energy of the organic surface. Based upon the above-mentioned results, SAMs are likely to be promising matrixes to suppress the dissociation of the clusters in the soft-landing process and to realize the effective trapping of intact clusters.

Scope and Organization of the Thesis

The aim of this work is establishment of new type of matrix-isolation technique, which realizes the supporting of the gas-phase synthesized clusters on the substrate with remaining

their native structure intact as well as high thermal stability. Nondissociative deposition of gas-phase clusters onto a solid surface is indeed successfully performed by soft-landing technique, nonetheless, the structural changes of the soft-landed clusters inevitably takes place due to the chemical interaction with the surface. The chemical interactions between the cluster and surface have an effect on strong trapping of the clusters at surfaces so that the thermal stability will be increased as well as the original properties of clusters elucidated in gas phase, however, should be lost at the surface. In fact, there is no report on maintenance of the native structure of the clusters after soft-landing.

I proposed the use of organic monolayer surfaces as supporting matrices to realize both the retaining of the native structure and high thermal stability of the soft-landed clusters. Among the functional clusters previously synthesized in gas phase, I adopted one-dimensional transition-metal–benzene sandwich complexes for the isolation targets. Mostly, the experimental efforts have devoted to perform the soft-landing of "metal" clusters because these clusters possess large bond energy themselves so that the composition of the clusters can be retained even after the strong chemical perturbation from the surface. This is the first time examination of soft-landing of organometallic complexes as target clusters. The experimental efforts carried out in this work are summarized as follows:

First of all, I examined the soft-landing of transition-metal–benzene sandwich complexes of the form $M(benzene)_2$ (M = Ti, V, Cr) onto self-assembled monolayers of *n*-alkanetihols (C_nH-SAM), described in Chapter 3. The C_nH-SAM species is found to serve as an excellent inert buffer matrix to discourage the decomposition of incoming complexes in the soft-landing process at hyperthermal collision energy. Furthermore, the complexes keep their native sandwich structures intact on the SAM matrices after the soft-landing and the hyperthermal incident energy process results in the penetration of the complexes into the

C_nH-SAM matrix. The complexes thus incorporated are highly oriented (with their molecular axis canted 70–80° off the surface normal), a phenomenon which is probably due to the attractive CH-π interaction between the capping benzene rings of the complex and the lateral methylene groups of the alkanethiolates. In addition, it was found that the $M(benzene)_2$ complexes penetrating into the long-chain SAMs possess unusually large adsorption heats, comparable to a typical adsorption heat of chemisorption, so that the thermal desorption of the complexes is suppressed, even at room temperature.

In Chapter 3, the thermal deposition of the $Cr(benzene)_2$ complexes are also carried out via physical vapor deposition technique in order to roughly evaluate the influence of projectile kinetic energy on resulting adsorption regime of the complexes on the C_nH-SAM substrate. Thermal deposition of the $Cr(benzene)_2$ complexes makes physisorption of the complexes on the surface of the $C_{18}H$-SAM with a random orientation and small desorprion activation energy (E_d = ~70 kJ/mol). Consequently, it was confirmed that the room-temperature isolation of the sandwich complexes could be successfully provided only after the soft-landing with hyperthermal collision energy.

Secondly, in Chapter 4, I investigate the effect of fluorination of organic monolayer matrices on the resulting soft-landing isolation regime of the sandwich complexes. The study of soft-lading onto the C_nH-SAMs suggest that the orientaional preference of the sandwich complexes may be caused by weak chemical interaction between the complex and molecules forming the SAM matrix. Thus, it can be expected that varying the chemical species within SAM matrices likely change the orientation preference of the complexes. As a result, I found the changes in orientaional preference as well as increase in thermal stability of the sandwich complexes in the fluorinated SAM with respect to that in alkanethiolate SAMs. The results conclusively suggest that both the orientaional preference and thermal

stability can be controlled well by modification of organothiolates forming the SAM matrices.

In Chapter 5, I described the endeavor of the matrix-isolation of multiple-decker V_2(benzene)$_3$ complexes and achievement of the isolation of the complexes in the C_{18}H-SAM matrix,. The infrared spectrum of the multiple-decker V_2(benzene)$_3$ complexes are obtained for the first time. Thermal desorption study reveals that the matrix-isolated V_2(benzene)$_3$ complexes resist the thermal desorption up to a high temperature of ~350 K. This is the first time achievement of soft-landing isolation of gas-phase synthesized multiple-decker V_2(benzene)$_3$ sandwich complexes with high thermal stability.

Finally, a newly designed portable cluster source mounted high-pressure, high-temperature, high-speed pulsed valves for generating supersonic beam is presented in Chapter 6. A quadrupole deflector and time-of-flight mass spectrometer (TOF-MS) are equipped at outlet of the cluster generation stage, a design which is possible to extract the generated cluster ions via measurement of their mass distribution. The portable cluster source is applied for cluster-deposition studies, and I examined installing the portable cluster source into scanning probe microscope for the measurements of physical topographic images of the clusters soft-landed on the SAM matrices

In this work, the adsorption properties and thermal chemistry of the resulting isolated complexes on the SAM matrices are elucidated by means of infrared spectroscopy, thermal desorption spectroscopy, and scanning microscopic measurements. Achievement of room-temperature isolation as well as the orientaional control of the gas-phase synthesized sandwich clusters will open up the next stage; application of these complexes for the nanostructured cluster-based materials.

References

1. Kroto, H. W.; Heath, J. R.; O'Brien, S. C.; Curl, R. F.; Smalley, R. E. *Nature* **1985**, *318*, 162.
2. Krätschmer, W; Lamb, L. D.; Fostiropoulos, K.; Huffman, D. R. *Nature* **1990**, *347*, 354.
3. Li, J; Li, X; Zhai, H. J.; Wang, L. S. *Science* **2003**, *299*, 864.
4. Hoshino, K.; Kurikawa, T.; Takeda, H.; Nakajima, A.; Kaya, K. *J. Phys. Chem.* **1995**, *99*, 3035.
5. Nakajima, A.; Kaya, K. *J. Phys. Chem. A* **2000**, *104*, 176.
6. Kurikawa, T.; Nagao, S.; Miyajima, K.; Nakajima, A.; Kaya, K. *J. Phys. Chem. A* **1998**, *102*, 1743.
7. Weis, P.; Kemper, P. R.; Bowers, M. T.; *J. Phys. Chem. A* **1997**, *101*, 8207.
8. Miyajima, K.; Nakajima. A.; Yabushita, S.; Knickelbein, M. B.; Kaya, K. *J. Am. Chem. Soc.* **2004**, *126*, 13202.
9. Wang, J.; Acioli, P. H.; Jellinek, J. *J. Am. Chem. Soc.* **2005**, *127*, 2812.
10. Heiz, U.; Schneider, W. -D. *J. Phys. D* **2000**, *33*, R85.
11. Heiz, U.; Bullock, E. L. *J. Mater. Chem.* **2004**, *14*, 564.
12. Yoon, B.; Häkkinen, H.; Landman, U.; Wörz, A. S.; Antonietti, J. -M.; Abbet, S.; Judai, K.; Heiz, U. *Science*, **2005**, *307*, 403.
13. Moseler, M.; Häkkinen, H.; Landman, U. *Phys. Rev. Lett.* **2002**, *89*, 176103.
14. Haryta, M.; Kobayashi, T.; Sano, H.; Yamada, N. *Chem. Lett.* **1987**, *34*, 405.
15. Ouyang, Z.; Takáts, Z.; Blake, T. A.; Gologan, B.; Guymon, A. J.; Wisemen, J. M.; Oliver, J. C.; Davisson, V. J.; Cooks, R. G. *Science* **2003**, *301*, 1351.
16. Gologan, B.; Takáts, Z.; Alvarez, J.; Wisemen, J. M.; Talaty, N.; Ouyang, Z.; Cooks, R. G. *J. Am. Soc. Mass Spectrom.* **2004**, *15*, 1874.

17. Pugmire, D. L.; Woodbridge, C. M.; Boag, N. M.; Langell, M. A. *Surf. Sci.* **2001**, *472*, 155.

18. Blass, P. M.; Akhter, S.; Seymour, C. M.; Lagowski, J. J.; White, J. M.; *Surf. Sci.* **1989**, *217*, 85.

19. Welipitiya, D.; Dowben, P. A.; Zhang, J.; Pai, W. W.; Wendelken, J. F. *Surf. Sci.* **1996**, *367*, 20.

20. Miller, S. A.; Luo, H.; Pachuta, S. J.; Cooks, R. G. *Science* **1997**, *275*, 1447.

21. Day, B. S.; Shuler, S. F.; Ducre, A.; Morris, J. R. *J. Chem. Phys.* **2003**, *119*, 8084.

22. Antonietti, J. –M; Gong, J.; Habibpour, V.; Röttgen, M. A.; Abbet, S.; Harding, J.; Arenz, M.; Heiz, U.; Genber, C. *Rev. Sci. Instrum.* **2007**, *78*, 054101.

23. Antonietti, J. –M; Michalski, M.; Heiz, U.; Jones, H.; Lim, K. H.; Röttgen, M. A.; Vitto, A. D.; Pacchioni, G. *Phys. Rev. Lett.* **2005**, *94*, 213402.

24. Vitto, A. D.; Pacchioni, G.; Lim, K. H.; Röttgen, M. A.; Antonietti, J. –M; Michalski, M.; Heiz, U.; Jones, H. *J. Phys. Chem. B* **2005**, *109*, 19876.

25. Fauth, K.; Schneider, N.; Heβler, M.; Schütz, G. *Eur. Phys. J. D* **2004**, *29*, 57.

26. Lau, J. T.; Föhlisch, A.; Nietubyć, R.; Reif, M.; Wurth, W. *Phys. Rev. Lett.* **2002**, *89*, 057201.

27. Lau, J. T.; Föhlisch, A.; Martins, M.; Nietubyć, R.; Reif, M.; Wurth, W. *New J. Phys.* **2002**, *4*, 98.

28. Sipr, O.; Bornemann, S.; Minar, J.; Polesya, S.; Propescu, V.; Simunek, A.; Ebert, H. *J. Phys.: Condens. Matter* **2007**, *19*, 096203.

29. Tacchi, S.; Stollo, A.; Gubbiotti, G.; Carlotti, G.; Košuth, M.; Ebert, H. *Surf. Sci.* **2007**, *601*, 4311.

30. Binns, C.; Trohidou, K. N.; Bansmann, J.; Baker, S. H.; Blackman, J. A.; Bucher, J. –P.;

Kechrakos, D.; Kleiber, A.; Louch, S.; Meiwes-Broer, K. –H.; Pastor, G. M.; Perez, A.; Xie, Y. *J. Phys. D: Appl. Phys.* **2005**, *38*, R357.

31. Kleiber, A.; Passig, J.; Meiwes-Broer, K. –H.; Getzlaff, M.; Blackman, J. A. *J. Appl. Phys.* **2007**, *101*, 114318.

CHAPTER 2

Experimental Details

2.1. Soft-Landing Technique

2.1.1. Outline of Apparatus

An overview of the experimental setup is shown in Figure 2.1. The apparatus consists of mainly three parts of high frequency laser vaporization source, the ion optics with mass selection, and energy control and the deposition/analysis chamber. The deposition/analysis chamber is equipped for performing thermal desorption spectroscopy and infrared reflection absorption spectroscopy.

In order to overcome a pressure difference of more than 10 orders of magnitudes going from expansion zone of the cluster source (~10–100 Torr) to the deposition/analysis chamber (10^{-10} Torr), the vacuum system was designed using four differentially pumped units. The source chamber is pumped by a 4900 l/s diffusion pump (ULK14A-D31, ULVAC) backed with a 77.8 l/s booster pump (PMB-003C, ULVAC) and a 10.6 l/s rotary pump (T2033A, ALCATEL). The base pressure is ~10^{-7} Torr, while vacuum level is typically in the range of 10^{-4} Torr during cluster formation with He carrier gas. The second chamber with the deflector and quadrupole mass filter is pumped by a 2000 l/s diffusion pump (MK2series 250/2000, DIFFSTAK) backed with a 25 l/s booster pump and 5.3 l/s rotary pump (YH1000C, ULVAC), and it has a base pressure of ~10^{-6} Torr. The ion-guide chamber, including two sets of octapole ion guides, is connected parallel with two 500 l/s turbo molecular pumps (PT500, Mitsubishi) backed with 4.2 l/s rotary pumps (T2015, ALCATEL). The deposition/analysis chamber consists of 1500 l/s turbo molecular pump (PT1500, Mitsubishi) tandemly-backed with 90 l/s turbo molecular pump (TMH-U071, Pfeiffer) and 8.3 l/s scroll pump (ISP-500B, ANEST IWATA), a titanium getter pump (ST707, saes), and a liquid-nitrogen-cooled cryopump. The pressure in the deposition/analysis chamber is measured using a Bayard-Alpert ionization gauge. The base pressure typically reaches

ultra-high vacuum conditions (UHV) of ~2×10^{-10} Torr in the deposition/analysis chamber, and the vacuum level is retained around 5×10^{-10} Torr even operating the He pulsed valve for cluster deposition.

The cluster source is a high frequency laser vaporization source. The metal plasma is produced by the second harmonics of a 100 Hz Nd^{3+}:YAG laser (Thunder Twice-Dual Head, Quanta System), and the vaporized metal atoms are cooled by He gas injected from a piezo-driven pulsed valve in a reaction zone. Organic vapors (typically benzene molecules) are continuously seeded via a needle valve (SS-4BMW, Swagelok) to react with the target metal atoms. The details of the cluster generation stage are described next section.

The ion optics was designed to transport the generated cluster ions from the source to the substrate mounted in the deposition/analysis chamber. The requirement of the ion optics are (a) to guide the cluster ions through the differentially pumped vacuum system with high transmission efficiency; (b) to separate the cluster ions from the neutrals by use of an ion bender (this is essential as otherwise a considerable amount of the neutral species would be deposited together with the size-selected cluster ions on the substrate); (c) mass selection bu a quadrupole mass spectrometer; (d) focusing and energy control of the cluster beam for deposition.

First, positively charged clusters are extracted by electrostatic plate through the octapole ion guides and are focused into a quadrupole deflector. The homemade quadrupole deflector is based on the design of Zeman,[1] who have showed that a two-dimensional quadrupole field can bend ion beams by 90° with low dispersion. The hyperbolic electrodes are approximated by cylindrical electrodes. Subsequent to the deflection, the cluster cations are entered into a quadrupole mass spectrometer (C60, Extrel). The diameter of quadrupole rods is 9.5 mm, it is operated by a 300 W rf-power supply at 0.88 MHz. It has an upper limit of

4000 amu. The size-selected cluster ions are further guided onto the deposition substrate by two sets of octapole ion guides. The last ion lenses focus the ion beam into a region of 6 mm diameter and decrease the velocity the cluster ions for deposition.

The target substrates are mounted on the sample holder, which is directly contacted with a liquid nitrogen (LN_2) reservoir to efficiently cool down the substrate, in the deposition/analysis chamber under UHV conditions. The substrate could be cooled down to ~120 K by contact with a liquid nitrogen reservoir, and the substrate temperature was kept at 180–220 K during the deposition by means of a heating element. The derail of the sample holder is illustrated in Figure 2.2. The ion current can be monitored by the neutralizing charge through an electrometer (6517A, Keithley) and the number of deposited clusters can be obtained by integrating the measured ion current on the substrate over the deposition time.

2.1.2. Cluster Generation and Energy Controlled Deposition

Cluster generation method via combination of the laser-vaporization techniques and molecular beam methods was presented by Smallley and Bondybey in 1981.[2–4] The surface of target material is instantaneously vaporized by the irradiation of tightly focused pulsed laser beam. The resulting hot vapor is then cooled down by a carrier gas (commonly an He gas) and aggregated to form clusters. The laser vaporization technique takes advantage because it is applicable to a wide variety of solid target, including metal, semiconductor, insulator, and high-boiling-point materials, and can produce high-density cluster packet in a short period. Since the operation of a pulsed laser and pulsed valve provide very little gas load so that a large pumping system is not required in this cluster-generation system.

A schematic view of the cluster ion source is depicted in Figure 2.3. The rotation system introduced by Gangopadhyay and Lisy is slightly modified for movement of a target metal disk.[5] The disk is integrated in a motor driven hypocycloidal planetary gear assembly.

It consists of the target disk with a diameter of 50 mm, which is connected to an inner gear (23 pitches). The inner gear turns inside an outer gear (50 pitches), and outer gear is located off-axis to the center of the source assembly. With this mechanism, the laser beam burns a hypocycloid onto the disk, which efficiently covers more than 90% of the target area. The usable surface area of disk sample is about a factor of 10 larger than in conventional sources using metal rods as target materials. Rotation of the metal disk can be operated with a stepping motor mounted in the vacuum chamber. This rotation mechanism guarantees an excellent long-term stability and the source can be operated for at least 1000 h without changing the target.

The source cavity consists of a reaction cavity and clustering channel. Unlike other cluster source, the cavity and channel are placed on coaxial with respect to the incoming laser beam. The He inlet channel is drilled into the source body, has a diameter of 2–4 mm, and the channel for injection of organic vapors is drilled at opposite side. A home-built piezo-driven pulsed valve, which has better stability as well as faster response, is used for sending He carrier gas, while continuous flow of organic vapor is introduced into the reaction room. The metal plasma is produced by the second harmonics of a 100-Hz Nd^{3+}:YAG laser. The visible green color of the second harmonics of Nd^{3+}:YAG helps the adjustment of the path of the laser beam. The power of the vaporization laser is typically 25 mJ/pulse, and the laser output is tightly focused onto a metal target with a 1000 mm optical lens. The resulting plasma is cooled by injection of He pulsed gas in the reaction cavity, and is reacted with continuously dosed organic vapors. The clustering cavity, made up by high thermal conductive material (copper), can be cooled in an efficient fashion with direct contact LN_2 reservoir in order to obtained well-cooled cluster beam.

The clusters thus generated are guided to the deposition/analysis chamber in high

transmitting efficiency mainly using octapole ion guides. A high-voltage radio-frequency (RF) generator, which is newly designed by Anderson et al.,[6,7] is used to operate the octapole ion guides. The key feature of the RF generator is that the ion guides is directly connected to the RF generator, becoming part of the capacitance of the oscillator circuit. As a result, there is no need for impedance matching or RF-coupling network so that the octapole ion guides can be operated with long-term stability.

The collision energy of the molecular beam with the target substrate was controlled by retarding field applied on the SAM substrate. Figure 2.4 shows the representative ion current of the $Cr(benzene)_2$ cation beam as function of the substrate potential. Applying retarding potential above –30 V drastically decreases the ion current and to zero above 30 V. First derivative of the ion current as function of the retarding potential (Fig. 2.4(b)) obtains an energy distribution of the mass selected $Cr(benzene)_2$ cation beam. From this curve, a broad energy distribution of about 40 eV at full-width half-maximum was estimated for the beam. In this experiment, we typically set the retarding potential to –20 V during the deposition time so that the mean kinetic energy of the positive-charged complex beam (i.e. collision energy) is close to 20 eV. However, a small amount of the complexes are inevitably deposited with lower or higher kinetic energy due to the broad energy distribution.

In the deposition/analysis chamber, thermal deposition of molecules onto a surface can be also carried out by physical vapor deposition (PVD) technique where sample vapors deposit on a solid surface with thermal energy. The target substrate is dosed by admission of sample vapor into the UHV chamber through a stainless steel doser line (1/4 inch diameter) equipped with a bellows gate valve (SS-4BW, Swagelok). Pumping of the doser line was provided with a 50 *l*/s turbo-molecular pump and the doser-line pressure was typically 1×10^{-8} Torr. The temperature of the sample and doser line was ~300 K during the substrate

exposure and the exposures was recorded in Langmuires (1L = 10^{-6} Torr·s). At room temperature, using kinetic model of ideal gas, the mean kinetic energy of gaseous molecules can be roughly estimated to be ~25 meV, a value which is only about one thousandth of deposition (collision) energy in the soft-landing experiment.

2.2. Surface Analysis

2.2.1. Infrared Reflection Absorption Spectroscopy

It is interaction of the electromagnetic field of infrared radiation with the oscillation dipole associated with a particular normal vibrational mode that allows the vibrational excitation of molecules in both of bulk and adsorbed phase. This excitation manifests itself in the absorption of a proportion of the transmitted or reflected radiation in the infrared experiment. The dipole selection rule, and factors influencing absorption intensities and frequencies of the infrared absorption in the gas, liquid, and solid state, therefore forms the basis for interpretation of IRAS spectra.

General principles of the IRAS measurement are described here.[8] Consider the reflection of infrared radiation from a clean and highly reflecting metal surface. The incident beam impinges at an angle ϕ relative to the surface normal: the incident and reflected beam and the surface normal lie in the incident plane (Figure 2.5). The interaction of the light with the surface is described by the Fresnel equations, which incorporate the appropriate boundary conditions on the electromagnetic wave equations of the incident, reflected, and reflected wav fronts, providing the amplitude r and phase δ of the reflected wave with respect to incident in terms of the complex index of refraction $\varepsilon = n + ik$, where n is refractive index and k is attenuation coefficient, of the phases making up the interface The amplitude and phase changes experienced on reflection depend upon the direction of the electric field vector

of the wave fronts, and it is convenient to resolve the electronic field vector into components in the incident plane (*P* polarized) and normal to the incident plane (*S* polarized), displayed in Figure 2.5, likewise resolving the reflection coefficients (r_s and r_p) and phase changes (δ_s and δ_p) yielded in Fresnel's equations. If $n^2 + k^2 >> 1$, which is true for metals in the infrared wavelength region, the following formula can be derived:

$$R_p = r_p^2 = \frac{(n - \sec\phi)^2 + k^2}{(n + \sec\phi)^2 + k^2} \tag{2.1}$$

$$R_s = r_s^2 = \frac{(n - \cos\phi)^2 + k^2}{(n + \cos\phi)^2 + k^2} \tag{2.2}$$

$$\Delta = \delta_p - \delta_s = \arctan\left(\frac{2k\tan\phi\sin\phi}{\tan^2\phi - (n^2 + k^2)}\right) \tag{2.3}$$

where R_p and R_s are the intensity coefficients, σ_p and σ_s the phase shifts on reflection, and ϕ is the angle of incidence (Figure 2.1).

Figure 2.6 shows a plot of R_p and R_s, σ_p and σ_s as a function of ϕ under the appropriate conditions of a highly reflecting metal in the infrared ($n = 3$, $k = 30$). The electric field at the surface is the vector sum of the electric field components due to the incident, reflected, and refracted waves. The optical properties of the metal ($n^2 + k^2 >> 1$) lead to most of the incident intensity being reflected, and the refracted wave contribution to the surface electric field is negligible. If the amplitude of the incident electric field is $E^i \sin\theta$ (where θ is an arbitrary phase), the field due to the reflected wave is $E^i r \sin(\theta + \delta)$. The resulting field at the surface is therefore given by

$$E = E^i\left[\sin\theta + r\sin(\theta + \delta)\right] \tag{2.4}$$

The *P* and *S* polarized electric field components can be considered separately as before, and we are interested in the direction of the resulting surface electric field E_p or E_s with respect to

the metal surface. Note that for all incident angles ϕ, E_s^i and E_s^r remain parallel to the surface (Figure 2.5), i.e., the resulting electric field which is parallel to the metal surface is given by Es = $E_s^i + E_s^r$, and from equation (2.4) we have

$$E_s = E_s^i\left[\sin\theta + r_s \sin\left(\theta + \delta_s\right)\right] \qquad (2.5)$$

Since δ_s is close to 180° and $r_s \approx 1$ for all ϕ (Figure 2.6) it can be seen from equation (2.5) that the 180° phase change leads to destructive interference and a vanishingly small electric field at the surface. No interaction of the surface electric field due to E_s with surface dipoles is possible.

P polarized radiation, however, behaves quite differently since the incident and reflected electric wave fields have components both parallel and normal to the surface (inset in Figure 2.7) and sum to yield parallel $E^{\parallel}{}_p$ and normal $E^{\perp}{}_p$ components of the surface electric field given by

$$E_p^{\parallel} = E_p^i \cos\phi\left[\sin\phi - r_p \sin\left(\theta + \delta_p\right)\right] \qquad (2.6)$$

$$E_p^{\perp} = E_p^i \sin\phi\left[\sin\theta - r_p \sin\left(\theta + \delta_p\right)\right] \qquad (2.7)$$

Note that for a wide range of angles ϕ, δ_p remains small (Figure 2.6) and only increases to –180° near grazing incidence. The parallel components of E_p^i and E_p^r combine to give a very small resultant field $E^{\parallel}{}_p$ at low angles, even through they are in phase, similar in magnitude ($r_p \sim 1$), and their contribution to E_p is largest [cos ϕ term in equation (2.6)] simply because they are in the opposite direction. The normal components combine constructively [equation (2.7)] but at low angles $E^{\perp}{}_p$ remains small because only a small proportion is resolved in the surface normal direction [sin ϕ term in equation (2.7)]. As ϕ increases, so does this normal component, with a concomitant decrease in the parallel component. Constructive interference yields a normal component of ~2 E_p^i before the sharp change in

phase towards –180° (Figure 2.6) causes mutual cancellation [equation (2.7)]. The effect of ϕ on the component $E^{\perp}_{p}$ is shown in Figure 2.7 again for reflection from a metal with $n = 3$, $k = 30$. One must conclude, therefore, that incident P polarized radiation can give rise to significant electric fields at metal surface, but only in direction normal to the surface, and only at grazing angles of incidence (high ϕ).

Once the enhanced electric field $E^{\perp}_{p}/ E^{i}_{p}$ has been calculated, one notes that the number of molecules with which the incoming incident ray can interact is proportional to sec ϕ, and absorption intensity is proportional to $(E^{\perp}_{p}/ E^{i}_{p})^2$. Therefore the total absorption intensity in the IRAS experiment is given by $\Delta R = (E^{\perp}_{p}/ E^{i}_{p})^2 \sec \phi$, the function plotted in Figure 2.7. This function has the same shape for all metals reflecting in the infrared, but ΔR is largest for the most highly reflecting metals. It can be seen immediately from Figure 2.7 why it is important to carry out the IRAS experiment at high angle of grazing incidence.

The essence of the theoretical modeling of the IRAS experiment on metals is contained, however, in the simplest two-phase models insofar as it shows the following:

1. Only the *p* component of the incident light can interact with the adsorbate.
2. Only molecular vibrations with a finite component of their dynamic dipole perpendicular to the surface are observable.
3. The experiment will be most efficient at high angles of incidence ϕ, i.e., at near grazing incident angles.
4. The most highly reflecting metal surface will yield the highest absorbance.

The experimental setup for the IRAS measurement performed in this study is as follows. The IRAS measurements were carried out with a FT-IR spectrometer (IFS 66v/S, Bruker): a collimated IR beam emerging through one of the side ports of the spectrometer was focused onto the sample substrate at a grazing incidence angle of ~80° from the surface normal

through a flat KBr window. After the reflection from the substrate, the IR beam exiting through another KBr window at the opposite side of the apparatus is directed onto an off-axis parabolic mirror, which refocuses the beam onto the active element of a liquid-nitrogen-cooled mercury cadmium telluride (MCT) detector. The IR optics and the detector are mounted in a vacuum chamber pumped to a pressure of about 0.1 Torr to remove spectral background contributions due to atmospheric gases, mostly carbon dioxide and water vapor. All spectra were recorded with a spectral resolution of 2 cm^{-1}. Five hundred scans were accumulated for the background and sample spectra, which were recorded before and after the cluster deposition, respectively. The data acquisition was performed with Bruker OPUS software.

2.2.2 Thermal Desorption Spectroscopy

Thermal desorption spectroscopy (TDS) is a powerful technique to determine the kinetics of desprion of molecules from surfaces.[9–11] The principle is quite simple: gaseous molecules adsorb onto a surface at low temperature, the surface is heated in a controlled fashion (often linearly with time) and a mass spectrometer is used to measure the rate at which species thermally desorbed form the surface. The thermal desorption kinetics follow the rate equation so that, in principle, each desorption rate curve in TDS spectra contains information about the rate law for desorption: the reaction order, pre-exponential factor (frequency factor), the activation energy for desorption in the desorption rate constant, and variation of each of these factor with adsorbed coverage.

For desorption kinetics which follow the Polanyi-Wigner rate expression, we have the following equation:

$$N(t) = -\frac{d\theta}{dt} = \nu_n \theta^n \exp(-E_d / RT) \tag{2.8}$$

$$T = T_0 + \beta t \tag{2.9}$$

where k_d is the desorption rate constant, θ is the coverage, n is the reaction order, ν_n is a pre-exponential factor, E_a is the adsorption heat, β is heating rate for a linear temperature ramping.

Taking the logarithm of equation (2.8), i.e. Arrhenius plot, yields:

$$\ln\left(-\frac{d\theta}{dt}\right) = \ln \nu_n + n \ln \theta - \frac{E_a}{RT}. \qquad (2.10)$$

Rearrangement (3) gives:

$$\ln\left(-\frac{d\theta}{dt}\right) - n \ln \theta = \ln \nu_n - \frac{E_a}{RT}. \qquad (2.11)$$

This expression is linear with respect to (1/T) since ν_n and E_a vary only slowly with T, and plotting the left-hand side of this expression $\left[\ln\left(-d\theta/dt\right) - n \ln \theta\right]$ versus (1/T) yields a line with slope $(-E_a/R)$ and intercept ln (ν_n). Since the desorption rate: $-d\theta/dt$ is experimentally obtained by measured TDS spectra, both E_a and ν_n can be correctly determined by the linear Arrhenius plot. However, a value of n is not provided in experiment, thus, if an incorrect value of n is used in construct the plots, the expression will retain a term containing θ and the plot will not be linear with respect to (1/T). This can be shown be easily by rewriting the left-hand side of equation (2.13) to give

$$\ln\left[\left(-\frac{d\theta}{dt}\right)\Big/\theta^n\right] = \ln \nu_n - \frac{E_a}{RT}. \qquad (2.12)$$

Substituting for $-d\theta/dt$ from equation (2.8), where the correct value for the reaction order is denoted m, and choosing an incorrect value of n leads to the following expression:

$$\ln\left[\nu_m \theta^m \exp\left(-\frac{E_a}{RT}\right)\Big/\theta^n\right] = \ln \nu_m - \frac{E_a}{RT} + (m-n)\ln \theta. \qquad (2.13)$$

Since θ is not linear with respect to T or (1/T), this expression will not be linear with respect to either T or (1/T) for all possible values of T.

Investigation of the behavior of the curves in the plots described above resulting from

incorrect choices of reaction order is best done by examining the derivative of the left-hand side of equation (2.13) with respect to (1/*T*). As an example, the case of first order desorption kinetics where *m* = 1 is examined.

For convenient, a parameter γ is now defined as follow:

$$\gamma = \ln\left(-\frac{d\theta}{dt}\right) - n\ln\theta . \tag{2.14}$$

For first order desorption spectra n = 1 and derivation of equation (2.14) gives,

$$\frac{d\gamma}{d(1/T)} = -\frac{E_a}{R}, \tag{2.15}$$

which is a constant and is simply the slope of the plot of $\left[\ln(-d\theta/dt) - n\ln\theta\right]$ versus (1/*T*) for all values of *T*. If *n* is incorrectly assumed to be zero, then

$$\frac{d\gamma}{d(1/T)} = -\frac{E_a}{R} + \frac{\nu_1 T^2}{\beta}\exp\left(-\frac{E_a}{RT}\right). \tag{2.16}$$

The explicit temperature dependence of the right-hand side of this expression means that the plot of $\left[\ln(-d\theta/dt) - n\ln\theta\right]$ versus (1/*T*) will not be linear for large values of *T*. Since the second term is small for small *T*, the slope of the function will be $(-E_a/R)$ for small *T*. Furthermore, the second term will be positive for all values meaning that the slope will increase with increment in temperature. An increase in the derivative means that the plot of $\left[\ln(-d\theta/dt) - n\ln\theta\right]$ versus (1/*T*) with n incorrectly assumed to be zero for first order desorption kinetics will curve downward.

If *n* is incorrectly assumed to be 2, then

$$\frac{d\gamma}{d(1/T)} = -\frac{E_a}{R} - \frac{\nu_1 T^2}{\beta}\exp\left(-\frac{E_a}{RT}\right). \tag{2.17}$$

Again, the temperature dependence means that the plot will not be linear for all value of *T*. The slope of the function again will be $(-E_a/R)$ for small *T*. Furthermore, the second term will be negative for all value meaning that the slope will decrease with increasing temperature. A decrease in the derivative means that the plot of $\left[\ln(-d\theta/dt) - n\ln\theta\right]$ versus (1/*T*) with *n*

incorrectly assumed to be 2 will curve upward for first order desorption kinetics.

Results of the mathematical justification presented herein are simulated in Figure 2.8 together with the simulation TDS spectra. A plot of $\left[\ln\left(-d\theta/dt\right)-n\ln\theta\right]$ versus $(1/T)$ curve downward as T increases for any value of n greater than correct value that actually describes the desertion kinetics. The plot curve upward for any chosen value of n which is smaller than the correct value, as well. It should be note that for small values of T, the curves for all choices of n result in approximately linear and have the same slope. This behavior demonstrates that the extraction of E_a form the TDS spectum can be conducted even if the correct value of reaction order in examined desorption system is unknown. Indeed, extraction of kinetic parameters in TDS spectrum using its threshold region, i.e., small T region, have been reported by a number of thermal desorption studies.[11–13]

The schematic experimental setup for the TDS measurement performed in this study is illustrated in Figure 2.9. The thermal desorption of the deposited clusters was induced by heating the substrate with a ceramic heater (MS–1, Sakaguchi E.H Voc Corp.) that was directly attached to it, as shown in Fig. 2.2. The surface temperature was monitored by a type-K thermocouple and the heating rate, controlled by a temperature controller unit (SDR–S30–P, Sakaguchi E.H Voc Corp.), was typically set at ~1 K/s. The desorbed clusters were ionized by electron impact and then detected by a quadrupole mass spectrometer (4–4000 amu; 150–QC, Extrel). The entrance of the mass spectrometer was restricted by a stainless steel skimmer (5 mmϕ, placed ~1 mm above the substrate) in order to detect only the species desorbed from the substrate surface.

2.3. Organic Monolayer Matrix

The surface on which a organic monolayer forms and the physical object supporting that

surface often are referred to as the "substrate". Types of substrates range from planner surfaces (glass or silicon slabs supporting thin film films of metal, metal foils, single crystals) to highly covered nanostructure (colloids, nanocrystals, nanorods). Planner substrates are used widely for characterizing the relationship between the structure and property of the monolayers because they are easy to prepare and compatible with a number of techniques for surface analysis and spectroscopic characterization.

The critical important for selecting the type of substrate are dependent on the application for which the SAM is used. Polycrystalline films are sufficient for many appreciations on planner substrates such as model surface for studying structure, growth, and phase behavior of the monolayers because a wide range of materials can be deposited easily. In this study, I used two types of commercially available two kinds of gold substrates: a polycrystalline gold film (Auro Sheet, Tanaka Precious Metals Co. Ltd.), consisting of Au(100 nm thickness)/Ti/Silica having more than 80% Au(111) facet on the surface, and a single crystal substrate (99.999%, MaTeck) faceted to provide atomically flat Au(111) surface, respectively.

2.3.1. Sample Preparation

For the polycrystalline gold film, a number of grains (~50 nm) are observed on the surface by noncontact atomic force microscopy (JSPM-5200, JEOL) as shown in Figures 2.10 (a) and (b). In order to obtain the flatness of the gold substrate, i.e. to produce atomically flat terraces, thermal annealing (200 °C, 2hour) of the gold film is carried out.[14] A results in shown in Figs 2.10 (c) and (d). As evident from the images, the morphology of the substrates changes dramatically upon annealing to provide long-range smooth terraces.

In this study, self-assembled monolayers of various chain-length *n*-alkanethiols ($C_nH_{2n+1}SH$; n = 4, 8, 12, 16, 18, and 22) and heptadecafluoro-undecanethiol ($C_{10}F_{15}H_4SH$)

were prepared for the organic monolayer surface. The molecular structures of typical single *n*-alkanethiol and heptadecafluoro-undecanethiol are represented in Figure 2.11. As well known, the backbone of *n*-alkanethiol, i.e. alkyl chain, forms planner *all-trans* zigzag conformation (Fig. 2.11 (a)) that is flexible because of low rotational barriers to transform *gauche* conformation. In contrast, the fluorocarbon chain forms helical conformation (Fig. 2.11 (b)) due to intramolecular stability, which will provide conformational rigidity of the backbone in the fluorocarbon chains.

In order to remove organic contaminants from the gold surface, the substrate was chemically cleaned by dipping in a piranha solution (3:1 concentrated H_2SO_4:H_2O_2) for about 20 minutes. Each SAM substrate was prepared by immersing the gold substrates into a 0.5 mM ethanolic solution of alkanethiols at ambient temperature for 20 hours. Hertfort, the author will denote the self-assembled monolayers of *n*-alkanethiol as C_nH-SAM, and heptadecafluoro-undecanethiol as C_{10}F-SAM, respectively

2.3.2. Characterization of Organic Surface

A variety of experimental methods have been used to probe the quality of the SAMs,[15,16] from the techniques that are macroscopic and average the signal across the entire film, to local probes. In this study, I employed contact angle goniometry (Drop Master 300, Kyowa Interface Science) and IRAS to confirm the formation of the SAMs on the gold substrate.

The contact angles of a water droplet (1 μl) on the C_n-SAMs and C_{10}F-SAM at room temperature are listed in Table 1, along with the bare gold surface. While the bare gold surface was completely wetted (~ 0°), the hydrophobic nature of all the C_nH-SAMs and C_{10}F-SAM examined was revealed by their large contact angles of 100–110°. The contact angles obtained are in good agreement with literature values for the corresponding SAMs anchored on gold surfaces.[17,18]

The IRAS spectra for the above C_nH-SAMs on the gold surface in the C-H stretching region are shown in Figure 2.12. These data are in good accordance with previously reported IRAS spectra.[19,20] Thus, the bands denoted as r^+ and r^- can be assigned to the antisymmetric and symmetric stretching modes of the terminal methyl group, respectively. The r^+ peak is split into a doublet, because of Fermi resonance interactions with the overtone of the lower frequency methylene scissoring mode.[21,22] The d^+ and d^- peaks, whose intensities increase with the alkyl-chain length, are respectively assigned to the antisymmetric and symmetric methylene stretching modes. The observed vibrational frequencies of the methylene modes (d^+ and d^-) in the long-chain $C_{16}H$- to $C_{22}H$-SAMs agree with those of crystalline-state alkanethiolate-SAMs, indicating the formation of densely packed, crystal-like alkanethiolate monolayers on the gold surfaces. In the short-chain C_8H- and $C_{12}H$-SAM spectra, the d^- peak is slightly shifted toward higher frequency (2920 cm^{-1}), a change which is probably due to a partial disordering of the short-chain C_8H- and $C_{12}H$-SAMs at room temperature.[23] The observed frequencies and corresponding vibrational modes for the $C_{18}H$-SAM are listed in Table 2.2. The IRAS spectrum for the $C_{10}F$-SAM on the gold surface in the 600–1550 cm^{-1} region measured at surface temperature of 160 K is shown in Figure 2.13. These data are in good accordance with previously reported IRAS spectra.[24,25] The observed frequencies and corresponding vibrational modes for the $C_{10}F$-SAM are listed in Table 2.3 together with the directions of the transition dipole moment of each vibrational mode toward the fluorocarbon helical axis.

The superlattice structures and schematic illustrations of the C_nH-SAM and $C_{10}F$-SAM on Au(111) surface are shown in Figure 2.14. As shown in Fig 2.14 (a), the C_nH-SAM forms densely packed hexagonal $\left(\sqrt{3}\times\sqrt{3}\right)R30^\circ$ structure, i.e. $c(4 \times 2)$ superlattice, corresponding to a molecule–molecule spacing of ~5 Å, where the van der Waals diameter of

the hydrocarbon chain is 4.2 Å. On the other hand, the $C_{10}F$-SAM also constructs highly packed *c*(7 × 7) superlattice on the Au(111) surface (Fig. 2.14 (b)) with an average nearest–neighbor spacing of ~5.8 Å, close to the van der Waals diameter of the fluorocarbon chain. The orientation angles of hydrocarbon and fluorocarbon axis are estimated to be ~30° and ~16°, respectively.

References

1. Zeman, H. D. *Rev. Sci. Instrum.* **1977**, *48*, 1079.
2. Dietz, T. G.; Duncan, M. A.; Powers, D. E.; Smalley, R. E. *J. Chem. Phys.* **1981**, *74*, 6511.
3. Bondybey, V. E.; English, J. H. *J. Chem. Phys.* **1982**, *86*, 2156.
4. Smalley, R. E. *Laser Chem.* **1983**, *2*, 167.
5. Gangopadhyay, P.; Lisy, J. *Rev. Sci. Instrum.* **1991**, *62*, 502.
6. Jones, R. M.; Gerlich, D.; Anderson, S. L. *Rev. Sci. Instrum.* **1997**, *68*, 3357.
7. Jones, R. M.; Anderson, S. L. *Rev. Sci. Instrum.* **2000**, *71*, 4335.
8. Hayden, B. E. In *Vibrational Spectroscopy of Molecules on Surface*; Yates, J. T., Jr.; Modey, T. E., Eds.; Method of Surface Characterization · vol. 1; Plenum Press; New York, NY, 1987; Chapter 7.
9. King, D. A. *Surf. Sci.* **1975**, *47*, 384.
10. Parker, D. H.; Jones, M. E.; Koel, B. E. *Surf. Sci.* **1990**, *233*, 65.
11. Miller, J. B.; Siddiqui, H. R.; Gates, S. M.; Russell, J. N., Jr.; Yates, J. T., Jr.; Tully, J. C.; Cardillo, M. J. *J. Chem. Phys.* **1987**, *87*, 6725.
12. Vogt, A. D.; Beebe, T. P., Jr. *Langmuir* **1999**, *15*, 2755.
13. Vogt, A. D.; Beebe, T. P., Jr. *J. Phys. Chem. B* **1999**, *103*, 8482.
14. Nogues, C.; Wanunu, M. *Surf. Sci.* **2004**, *573*, L383.
15. Schreiber, F. *Prog. Surf. Sci.* **2000**, *65*, 151.
16. Love, J. C.; Estroff, L. A.; Kriebel, J. K.; Nuzzo, R. G.; Whitesides, G. M. *Chem. Rev.* **2005**, *105*, 1103.
17. Dubois, L. H.; Zegarski, B. R.; Nuzzo, R. G. *J. Am. Chem. Soc.* **1990**, *112*, 570.
18. Linford, M. R.; Fenter, P.; Eisenberger, P. M.; Chidsey, C. E. D. *J. Am. Chem. Soc.* **1995**, *117*, 3145.

19. Porter, M. D.; Bright, T. B.; Allara, D. L.; Chidsey, C. E. D. *J. Am. Chem. Soc.* **1987**, *109*, 3559.

20. Rodriguez, K. R.; Shah, S.; Williams, S. M.; Teeters-Kennedy, S.; Coe, J. V. *J. Chem. Phys.* **2004**, *121*, 8671.

21. Hill, I. R.; Levin, I. W. *J. Phys. Chem.* **1979**, *70*, 842.

22. McPhail, R. A.; Snyder, R. G.; Strauss, H. L.; Ellinger, C. A. *J. Phys. Chem.* **1984**, *88*, 334.

23. Porter, M. D.; Bright, T. B.; Allara, D. L.; Chidsey, C. E. D. *J. Am. Chem. Soc.* **1987**, *109*, 3559–3568.

24. Lenk, T. J.; Hallmark, V. M.; Hoffmann, C. L.; Rabolt, J. F.; Castner, D. G.; Erdelen, C.; Rengsdorf, H. *Langmuir* **1994**, *10*, 4610.

25. Tsao, M. –W.; Hoffmann, C. L.; Rabolt, J. F.; Johnson, H. E.; Castner, D. G.; Erdelen, C.; Rengsdorf, H. *Langmuir* **1997**, *13*, 4317.

Table 2.1: Contact angle of water drops (1 μl) on the C_nH-SAMs and $C_{10}H$-SAM and the gold substrate.

Substrates	Contact angle (deg.)
C_8H -SAM	104 ± 1
$C_{12}H$ -SAM	107 ± 1
$C_{16}H$ -SAM	105 ± 1
$C_{18}H$ -SAM	106 ± 2
$C_{22}H$-SAM	107 ± 1
$C_{10}F$-SAM	112 ± 1
bare gold	~0

Table 2.2: Spectral mode assignments for *n*-octadecanethiol self-assembled on a gold surface

frequency observed	mode assignment
2847	CH_2, C–H symmetric stretching (d^+)
2878	CH_3, C–H symmetric stretching, Fermi resonance (r^+)
2917	CH_2, C–H asymmetric stretching (d^-)
2938	CH_3, C–H symmetric stretching, Fermi resonance (r^+)
2957	CH_3, C–H asymmetric stretching, out-of-plane (r^-)
2963	CH_3, C–H asymmetric stretching, in-plane (r^-)

Table 2.3: Spectral mode assignments for heptadecafluoro-undecanethiol ($C_{10}F_{15}H_4SH$) self-assembled on a gold surface [a]

frequency observed	mode assignment	dipole moment [b]
667	$w(CF_2)$, $r(CF_2)$	parallel
693	$w(CF_2)$, $r(CF_2)$	parallel
709	$v(CF_3)$ end group	parallel
962	δ(CCC), $r(CH_2)$	parallel
1003	$r(CH_2)$	parallel, perpendicular
1036	v(CC), trans planar	perpendicular
1076	v(CC), gauche	parallel
1119	v(CC), trans planar	perpendicular
1156	$v_a(CF_2)$, $\delta(CF_2)$	perpendicular
1207	$v_a(CF_2)$, v_a (CF_3)	perpendicular
1220	δ(CCC), v(CC)	perpendicular
1245	$v_a(CF_2)$, r (CF_2)	perpendicular
1284	$w(CH_2)$, $r(CF_2)$	parallel
1335	$v(CF_2)$ progression: axial CF_2 stretching	parallel
1372	$v(CF_2)$ progression: axial CF_2 stretching	parallel

[a] vibraional modes: v-stretching; δ-bending; r-rocking; w-wagging. [b] Directions of transition dipole moments with respect to the fluorocarbon helical axis.

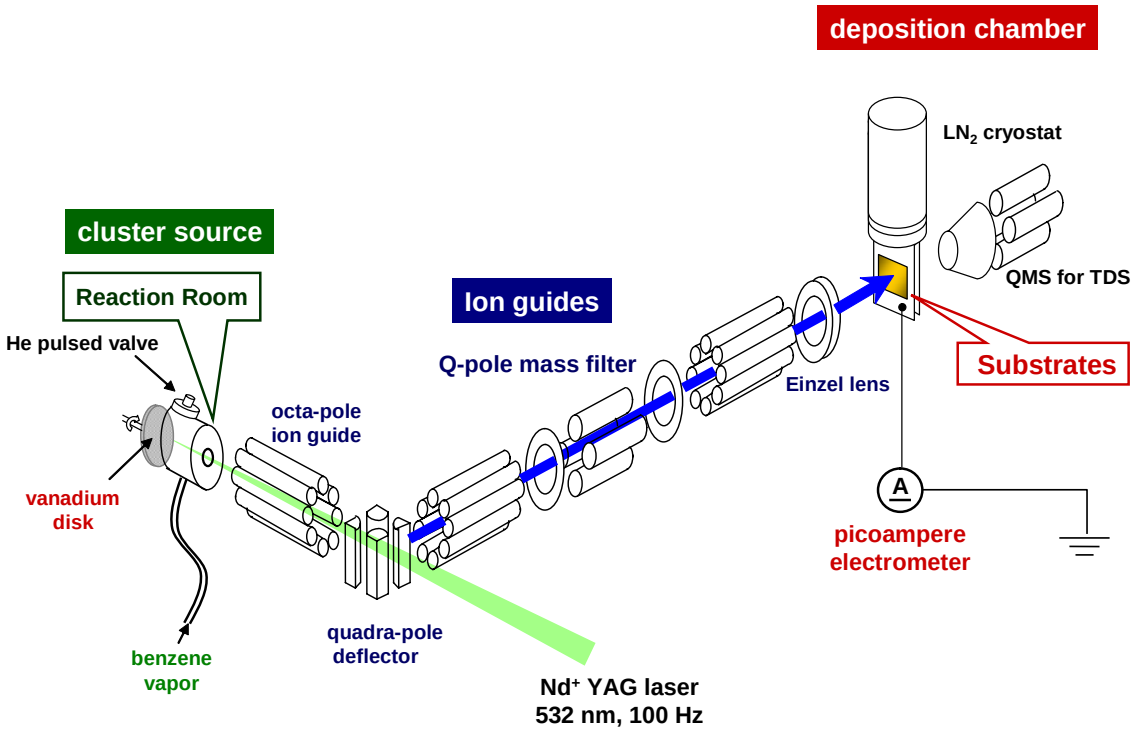

Figure 2.1. Overview of the experimental setup for soft-landing technique with the laser vaporization cluster source, ion guides, and deposition/analysis chamber.

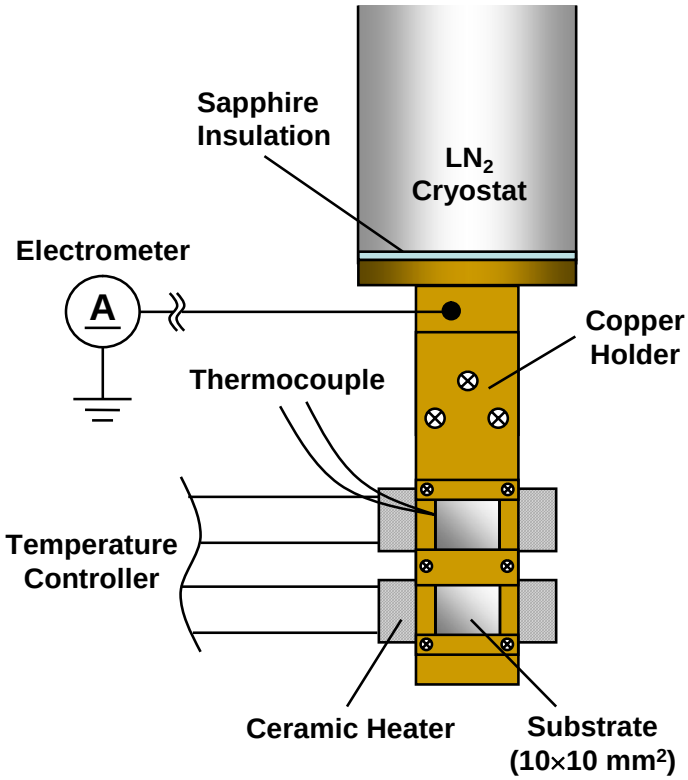

Figure 2.2. Details of the sample holder in the deposition chamber. To cool down the substrates efficiently using a LN_2 reservoir, a high thermal conductivity material (copper) was used for the sample holder. The ceramic heaters mounted inside the holder were placed in mechanical contact with the substrates to rapidly and even heating. The surface temperature was measured by a type-K chromel-alumel thermocouple and controlled by a proportional integral differential (PID) operation programmed by a temperature controller unit.

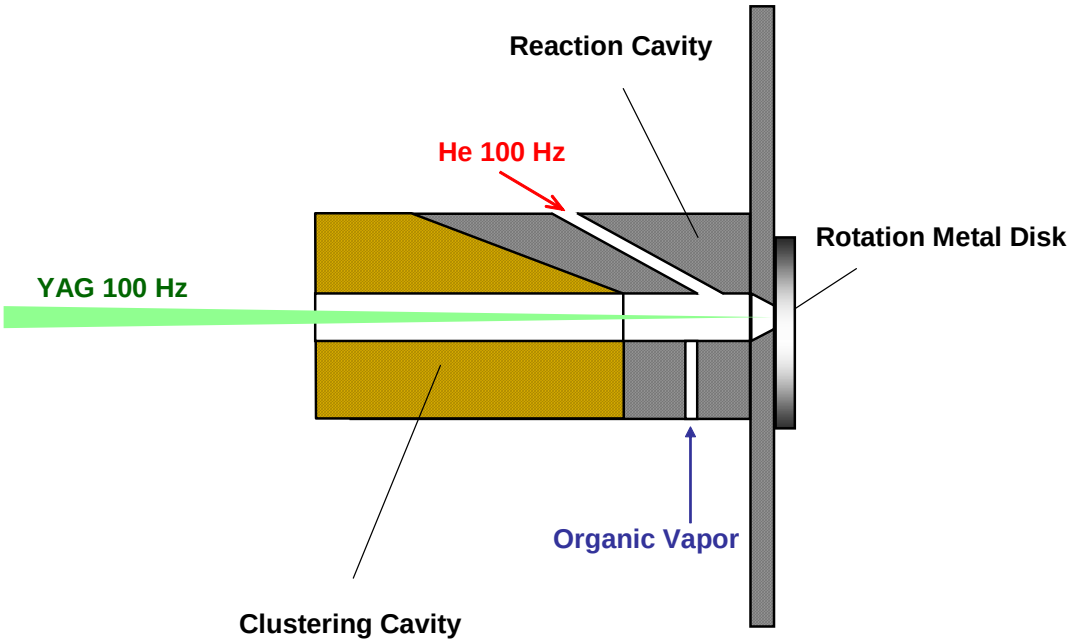

Figure 2.3. Schematic diagram of the high frequency laser vaporization source for the generation of organometallic complexes. In contrast to the conventional sources the laser beam is coaxial to the molecular beam axis. In order to provide a capable cooling of the clustering cavity using a LN_2 reservoir, a high thermal conductivity material (copper) was used while the other components are based on stainless-steel alloy.

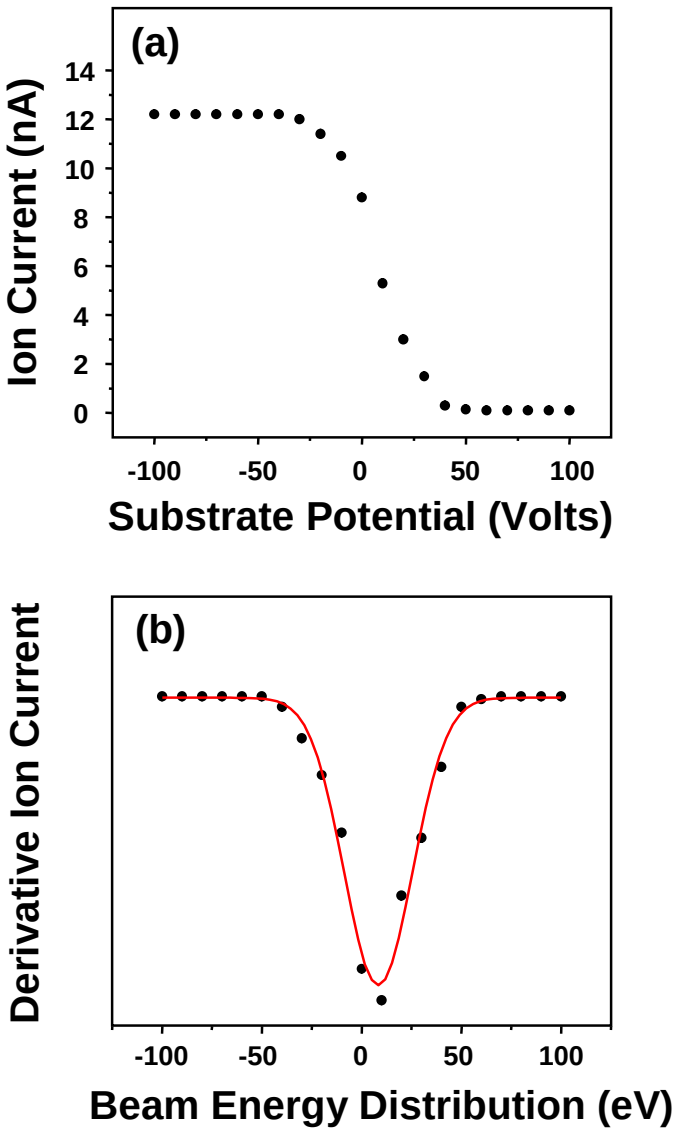

Figure 2.4. Typical ion current for molecular beam of size-selected $Cr^{+}(benzene)_2$ complexes (a) obtained at the substrate by varying applied potential, and (b) first derivative of the ion current as function of the substrate potential, measuring the energy distribution of the molecular beam. The full width at half maximum is about 40 eV.

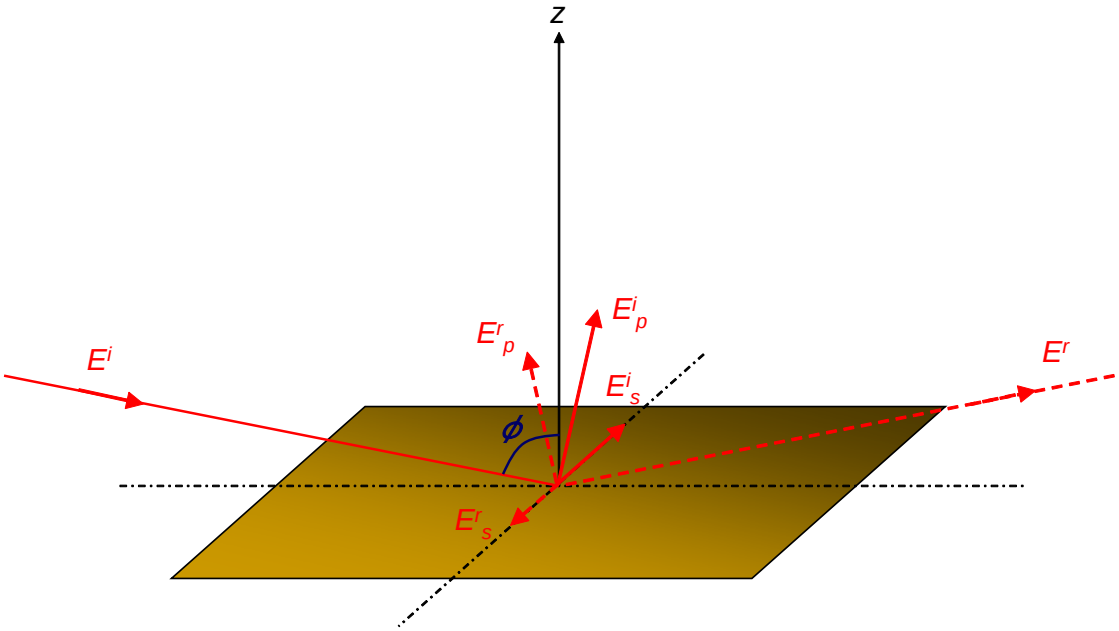

Figure 2.5. The reflection geometry showing the *s* and *p* components of the electric fileds of incident (E^i) and reflected (E^r) radiation.

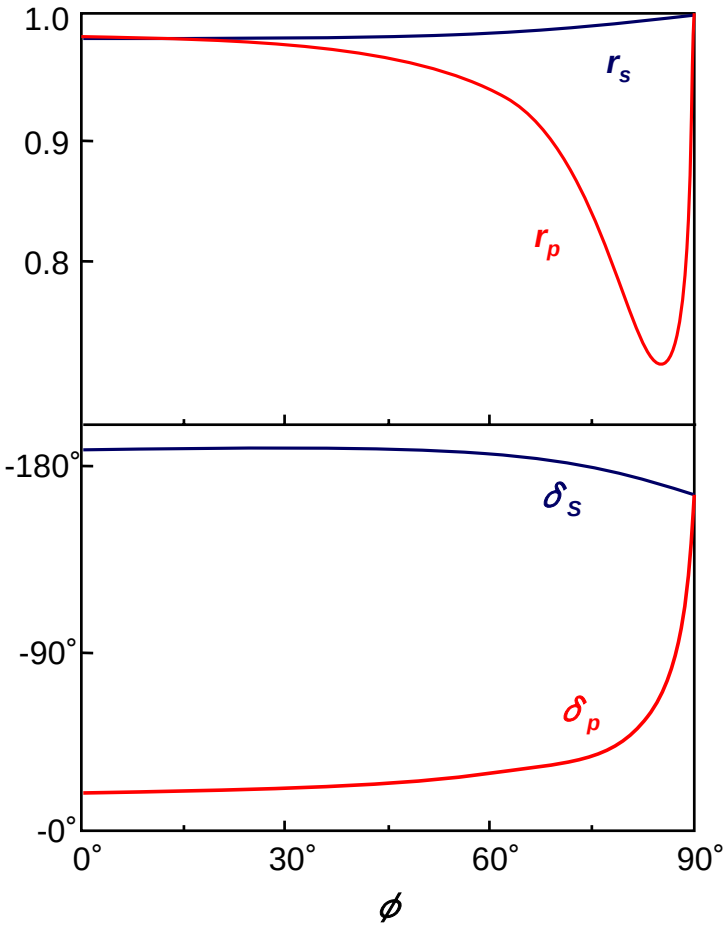

Figure 2.6. The intensity coefficients (R) and phase shift (σ) of the s and p components of the infrared radiation on reflection from a metal ($n = 3$, $k = 30$) surface.

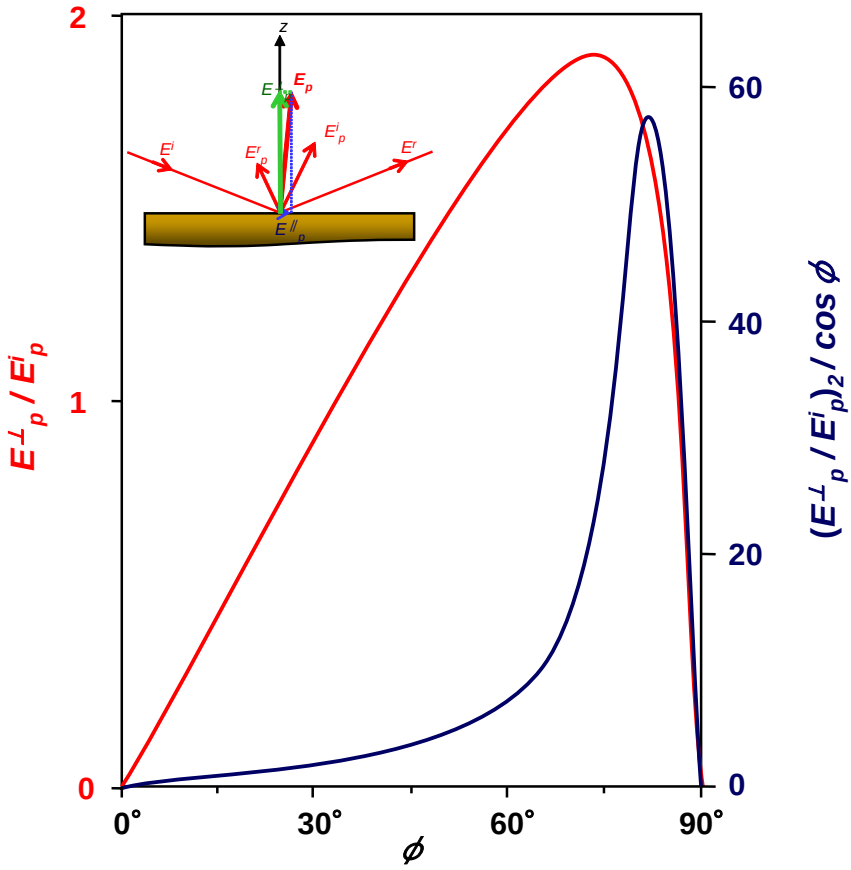

Figure 2.7. The relative amplitude ($E^{\perp}_p / E^i_p$) of the electric field perpendicular to the surface as a function of incident angle ϕ, together with the quantity ($E^{\perp}_p / E^i_p$)secϕ. The inset shows the dominance of the normal component of the field of the surface arising from the *p* component.

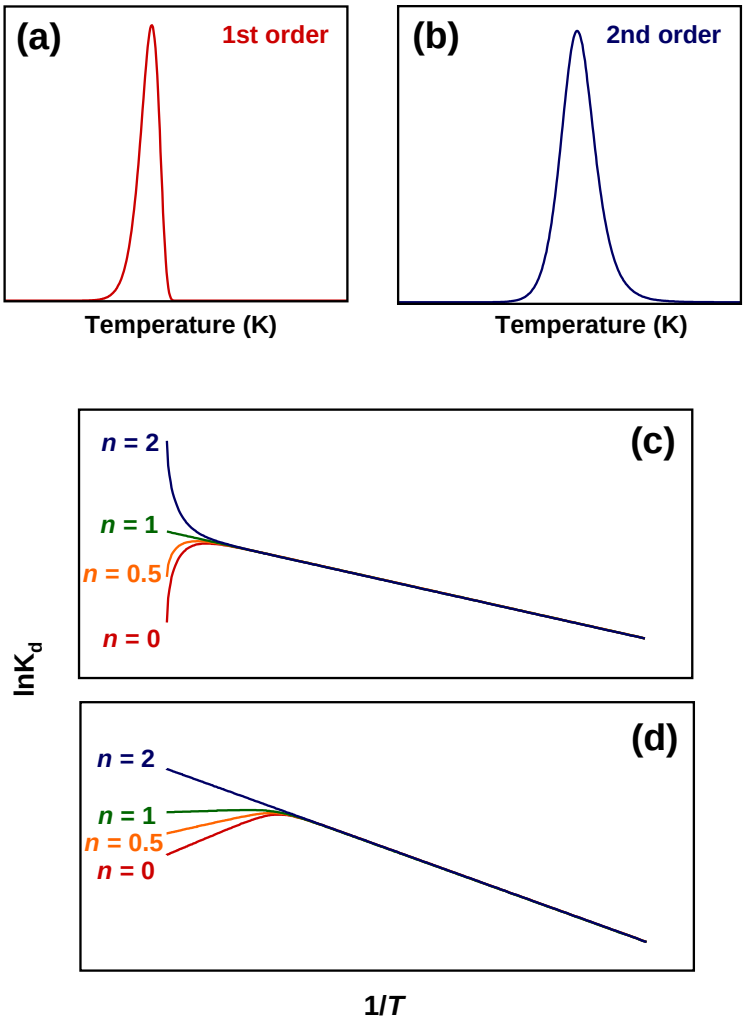

Figure 2.8. Computed simulations of TDS spectra calculated for E_a = 100 kJ/mol with β = 1 K/s for first (a) and second (b) order kinetics. Arrhenius plots for (a) and (b) are shown in panel (c) and (d), respectively, using n = 0, 0.5, 1, 2 in arbitrary of rate and coverage.

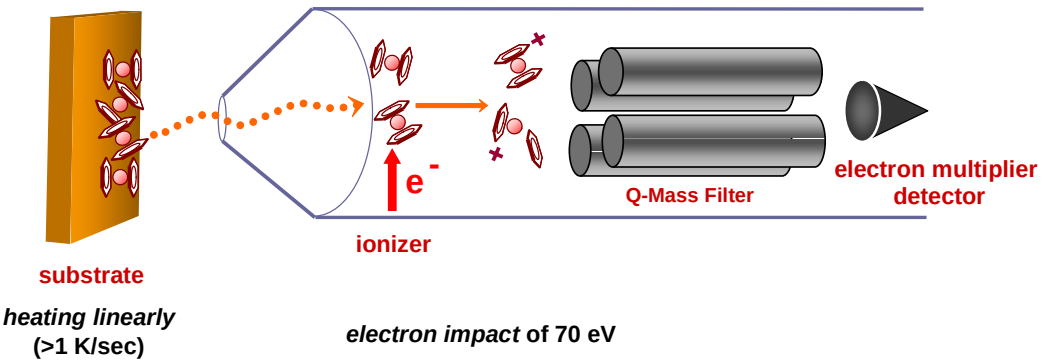

Figure 2.9. Schematic experimental setup for thermal desorption spectroscopy.

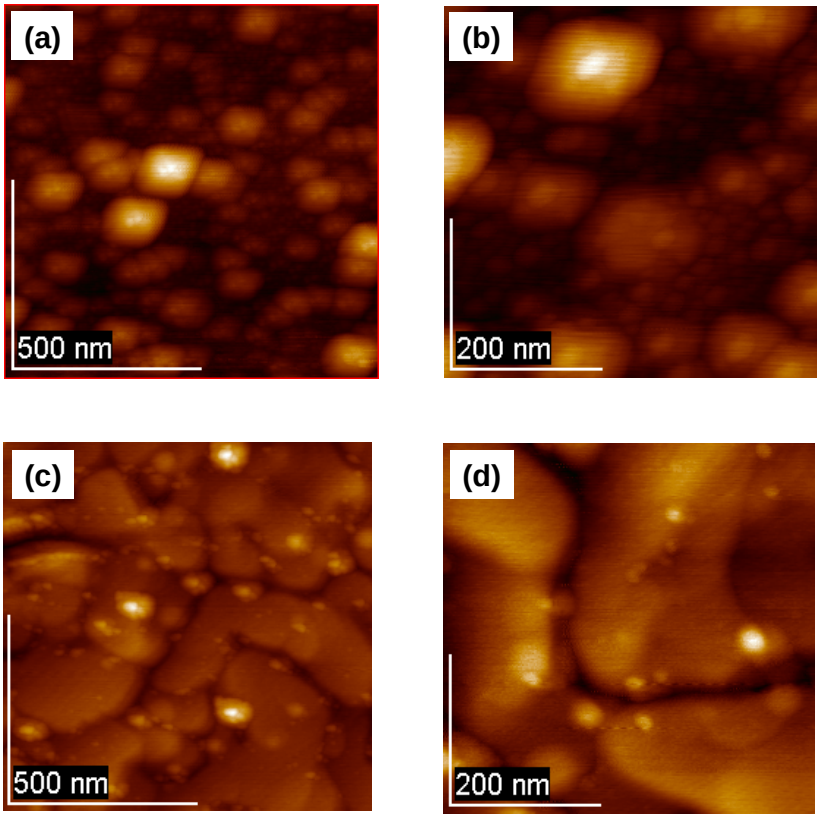

Figure 2.10. Topographic images for (a), (b) unannealed and (c), (d) annealed surface of a polycrystalline gold film (Auro Sheet) measured by noncontact atomic force microscopy.

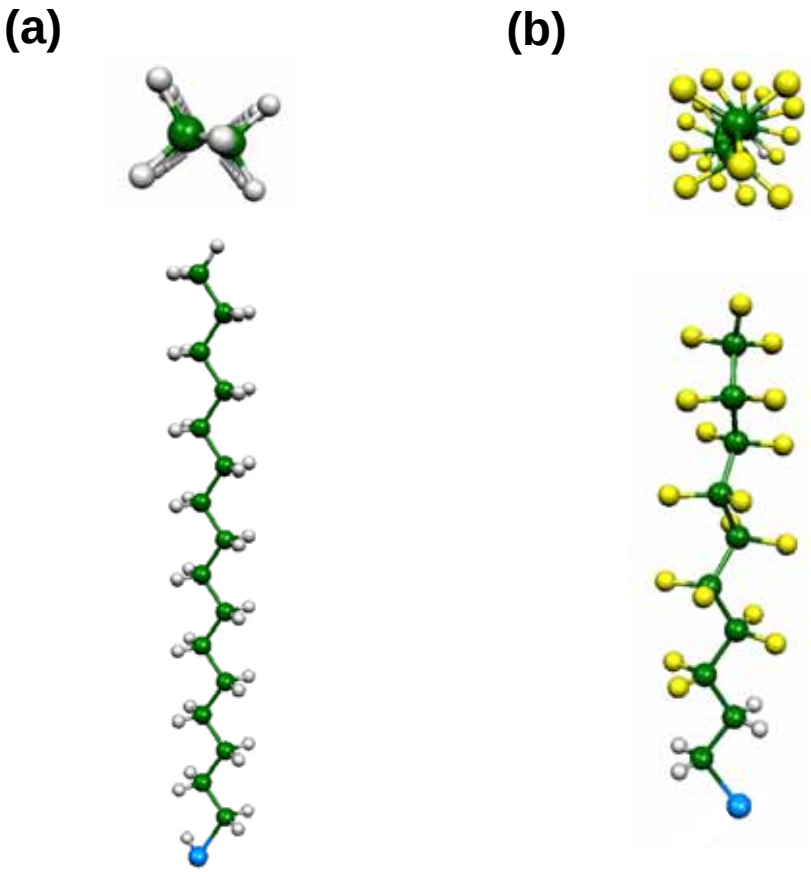

Figure 2.11. Schematic diagrams of (a) *n*-hexadecanethiolate ($C_{16}H_{33}S$-) and (b) heptadecafluoro-undecanethiolate ($C_{10}F_{15}H_4S$-). Planner zigzag conformation of hydrocarbon chain is provided in the alkyl chain, in contrast, the fluorocarbon chain forms helical conformation.

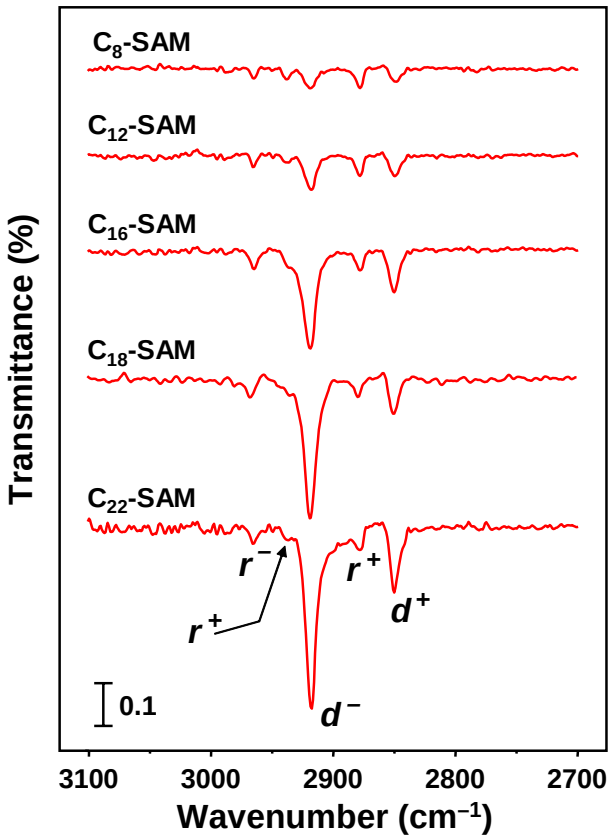

Figure 2.12. IRAS spectra in the C-H stretching region (2700–3100 cm^{-1}) for *n*-alkanethiols adsorbed on the gold substrate measured at room temperature.

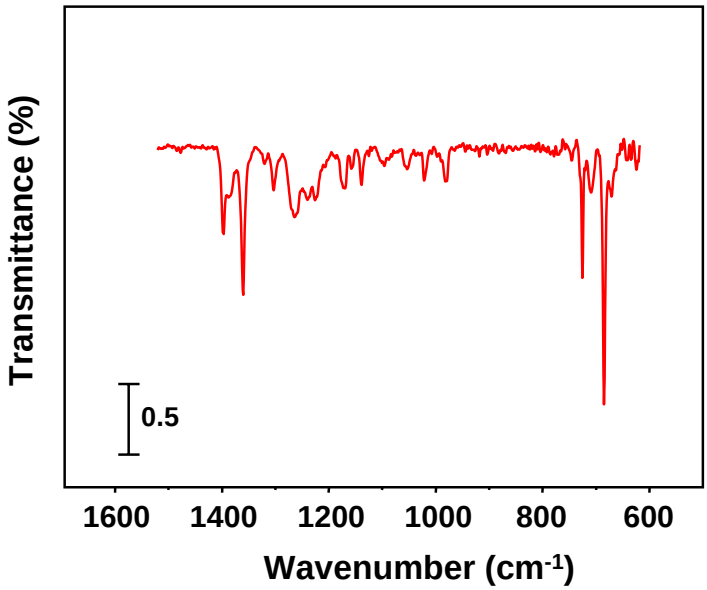

Figure 2.13. IRAS spectra in the 600–1550 cm^{-1} region for heptadecafluoro-undecanethiol ($C_{10}F_{16}H_4SH$) adsorbed on the gold substrate measured at 160 K.

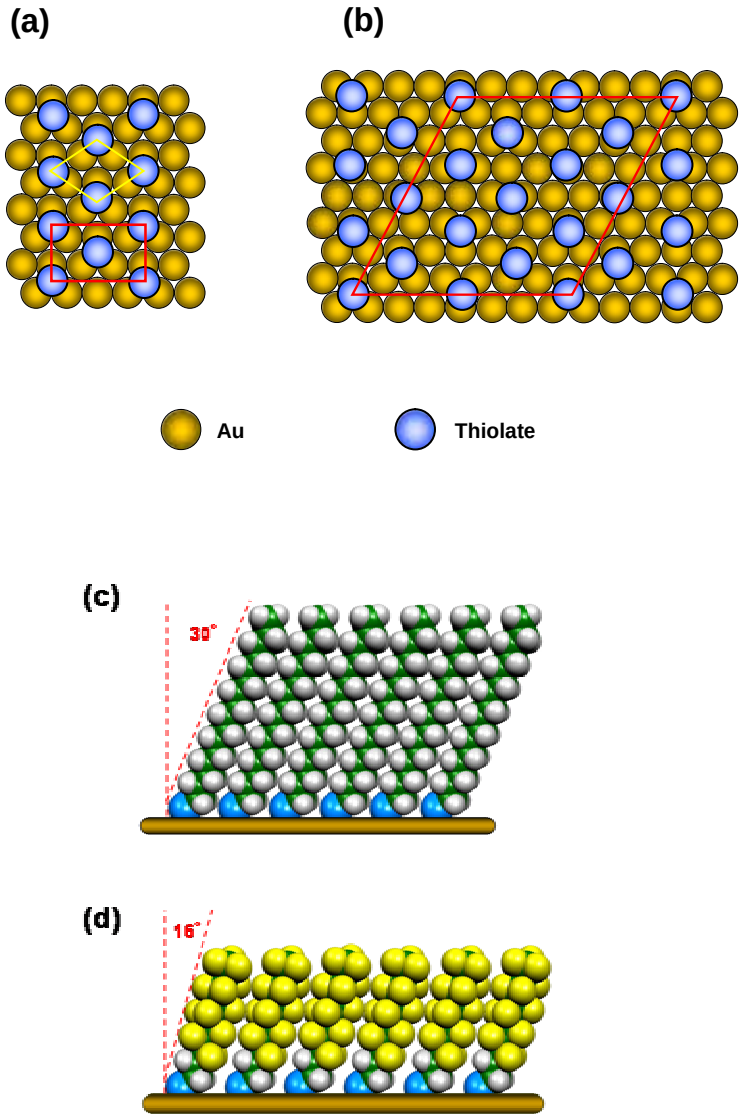

Figure 2.14. Schematic drawing of superlattice structure for (a) $C_{16}H$-SAM and (b) $C_{10}F$-SAM on Au(111) surface. The arrangement corresponds to the commensurate $c(4\times 2)$ in red parallelogram ($(\sqrt{3}\times \sqrt{3})R30^{o}$ in yellow parallelogram) for $C_{16}H$-SAM and $c(7\times 7)$ in red parallelogram for $C_{10}F$-SAM, respectively. Schematic illustrations of (c) $C_{16}H$-SAM and (d) $C_{10}F$-SAM represent the tilted angle of ~30º and ~16º, respectively.

CHAPTER 3

Soft-Landing Isolation of Transition-Metal–Benzene Complexes: M(benzene)$_2$ in *n*-Alkanethiol Self-Assembled Monolayer Matrices

Abstract

The adsorption state and thermal stability of V(benzene)$_2$ sandwich complexes soft-landed onto a self-assembled monolayer of different chain-length *n*-alkanethiols (C_nH-SAM, n = 8, 12, 16, 18, and 22) at hyperthermal collision energy (~20 eV) were studied by means of infrared reflection absorption spectroscopy (IRAS) and thermal desorption spectroscopy (TDS). The IRAS measurement confirmed that V(benzene)$_2$ complexes are molecularly adsorbed and maintain a sandwich structure on all of the SAM substrates. In addition, the complexes supported on the SAM substrates are oriented with their molecular axes tilted 70–80° off the surface normal. An Arrhenius analysis of the TDS spectra reveals that the activation energy for the desorption of the supported complexes increases linearly with the chain-length of the SAMs. For the longest chain C_{22}H-SAM, the activation energy reaches ~150 kJ/mol, and the thermal desorption of the supported complexes can be considerably suppressed near room temperature. The other transition-metal–benzene complexes of Ti(benzene)$_2$ and Cr(benzene)$_2$ show the similar adsorption state and thermal stability on the SAM substrate. For comparison, thermal deposition (~25 meV) of Cr(benzene)$_2$ vapor onto the C_{18}H-SAM is also carried out using physical vapor deposition technique, showing that the complexes are weakly physisorbed (E_d = ~70 kJ/mol) on the SAM with a random orientation. Only with hyperthermal collision event, the incident complexes can penetrate into the SAM matrix, and then the desorption of the embedded complexes in the SAM can be effectually suppressed up to around room temperature, which may be associated with the crystal-rotator phase transitions of the SAM matrix.

3.1. Introduction

Over the past decade, gas-phase synthesis by means of the laser-vaporization of metals has provided various kinds of metal clusters as well as organometallic complexes. These gaseous clusters have generated a great deal of attention due to their strongly size-dependent properties that are often different from those of the bulk materials. In particular, since the discovery of the multi-decked vanadium (V)–benzene sandwich complex $V_n(benzene)_{n+1}$,[1] a wide variety of experimental and theoretical efforts have been devoted to its characterization.[2–14] For example, it has been recently discovered that $V_n(benzene)_{n+1}$ complexes possess unique, size-dependent electronic[10–12] and ferromagnetic[13,14] properties originating from their 1D structures. Hence, they are expected to become one of the most promising candidates for use as building blocks in nanodevices.

Non-dissociative deposition of mass-selected cluster ions produced in the gas phase onto a pertinent substrate, a so-called "soft-landing", provides a possible use for the intriguing clusters as building blocks in cluster-based nanomaterials. Recently, surface modification via soft-landing of gas-phase ionic compounds such as metal clusters and biomolecules onto a solid surface increasingly enables the creation of new types of nanoscale materials, e.g. nanocatalysts,[15–17] nanomagnetics,[18–20] and biological microarrays.[21–23] However, there are rather few studies of soft-landing or vapor deposition of the organometallic sandwich complexes onto solid surfaces. In our laboratory, $V(benzene)_2$ sandwich complexes have been soft-landed onto a gold substrate covered with a low-temperature Ar matrix, and infrared spectroscopy has confirmed that they adopt a sandwich structure.[24] While direct deposition of the gaseous clusters onto a bare metal surface often results in dissociation of the clusters upon impact, the rare gas matrix can serve as a buffer layer, dissipating the kinetic energy of the projectile clusters and keeping the cluster largely intact.[25,26] However, the use of the rare

gas matrix is limited to extremely low substrate-temperature conditions, because the rare gas Ar matrix evaporates at a temperature of ~18 K.

Subsequent to soft-landing, the clusters inevitably undergo an interaction with a substrate surface. A profound insight into the cluster–surface interaction is critical for the fabrication of cluster-based nanomaterials. A study of the catalyzed oxidation of CO on Au_8 clusters soft-landed on a magnesia surface, for instance, demonstrated that a charging of the metal cluster, caused by the partial transfer of charge from an F-center of the surface into the deposited cluster, underlies the catalytic activity of the Au_8 clusters.[17] The F-centers further serve to strongly anchor the deposited clusters, thereby inhibiting their diffusion and coalescence on the surface until temperatures of ~350 K.

On a related note, the adsorption properties of 1D organometallic sandwich complexes on metal surfaces have been studied by physical vapor deposition onto the surface under ultra-high vacuum (UHV) conditions.[27–29] In strong contrast to the supported metal clusters, organometallic complexes are considered to be rather unstable with respect to bare metal surfaces. Indeed, Blass *et al.* demonstrated that a $Cr(benzene)_2$ sandwich complex chemisorbed on a Ni(100) surface dissociates its ligand–metal bond due to a strong perturbation from the Ni(100) surface.[28] Thus, to support organometallic complexes on a substrate, the use of chemically inert substrate is required to reduce such metal surface perturbations. However, a study of the adsorption of ferrocene, $Fe(C_5H_5)_2$, on a relatively inert Ag(100) surface showed that ferrocene adsorbs molecularly on an Ag(100) surface, but the weak adsorbate–surface interaction permits the thermal desorption of the adsorbed ferrocene at temperatures as low as 200 K. This desorption occurs because of the small desorption activation energy (or adsorption heat).[29] Therefore, an ingenious cluster-supporting methodology, realizing both a small structural perturbation (i.e.

maintenance of the sandwich structure) and a high adsorption heat (i.e. a high desorption temperature) of the supported organometallic sandwich complexes, is a highly desired goal.

Recently, Cooks and co-workers have described a technique to support gas-phase ionic species on a solid surface.[30–32] They have achieved trapping of gas-phase polyatomic ions using a self-assembled monolayer (SAM) of fluorocarbon as the supporting matrix.[30] They have also shown that the soft-landed bulky polyatomic ions can penetrate into the SAM and they are sterically trapped inside the SAM, while retaining their charge. Another important ability of the SAM has been demonstrated, in that it can serve as a effective buffer layer like a rare gas matrix, dissipating the kinetic energy of the projectiles.[33–35] For example, Day *et al.* have performed a detailed study of a rare gas collision with *n*-alkanethiolate SAMs and found that the long-chain alkanethiolate SAM effectively dissipates the translational energy of the projectile atom.[33] They estimated that more than 80% of the incident energy of the projectiles transferred to internal energy of the organic surface. Based upon the above-mentioned results, SAMs are likely to be promising matrixes to suppress the dissociation of the clusters in the soft-landing process and to realize the effective trapping of intact clusters.

Toward this ambitious end, I employed long-chain alkanethiolate-SAMs as cluster-trapping matrixes and succeeded in the room-temperature matrix isolation of the gas-phase synthesized vanadium-benzene 1:2 sandwich complexes, $V(benzene)_2$, in the *neutral* state. The SAM matrix-isolation scheme of the gas-phase synthesized complexes via soft-landing is shown in Fig. 3.1. In the chapter, firstly, I present the experimental results obtained for the alkanethiolate-SAM matrix isolation of the $V(benzene)_2$ sandwich complexes via a soft-landing technique. The $V(benzene)_2$ complexes produced in the gas phase were size-selectively soft-landed onto a bare gold substrate and on various chain-length

n-alkanethiolate self-assembled monolayers (C_nH-SAM with n = 8, 12, 16, 18, and 22). The adsorption state and thermal chemistry of the soft-landed complexes were examined by means of infrared reflection absorption spectroscopy (IRAS) and thermal desorption spectroscopy (TDS). A highly oriented adsorption geometry as well as an unusually large adsorption heat of the adsorbed sandwich complexes were confirmed for the long-chain C_nH-SAM substrates through the analysis of the IRAS and TDS results obtained. Further clarification of the origin of these findings was attempted by examinations of (1) the chain-length effect of the alkanethiolate-SAM matrix on the thermal chemistry of the soft-landed complexes; (2) influence of projectile kinetic energy on resulting adsorption regime of complexes on the SAM substrate. Consequently, it is confirmed that both the orientational preference and the high thermal stability of the complexes are due to the penetration of complexes into the SAM matrix, which could be successfully provided only with hyperthermal collision event of cluster with the SAM surface.

3.2. Experimental section

Details of experimental setup have been described in Chapter 2.1. Transition-metal–benzene sandwich complexes are produced in a molecular beam by laser vaporization. Cation complexes are extracted by a quadrupole deflector and only the $M(benzene)_2$ complexes are size-selected by a quadrupole mass spectrometer (QMS), respectively. The cations are subsequently deposited onto a series of C_nH-SAM (n = 8, 12, 16, 18, 22) substrate, which is cooled to 200 K by a liquid nitrogen cryostat, with an incident energy of ~20 eV. The deposition number of the cations can be determined by monitoring the ion current on the substrate during the deposition time. IRAS spectra for the deposited complexes are obtained with IR incident angle of ~80° with respect to the surface normal.

TDS measurements are carried out with a heating rate of 1 K/s after the complex deposition and the desorption species are detected by another QMS via electron impact ionization (~70 eV). Thermal deposition of $Cr(benzene)_2$ vapor onto the $C_{18}H$-SAM is performed via admission of the sublimed complexes at 300 K to the chamber trough a standard leak valve. The exposures was recorded in Langmuires ($1L = 10^{-6}$ Torr·s) and during the exposure time, the substrate temperature was kept at ~200 K

3.3. Results and Analysis

3.3.1. IRAS spectra of $V(benzene)_2$ complexes

The IRAS spectra in the 700–1500 cm^{-1} region of $V(benzene)_2$ complexes soft-landed on (a) bare gold and (b) $C_{18}H$-SAM substrates at 180 K are shown in Fig. 3.2 as a function of the deposition-number of the complex cations. The deposition of 2.0×10^{14} $V(benzene)_2$ cations per 1 cm^2 seemingly provides an approximate monolayer coverage (i.e. 1 ML). However, the deposition process may be accompanied by recoiling and/or dissociation of the complex ions in the collision with the substrate surface, so that the deposition-numbers presented here correspond to the *apparent* upper limits of the amounts of non-destructively deposited, i.e. "soft-landed", complexes. As shown in Fig. 3.2(a), two adsorption bands at 956 and 988 cm^{-1} start to appear when approximately 1.0×10^{14} cations have been deposited onto the bare gold substrate. In the deposition-number range of $\geq 4.0\times10^{14}$ ions, an additional two bands appear at 747 and 1418 cm^{-1}. In contrast, with a $C_{18}H$-SAM substrate, these four bands can be clearly observed at a much lower deposition-number (i.e. $<1.0\times10^{14}$), suggesting that this substrate permits a rather higher soft-landing efficiency than does the bare gold. The four bands observed for each substrate are in good agreement with the fundamentals reported in IR data for a *neutral* $V(benzene)_2$ complex in an Ar matrix.[8,45] Thus, I can assign the bands as

follows: that at 747 cm^{-1} to a C-H out-of-plane bending [$\nu_{o\text{-}p}$(CH)], 956 cm^{-1} to a symmetric ring-breathing mode [ν_s(CC)], 988 cm^{-1} to the C-H in-plane bending mode [$\nu_{i\text{-}p}$(CH)], and that at 1418 cm^{-1} to the asymmetric C-C stretching mode [ν_a(CC)]. These agreements indicate that the soft-landed V(benzene)$_2$ complex cations lose their charge, and the resulting neutral complexes adsorb on both the substrates with their native sandwich structure intact.

However, the relative intensities of the four bands differ strikingly in the V(benzene)$_2$/gold and the V(benzene)$_2$/C_{18}H-SAM spectra. In particular, the band intensity ratio of 956 to 988 cm^{-1} in the V(benzene)$_2$/gold spectrum completely reverses in the V(benzene)$_2$/C_{18}H-SAM spectrum. Similar spectral feature intensities have also been identified for the other C_nH-SAM substrates (n = 8, 12, 16, and 22).[36] Due to the surface selection rule of IRAS,[46] the relative absorption intensity qualitatively reflects the orientation of an adsorbate on a surface. Thus, the remarkable difference in the relative peak intensities suggests that the adsorption geometry of the complexes on the SAM substrate is different from that on the bare gold.

3.3.2. Estimation of orientation angle of V(benzene)$_2$ complexes on SAM substrates

The V(benzene)$_2$ sandwich complex ideally belongs to the D_{6h} point group, and it can thereby possess two IR-active A_{2u} and E_{1u} symmetry vibrational modes. In fact, the four IR peaks observed herein are due to two A_{2u} modes (747 and 956 cm^{-1}) and two E_{1u} modes (988 and 1418 cm^{-1}). The vibrational modes with A_{2u} symmetry give rise to transition dipoles along the D_{6h} symmetry molecular axis of the V(benzene)$_2$ complex (i.e. along the benzene-V-benzene direction). In contrast, the modes with E_{1u} symmetry arise from dipoles oriented perpendicular to the molecular axis. Owing to the IRAS surface selection rule, only vibrational modes whose transition dipole is perpendicular to the surface are potentially observable in the spectrum. Hence, when the V(benzene)$_2$ complex adsorbs with

its molecular axis perpendicular to the surface, only the A_{2u} modes are expected to be dipole active. At the other extreme, when the complex adsorbs with the molecular axis parallel to the surface, only the E_{1u} modes are observable. In the case of the gold substrate, the IR peak intensity distribution of the A_{2u} and E_{1u} modes is quite similar to that of the V(benzene)$_2$/Ar matrix spectrum (see Fig. 3.2(a)). As the V(benzene)$_2$ complexes isolated in an Ar matrix are randomly oriented in space, the result suggests that the V(benzene)$_2$ complexes are adsorbed with random orientations on the gold surface. For the C_{18}H-SAM substrate, however, a dramatic change is found in the relative IR peak intensity: namely, the two E_{1u} modes at 988 and 1418 cm^{-1} become rather more intense than the two A_{2u} modes at 747 and 957 cm^{-1}. Therefore, it can be expected that the V(benzene)$_2$ complexes that soft-landed onto the C_{18}H-SAM substrate are highly oriented, and that their molecular axis is tilted substantially off the surface normal. The orientation angle of an adsorbate can be semi-quantitatively determined by the RATIO method.[47] With the assumption that all the soft-landed V(benzene)$_2$ complexes are oriented uniformly on the substrate, the *averaged* tilt angle (Θ) of the complexes with respect to the surface normal is given by comparing the intensity ratio of the A_{2u} and E_{1u} modes as follows:[36]

$$\sin^2\Theta = 2/\left\{2+\left[I^{SAM}\left(A_{2u}\right)/I^{SAM}\left(E_{1u}\right)\right]/\left[I^{Ar}\left(A_{2u}\right)/I^{Ar}\left(E_{1u}\right)\right]\right\}, \qquad (3.1)$$

where I^{SAM} represents the IR absorption intensity in the oriented state (i.e. the SAM substrate), and I^{Ar} indicates the corresponding intensity in the random orientation (i.e. the Ar matrix). The analytical results, summarized in Table 3.1, demonstrate the large orientation angles (Θ = 70–80°) of the soft-landed V(benzene)$_2$ complexes on all the SAM substrates examined.

3.3.3. Thermal Desorption Studies of M(benzene)$_2$ complexes

To gain insight into the thermal stability of the soft-landed V(benzene)$_2$ complexes on each substrate, I examined the temperature-induced variations of the IRAS spectra, shown in

Fig. 3.3. The upper traces in Figs. 3.3(a) and (b) depict the IR spectra of the V(benzene)$_2$ complexes on the bare gold and C_{18}H-SAM substrates at 180 K taken after depositions of 5.0 $\times$ 10^{14} and 2.0 $\times$ 10^{14} cations, respectively. In the case of the gold substrate, the intensity reduction begins to occur around 230 K, and the bands completely vanish at 273 K (0 °C). In contrast, all the peaks in the V(benzene)$_2$/C_{18}H-SAM spectra do not decrease in intensity up to 290 K, but they start to decrease very slowly at 298 K (25 °C). After keeping the substrate temperature at 298 K for one hour, the bands at 747, 956, and 988 cm^{-1} are still observed in the spectrum, although the intensities decrease to about 40 % of their initial intensities. Note that once the peak intensities have decreased due to substrate heating, they never return to their initial values, even if the substrate is cooled down again to the initial temperature (180 K). This irreversibility can be reasonably explained by thermal desorption of the adsorbed complexes from the substrates, because the decrement of the IR band intensity starts at the same temperature as the desorption threshold temperature for the TDS spectrum. Below, I show that the desorption temperature of the adsorbed V(benzene)$_2$ complexes on the C_{18}H-SAM substrate is approximately 70 K higher than that on the gold substrate. Although the IRAS spectra clearly indicate the physisorption of the V(benzene)$_2$ complexes on both of the substrates, this result interestingly suggests that the activation energy for the desorption (i.e. adsorption heat) of the adsorbed complexes is much different between these two substrates.

Figure 3.4 shows the substrate-temperature effect on the orientation angles of the supported complexes on the short-chain C_8H-SAM and the long-chain C_{18}H-SAM. For the long-chain C_{18}H-SAM, the average orientation angle of the complexes barely changes (within ±0.5°) below the threshold desorption temperature of ~300 K, a result indicating no change in the adsorption geometry of the complexes remaining on the C_{18}H-SAM substrate. In

contrast, the average orientation angles for the complexes supported on the short-chain C_8H-SAM alter by ±3°, depending on the surface temperature. As will be discussed later, this fluctuation is attributed to the reduced rigidity of the short-chain SAMs.

In the TDS measurements, the deposition-number of the complex ions was set to provide a relatively low coverage of ≤ 0.2 ML (i.e. 4.0×10^{13} ions/cm^2) so that aggregations and interactions between the adsorbed complexes themselves on the substrate might be reduced. Figure 3.5 shows typical TDS spectra for the V(benzene)$_2$ complexes on the gold and the $C_{18}H$-SAM substrates. The desorbed species detected consisted mainly of three kinds of ions: V(benzene)$_2^+$ (*m/z* = 207), V(benzene)$_1^+$ (*m/z* = 129), and benzene$^+$ (*m/z* = 78). It should be noted that these ion signals were not observed in the absence of electron impact ionization in the mass spectrometer, a result explicitly confirming that the soft-landed complex ions are neutralized on the substrates. In the TDS spectra for each substrate, all of the three ions exhibit identical peak shapes; the temperatures of the threshold and maximum desorption are the same. The close similarity between the peak shapes of parent and fragmented species shows that these ions were obtained from a unique ionization process of *neutral* V(benzene)$_2$. Thus, the V(benzene)$_1^+$ and benzene$^+$ ions are produced *not* on the surface, but in the electron impact ionization event of the parent V(benzene)$_2$ complex in the mass spectrometer. For the bare gold substrate, as shown in Fig. 3.5(a), the desorption of the V(benzene)$_2$ complexes starts at ~240 K (i.e. a threshold desorption temperature) and the desorption rate reaches a maximum at ~270 K. The TDS curves display a nearly symmetric shape in which the ion intensity slowly decreases after the peak maximum. In the case of the $C_{18}H$-SAM, however, the desorption temperature and the shape of the TDS curves differ greatly from those of the gold substrate, as shown in Fig. 3.5(b). In good agreement with the IRAS study mentioned in Sec. 3.4, the threshold desorption temperature of the complexes on

the $C_{18}H$-SAM substrate is higher than that on the gold, a finding indicating that the soft-landed complexes are more strongly bound on the $C_{18}H$-SAM substrate than on the gold substrate. Furthermore, the TDS curve for the V(benzene)$_2$/$C_{18}H$-SAM substrate exhibits a sharp decrease after the peak maximum. In general, a peak profile of a TDS spectrum reflects the reaction order of a desorption process.[48,49] Thus, the peak shape difference observed herein suggests that the desorption process of the V(benzene)$_2$ complexes is significantly different between the gold and the $C_{18}H$-SAM substrates. In addition, the integrated areas of the V(benzene)$_2$ TDS spectra, corresponding to the amount of V(benzene)$_2$ complexes deposited intact, is much larger for the $C_{18}H$-SAM than for the gold substrate. The integrated areas of the V(benzene)$_2^+$ peak in the V(benzene)$_2$/C_{16-22}-SAM spectra are typically about ten times larger than that for the gold substrate. As mentioned in Sec.3.2, this result also shows that the SAM matrix can behave as a buffer layer to efficiently reduce the recoils and/or decomposition of the incoming complex ions in the landing process.

The effect of the SAM chain-length on the thermal chemistry of the soft-landed V(benzene)$_2$ complexes was systematically studied by means of TDS measurements. Displayed in Fig. 3.6 are TDS spectra for V(benzene)$_2$ complexes desorbed from C_nH-SAM (with n = 8, 12, 16, 18, and 22) after deposition of 4.0×10^{13} cations of the complexes onto each substrate. For comparison, the TDS spectrum of V(benzene)$_2$/gold is also shown as the upper trace. The threshold desorption temperatures of the complexes on all the SAM substrates are higher than that for the bare gold substrate, and they gradually increase with the chain-length of the SAM. This result demonstrates that the soft-landed complexes are more strongly trapped by longer chain SAMs. In addition, the peak shape of the V(benzene)$_2^+$ signal systematically varies with the chain-length of the SAM. Although an asymmetric shape is observed for the long-chain C_{16-22}-SAMs, a tail at the high-temperature side of the

peak tends to be observed in the V(benzene)$_2$/C$_8$H- and C$_{12}$H-SAM spectra. As discussed later, these results are closely related to the rigidities of the densely packed SAMs.

3.3.4. Arrhenius analysis of TDS spectra

The reaction order and activation energy for the desorption (adsorption heat) of adsorbed complexes can be evaluated through an analysis of their TDS profiles. On a solid surface, the desorption rate equation (the Polanyi-Wigner equation) of adsorbates is given by

$$\ln k_d = \ln\left[\left(-\frac{d\theta}{dt}\right)\Big/\theta^n\right] = \ln \nu_d - \frac{E_d}{RT}, \qquad (3.2)$$

where k_d is the desorption rate constant, θ is the coverage, n is the reaction order, ν_d is a pre-exponential factor, and E_d is the adsorption heat.[50] The observed TDS profile provides the desorption rate ($-d\theta/dt$) and the coverage (θ), so that if a correct reaction order value, n, is chosen, a plot of $\ln k_d$ versus $1/T$ (i.e. an Arrhenius plot) should be linear. However, when an incorrect value of reaction order, m, is substituted, the expression possesses an additional term containing θ, as in the following:[48]

$$\ln\left[\left(-\frac{d\theta}{dt}\right)\Big/\theta^m\right] = \ln \nu_d - \frac{E_d}{RT} + (n-m)\ln\theta\,. \qquad (3.3)$$

This Arrhenius plot does not retain its linearity because θ is not linear with respect to $1/T$. In this analysis, four different reaction order values (n = 0, 0.5, 1, and 2) were examined to find the correct reaction order, n.

Figure 3.7 shows the Arrhenius plots for the TDS spectra of the V(benzene)$_2$ complexes desorbed from the bare gold, C$_8$H-SAM, and C$_{18}$H-SAM substrates. Linear plots were obtained only for a reaction order of n = 2 for the gold substrate [Fig. 3.7(a)] and n = 1 for the C$_{18}$H-SAMs [Fig. 9(c)], while the plots obtained using other values were non-linear in the high temperature range (i.e. small $1/T$). The slope of the linear fit yielded a value of 64 ± 13

kJ/mol for the adsorption heat of the complexes on the bare gold. In the case of the $C_{18}H$-SAM, the adsorption heat was determined to be 138 ± 21 kJ/mol, comparable to the typical adsorption heat of chemisorption (~100 kJ/mol). For the long-chain $C_{16}H$- and $C_{22}H$-SAMs, linear plots were also obtained with a reaction order of n = 1, just as for the $C_{18}H$-SAM. As shown in Fig. 3.7(b), however, a linear plot could not be obtained for any value of n for the shorter chain C_8H- and $C_{12}H$-SAMs, a finding indicating that the desorption rate does not necessarily follow the simple desorption model of the Polanyi-Wigner equation [Eq. (3.2)]. Thus, in the case of the C_8H- and $C_{12}H$-SAMs, the adsorption heats were determined from the slope of the relatively large $1/T$ region where the plot is approximately linear and has the same slope for all choices of n.[51] The adsorption heats (E_d) thus obtained are also listed in Table 3.1.

3.4. Discussion

3.4.1. Soft-landing Isolation Regime

The IRAS results confirmed that $V(benzene)_2$ complexes are non-dissociatively adsorbed on both the gold and SAM substrates, and retain the D_{6h} sandwich structure. On each substrate, furthermore, the IR absorption frequencies of the soft-landed $V(benzene)_2$ cations are in good agreement with those of their *neutral* complex[8,45] but are different from those of the cation in gas-phase,[5] results indicating that the $V(benzene)_2$ cations are neutralized in the landing process by electron transfer from the substrates. Indeed, the average ion currents during the complex cation deposition did not change between those for the gold and for the alkanethiolate-SAM substrates. It has been reported that a highly polar, fluorinated SAM can suppress the neutralization of projectile ions at the surface and trap the deposited ion intact,[30–32,52] however, such an effect is unlikely for the alkanethiolate-SAMs.

On an Au(111) surface at low temperature, the previous IRAS study revealed that a benzene molecule preferentially adsorbs in a "flat-lying" geometry with the molecular plane parallel to the surface plane due to interactions of the benzene π orbitals with the gold surface.[53] Thus, the V(benzene)$_2$ complexes might also prefer to adsorb via the flat-lying geometry where the capping benzene rings of the complex are parallel to the gold surface. When the V(benzene)$_2$ adsorbs in this manner, only the A_{2u} modes at 747 and 956 cm^{-1} should be IR active on the gold surface, because of the surface selection rule. Furthermore, the bonding interaction of the benzene π orbitals with the gold surface should lead to a frequency shift of the vibrational modes of the benzene ring. Indeed, the frequency of the $\nu_{o\text{-}p}$(CH) mode of benzene adsorbed on a Au(111) surface in this geometry is shifted more than 10 cm^{-1} to higher frequency than that of free benzene.[53] However, the V(benzene)$_2$/gold IRAS spectra observed herein clearly display both the A_{2u} modes at 747 and 956 cm^{-1} and the E_{1u} modes at 988 and 1418 cm^{-1} with the remaining vibrational frequencies corresponding to those of the condensed-phase observed in an Ar matrix.

This finding suggests that the complexes adsorb in random orientations on the gold surface, possibly because of facile surface diffusion of the adsorbed complexes. The surface diffusion of adsorbates has often been observed on a metal surface, because the potential barrier for the lateral motion of adsorbates on a metal surface is usually small enough to permit diffusion, except at extremely low temperatures.[54,55] Hence, the complexes diffuse on the surface as two-dimensional gases, and can form islands of the complexes at step and defect sites existing on the gold surface at the relatively high surface temperature of 180 K. Such adsorption states exhibit an apparently random orientation on the surface, and generate the IR bands of both the A_{2u} and E_{1u} vibrational modes in the IRAS spectra. Consequently, the IRAS spectra for the V(benzene)$_2$/gold are identical to the IR spectra of V(benzene)$_2$ in a

Ar matrix where the complexes are randomly oriented in space.

The thermal desorption studies also support the occurrence of surface diffusion of the complexes on the surface. As noted above, the desorption of the adsorbed $V(benzene)_2$/gold complexes is second-order. Although second-order desorption kinetics is often characterized by a recombination desorption of dissociatively-adsorbed molecules,[46,50,51] the IRAS study shows that the soft-landed complexes adsorb molecularly on the gold surface. I have also confirmed that the fragments of $V(benzene)_2$, i.e. benzene and $V(benzene)_1$, which are produced in the landing process, desorb from the gold substrate well below 180 K. Thus, such a recombination process is ruled out in the present second-order desorption kinetics. Another plausible origin of the second-order kinetics of adsorbates is their surface diffusion, which can produce a long tail in the high temperature side of the TDS peaks.[49] For example, Vogt *et al*. reported that the TDS spectra for alcohol molecules adsorbed on SAMs display a second-order desorption (or symmetric) profile due to their diffusion on the SAM surfaces.[56] It is conceivable that the surface diffusion of the complexes leads to a random orientation in the desorption process, and that the IRAS spectra for the $V(benzene)_2$/gold represent the random orientation of the complexes at any surface temperature.

Both the IRAS and TDS results demonstrate that the adsorption regime of the $V(benzene)_2$ complexes on the SAMs is very different from that on the bare gold surface; namely, a highly oriented geometry as well as higher thermal stability (i.e. larger adsorption heats) were obtained for the complexes supported on the SAM substrates. These results suggest that some significant physical effects at play in $V(benzene)_2$ adsorption on the SAM substrates. As mentioned in Sec. 3.3, the analysis of the IRAS spectra shows that the $V(benzene)_2$ complexes are trapped with large orientation angles of $\Theta = 70–80°$ on the $C_{18}H$-, and $C_{22}H$-SAM substrates. When the $V(benzene)_2$ complexes are adsorbed on the outermost

methyl-groups of the alkanethiolate-SAMs, the complexes may prefer the adsorption geometry in which their molecular axes are perpendicular to the surface (Θ = ~0°), because such geometry effectively involves an attractive CH-π interaction between one of the capping benzene rings of the complex and the outermost methyl-groups. However, if the V(benzene)$_2$ complexes are incorporated in the SAM matrix, the complexes should interact with the hydrogen atoms of the lateral methylene groups of the surrounding alkanethiolate molecules. In this case, the molecular axis of the V(benzene)$_2$ molecules may be tilted considerably off the surface normal because of the methylene CH-benzene π interaction. Hence, the large orientation angles (Θ = 70–80°) obtained herein suggest penetration of complexes into the SAMs.

The TDS results for the V(benzene)$_2$/C$_n$H-SAMs are also consistent with the complex-penetration model. While second-order desorption kinetics were observed for the gold surface, the complexes supported on the long-chain C$_n$H-SAMs with $n \geq 16$ display first-order desorption kinetics. They do so because the thermal desorption of the complexes trapped inside the long-chain SAMs can be regarded as a one-way diffusion into the SAM matrix. Such thermal desorption produces the following first-order desorption rate equation:[57]

$$-\frac{d\theta}{dt} = \nu_D \theta \exp\left(-E_D/RT\right) = k_D \theta \qquad (4)$$

where ν_D is the pre-exponential factor and E_D is the activation energy for escaping from the inside of the SAM. Note that E_D corresponds to the adsorption heat (E_d) of the complexes soft-landed onto the C$_n$H-SAM substrates.

The kinetic energy distribution of the incident V(benzene)$_2$ complex were estimated to be ~20 eV at full-width half-maximum (FWHM) in this study. Thus, a small amount of the complexes deposited with low kinetic energy (< 1 eV) might possibly land right on the methyl surface of the SAM matrix, being weakly physisorped *on* the methyl surface. However, I

observed only one peak in the TDS spectra as well as a progressive shift to higher desorption temperature with the chain-length, indicating that there was mainly one desorption state for the SAM-trapped complexes. Therefore, I could evaluate that the quantity of the complexes physisorbed on the methyl surface of the SAM matrix was negligible.

Like the desorption process from the long-chain $C_{16–22}$-SAMs, that of the complexes incorporated in the short-chain C_8H- and $C_{12}H$-SAMs is also expected to exhibit first-order desorption kinetics. However, the TDS spectra for the short-chain SAMs did not follow the Arrhenius equation, exhibiting non-linear desorption kinetics. This unusual desorption kinetics may originate in the reduced rigidity of the shorter chain SAMs. For the long-chain SAM, as is well known, a strong lateral van der Waals interaction between the alkanethiolates on the gold surface results in the "rigid" crystalline-phase SAM. However, the magnitude of the interaction decreases as the chain-length shortens, so that the short-chain SAMs become less rigid.[58,59] As shown in Fig. 3.4, the average orientation angle of the complexes penetrated in the $C_{18}H$-SAM is not influenced by the substrate temperature, pointing to the immobility of the complexes trapped in the "rigid" long-chain SAM. In contrast, an orientation angle fluctuation, which exceeds the experimental uncertainty, was identified for the short-chain C_8H-SAM. This result probably implies a relatively high mobility for the complexes trapped in the short-chain SAM, which could be caused by the fluxional behavior of the "less-rigid" SAM produced as the substrate temperature rises. The thermal desorption from the less-rigid matrix might not obey the simple desorption model of the Arrhenius equation, and might result in the non-linear desorption kinetics.

The temperature dependence of the IRAS spectrum for the V(benzene)$_2$/$C_{18}H$-SAM [see Fig. 3.3(b)] shows that the IR peaks due to the V(benzene)$_2$ complexes remain in the IRAS spectrum around room temperature, a finding which can be now ascribed to the large

adsorption heat (>1 eV) of the SAM-incorporated V(benzene)$_2$ complexes. In general, such a large adsorption heat is limited to chemisorbed adsorbates. However, the present study demonstrates that the V(benzene)$_2$ complexes can be trapped *physically* in the void spaces among the encompassing alkyl-chains of the SAM, yielding an unusually large adsorption heat which is comparable to or greater than the adsorption heat of chemisorptions. This novel physisorption state, furthermore, can keep the supported complexes largely intact in the SAM matrix, while chemisorptions usually are accompanied by structural strains or dissociations of the adsorbates due to the strong chemical perturbation generated by the surface.

3.4.2. Infulence of variety of transition metals in the complex

Considerable experimental and theoretical studies have revealed that the characteristics of the transition-metal–benzene complexes, including geometry, stability, optical and magnetic properties, are highly depending on the variety of the transition metals, i.e. change in number of 3*d* electrons, in the complexes. I therefore herein demonstrate the influence of alternation of the metals in the complexes on their deposition process as well as resulting adsorption properties and thermal chemistry after the soft-landing onto the SAM matrix.

Figure 3.8 shows the IRAS spectra in the 650–1550 cm^{-1} region after the soft-landing of M(benzene)$_2$ cation complexes (M = Ti, V, and Cr) onto the C_{18}H-SAM substrates along with the IR fundamentals of neutral complexes in the condensed phase. For each sandwich complex, the peak positions of these IR absorption bands is in good agreement with the IR fundamentals[8,45,60] for the *neutral* sandwich complexes in an Ar matrix or KBr pellet. These agreements indicate that all the soft-landed M(benzene)$_2$ cation complexes lost their charge, and the resulting neutral complexes adsorb on the SAM substrate with their native sandwich structure intact. The vibrational assignments for observed IR bands for each M(benzene)$_2$

complexes are summarized in Table 3.2. In the measurement, the collision energy of the complexes toward the substrates was set to 20 eV for V(benzene)$_2$ and Cr(benzene)$_2$. For Ti(benzene)$_2$, however, the 2.0×10^{14} cation deposition with the collision energy of 20 eV provides no IR signal, suggesting that the collision-induced dissociation of Ti(benzene)$_2$ occurs efficiently in the landing process. Thus, the collision energy was reduced to 10 eV in order to suppress the dissociation.

The dissociative deposition for Ti(benzene)$_2$ at 20-eV collision energy is mostly originating from the decrease in the binding energy (with respect to a metal atom and two benzene molecules) of incoming Ti$^+$(benzene)$_2$ complexes as compared to that of V$^+$(benzene)$_2$ and Cr$^+$(benzene)$_2$ complexes. The magnitude of the binding energy can be characterized by electronic configurations of the cationic complexes. The low energy electronic states were theoretically provided as a doublet state of $^2A_{1g}(e_2^4, a_1^1)$ for Cr$^+$(benzene)$_2$ in the D_{6h} symmetry, and as a triplet state of $^3B_{3g}(e_2^3, a_1^1)$ for V$^+$(benzene)$_2$, and two nearly degenerated states of $^2A_g(e_2^3, a_1^0)$ and $^2B_{3g}(e_2^2, a_1^1)$ for Ti$^+$(benzene)$_2$ in the distorted D_{2h} conformation, where e_2 is bonding and a_1 is nonbonding orbital, respectively.[5,6] The dissociative deposition for Ti(benzene)$_2$ at 20-eV, obtained herein, suggests that the small bond-order state of $^2B_{3g}(e_2^2, a_1^1)$ might be adopted for the incident Ti$^+$(benzene)$_2$ complexes.

In the IRAS spectra, in addition, it should be emphasize that the predominant observation of E_{1u} modes with respect to A_{2u} modes is measured for all the M(benzene)2 complexes soft-landed on the C_{18}H-SAM substrate. The *averaged* tilted angle (Θ) of the Cr(benzene)$_2$ and Ti(benzene)$_2$ complexes with respect to the surface normal is estimated to be Θ = ~74° for Ti(benzene)$_2$, and Θ = ~67° for Cr(benzene)$_2$, respectively, values which are roughly same as that for V(benzene)$_2$ of Θ = ~72°. Similar orientational preferences are obtained for every early transition-metal–benzene complexes soft-landed on the SAM

substrate. The results strongly support that the most presumable origin to make the orientation is, therefore, extremely weak attractive CH-π interaction between the capping benzene rings of the complex and the hydrogen atoms of methylene groups of the surrounding *n*-octadecanthiolate molecules. Usually, chemical interaction involving charge transfer between adsorbates and a substrate causes frequency shift in vibrational spectra of the adsorbates, however, I obtained no frequency shift in the vibration of the complexes after the soft-landing. It has been reported that the CH-π interaction energy is very small (~6 kJ/mol) as compared to the other hydrogen-π interactions (e.g. OH-π, NH-π).[61–63] Thus, such weak CH-π interaction would only effect to orient the sandwich complexes inside the SAM matrix but make any frequency shift in the vibrations of the complexes after the incorporation.

3.4.3. Dependence of Deposition Energy on Resulting Isolation Regime

We examined physical vapor deposition (PVD) study of a $Cr(benzene)_2$ vapor to gain insight into the deposition process and resulting adsorption regime of the soft-landed $M(benzene)_2$ complexes on the SAM substrate by comparing the resulting adsorption state after the PVD. At room temperature, as mentioned above, the mean kinetic energy of the thermally vaporized $Cr(benzene)_2$ is estimated to be ~25 meV which is much smaller than the kinetic energy of soft-landed species (~20 eV).

The IRAS spectra in the low frequency (650–1550 cm^{-1}) and high frequency (2700–3100 cm^{-1}) regions of thermally deposited $Cr(benzene)_2$ complexes on the $C_{18}H$-SAM substrate at several coverage are shown in Figure 3.9. After exposure of 2 L, I observed five IR absorption bands originating from the vibrational modes of the $Cr(benzene)_2$ complex. Note that additional high frequency mode at 3043 cm^{-1} is attributed to in-plane CH stretching mode of capping benzene rings. The IR spectral feature, i.e. peak position and relative intensity, for $Cr(benzene)_2$ deposited on the $C_{18}H$-SAM is in good agreement with the

aforementioned IR fundamentals for the $Cr(benzene)_2$ complexes in a solid-state KBr pellet, indicating that the Cr(benzene) complexes are molecularly adsorbed on the SAM substrate. Furthermore, since orientation of the $Cr(benzene)_2$ complexes should be totally randomized in the KBr pellet, the analogy of relative IR intensity suggests that the thermally deposited complexes are randomly oriented on the SAM substrate. As mentioned above, the hyperthermally deposited complexes are highly oriented on the SAM substrate, therefore, the random-orientation indicates that adsorption state of thermally deposited $Cr(benzene)_2$ complexes is different from that of soft-landed complexes on the SAM substrate. Such random-orientation behavior is also observed for $Cr(benzene)_2$ and $V(benzene)_2$ complexes physisorbed on a bare gold surface. Thus, it is expected that the thermally deposited complexes may be physisorbed on the surface of the SAM matrix.

Displayed in Figure 3.10 is the IRAS spectra for the $Cr(benzene)_2$ complexes soft-landed on the $C_{18}H$-SAM substrate at 200 K with hyperthermal collision energy of ~20 eV, as a function of the deposition-number of the $Cr(benzene)_2$ cations. As shown in Figure 3.10, three absorption bands originating from E_{1u} modes at 997, 1429 and 3044 cm^{-1} are first appeared until 8×10^{13} cations have been deposited onto the substrate. At the deposition number of 2.0×10^{14} ions, an additional A_{2u} mode is clearly observed at 972 cm^{-1}. In addition, I observed negative IR peaks in high frequency region after the soft-landing of the complexes. The peak positions of these negative peaks are assignable to vibrational frequencies of the CH stretching modes for alkanethiolate molecules within $C_{18}H$-SAM (see Table 2.2). In this study, I recorded the background IR spectra before the depositions of complexes so that the negative peaks in measured IR spectra represent decrease in IR absorption intensity of the CH stretching modes for alkanethiolate molecules. The negative peak intensities grow with the deposition-number of the $Cr(benzene)_2$ complexes, suggesting

penetration of the complexes into the $C_{18}H$-SAM matrix due to high-energy collision impact in the soft-landing process. The penetration probably causes some structural disordering for the well-ordered SAM by collision-induced desorption and collision-induced migration. In the case of thermal deposition, contrastively, no negative peak was observed in the IRAS spectra after the exposure of the $Cr(benzene)_2$ vapor, showing no significant change in the SAM structure. This result can be attributed to the weak physisorption of the complexes on a methyl-surface of the SAM. Using scanning tunneling microscopy, in fact, Kandel and co-workers recently showed that collision of 1.3-eV xenon atoms with alkanethiol monolayer on Au(111) can cause frequent changes in position and orientation of alkanethiols in the monolayer.[64]

In order to evaluate the thermal stability of thermally deposited and soft-landed $Cr(benzene)_2$ complexes on the $C_{18}H$-SAM substrate, I examined the temperature-induced variations of the IRAS spectra, as shown in Figure 3.11. The upper traces in Figs. 3.11(a) and (b) represent the IR spectra of the $Cr(benzene)_2$ complexes on the $C_{18}H$-SAM substrates at 200 K taken after thermal deposition of 4 L via PVD method and soft-landing of 2.0×10^{14} cations, respectively. In the case of the thermally deposited complex, the IR intensity reduction begins to occur around 240 K, and the bands completely vanish at 260 K. These IR bands never return to their initial intensity, even if the substrate is cooled down again to the initial surface temperature of 200 K so that decrease in IR intensity reflects thermal desorption of the adsorbed complexes from the SAM substrates. In high frequency region of the spectra, furthermore, negative IR peaks attributed to the CH stretching of alkanethiols within the SAM were produced with increase in surface temperature. Growth of negative peaks i.e., decrease in the peak intensities, reflects changing the tilted angle of alkyl chains of the SAM with the surface temperature.[65,66] Indeed, when the substrate is cooled down to

200 K again, these negative peaks disappear and the tilted angle returns the initial state.

For the soft-landed complexes, in contrast, all the IR peaks in the spectra start to decrease at a much higher temperature of 280 K and completely vanished at 300 K. Namely, the desorption temperature of the soft-landed $Cr(benzene)_2$ complex is approximately 40 K higher than that of thermally deposited complex on the $C_{18}H$-SAM substrate. This high thermal stability would be produced by incorporation of the complexes inside the SAM matrix. When the substrate is cooled down to 200 K after the thermal desorption of the soft-landed complexes, the negative IR peaks in high frequency region remain. In this measurement, as mentioned above, the background of the IRAS spectra is recorded before the deposition of complexes so that this signifies that the collision-induced desorption and/or dissociation of alkanethiols within the SAM matrix takes place during hyperthermal collision events.

The thermal desorption kinetics of the $M(benzene)_2$ complexes supported on the SAM substrates can be evaluated by the TDS study in detail. Figure 3.12 shows the TDS spectra for $Cr(benzene)_2$ complexes on the $C_{18}H$-SAM substrates. In order to reduce the aggregations and interactions between the adsorbed complexes themselves on the substrate, in this TDS measurement, the deposition number of the landed complexes was set to provide a relatively low coverage.

The upper trace of the Fig. 3.12 depicts a typical TDS spectrum of the $Cr(benzene)_2$ complex on the $C_{18}H$-SAM taken after the exposure of 1 L. The thermal desorption of the supported complexes starts ~230 K and the desorption rate reaches maximum at ~265 K. The TDS curve displays a nearly symmetric shape in which the ion intensity slowly decreases after the peak maximum to have a long tail on their high-temperature side. The identical feature was also observed for the TDS spectrum of physisorbed $V(benzenen)_2$ complexes on a

gold surface, indicating that thermally deposited Cr(benzene)$_2$ complexes are physisorbed on a methyl-surface of the SAM. The illustration of the long tail in the high-temperatures reflects surface diffusion of the complexes on the SAM surface. Such surface diffusion of the complexes would bring about a random orientation in the desorption process, the IRAS spectra for the Cr(benzene)$_2$/C_{18}H-SAM after the PVD then represent the random orientation of the complexes at any surface temperature

The TDS spectra of the Cr(benzene)$_2$ complexes after the soft-landing of 4×10^{13} ions/cm^2 ($\leq$ 0.2 ML) onto C_{18}H-SAM are also displayed in Fig. 3.12, where the TDS spectra of the soft-landed V(benzene)$_2$, and Ti(benzene)$_2$ complexes are displayed as reference. The desorption spectra for all the metal-benzene sandwich complexes illustrate identical spectral feature, indicating that a similar desorption process have occurred for these M(benzene)$_2$ complexes. However, a pronounced difference in the TDS spectral feature was obtained between the soft-landed complexes and the thermally deposited Cr(benzene)$_2$ complexes. For each soft-landed complex, the thermal desorption starts ~290 K and the desorption rates reach maxima at ~310 K. The dramatic increase in desorption temperature provides conclusive evidence that the soft-landed complexes are more strongly bounded on the SAM substrate than the complexes thermally deposited via the PVD method. Furthermore, the TDS curves for the soft-landed complexes illustrate asymmetric peak profiles in which the desorption rate rapidly decrease after the peak maximum. This result demonstrates that the soft-landed complexes desorb from the C_{18}H-SAM substrate via a first order desorption kinetics: namely, the thermal diffusions of the complexes in the desorption process are effectually inhibited. Thus, these TDS results clearly show that the soft-landed complexes do not physisorb on the surface of the SAM matrix. The increase in desorption temperature and the first order desorption kinetics provided herein strongly support the incorporation of

the M(benzene)$_2$ complexes inside the SAM matrix (i.e. matrix-isolation regime) after their soft-landing with hyperthermal collision energy.

The activation energy for desorption of the complexes supported by the SAM substrates can be quantitatively determined by taking Arrhenius plots of the measured TDS spectra. For the Cr(benzene)$_2$ complexes on C_{18}H-SAM substrate after the PVD, the desorption activation energy was calculated to be 71 ± 12 kJ/mol. This value is comparable to the desorption activation energy for the V(benzene)$_2$ complexes physisorbed on a gold surface of 64 ± 13 kJ/mol. This similarity of the desorption activation energy indicates that the desorption activation energies of the complexes predominately originate form van der Waals interactions between the complex and the surfaces, because the interactions between the complexes and a gold surface is regarded as van der Waals ones. In contrast, the M(benzene)$_2$ complexes soft-landed on the C_{18}H-SAM matrix obtain much larger desorption activation energies. As listed in Table 3.3, the activation energies reach typical adsorption heats of chemisorption state (commonly >100 kJ/mol) for all the M(benzene)$_2$ complexes supported on the C_{18}H-SAM substrates after the soft-landing.

3.4.4. Effect of Alkyl-Chain Length of Matrices on Thermal Chemistry of Soft-Landed Complexes

The study of the alkyl-chain length effect on desorption activation energy of the V(benzene)$_2$ complexesoft-landed on the C_nH-SAM matrices. As shown in Figure 3.13, the activation energy almost linearly increases with the chain length of the SAM. This linear increment is quite analogous to dependency of enthalpy of phase transitions for condensed-phase *n*-alkanes on their chain length,[67,68] for instance, their enthalpy of fusion is also plotted in Fig. 3.13. This similarity suggests that the thermal desorption of the matrix-isolated complexes may be associated with such phase-transitions of alkyl-chains within the SAM matrix.

For *n*-alkanes, between the crystalline (solid) phases and liquid phase exist a series of weakly ordered plastic crystalline phases, so-called the "rotator phase", due to the lack of long-range order in the rotational degree of freedom of their long alkyl-chains.[69-71] Skinner and co-workers characterized the transition enthalpy at the crystal–rotator transition (ΔH_T) as well as the fusion enthalpy at the rotator–liquid transition (ΔH_F) of *n*-alkanes in the C_{17} to C_{36} range.[68] They discovered that the ΔH_T also increases monotonically as the chain length growth with the identical slope of ΔH_F toward the chain length, while the value of ΔH_T is about one-half of that of ΔH_F.

In the case of the *n*-alkanethiol SAM below room temperature, the normal alkyl-chains are mostly linear (i.e. all-*trans* conformation) to enhance the chain-chain packing, however, the rotator structure of alkyl-chains can be also observed, called *gauch* conformational defects, above room temperature region.[65,66,72] The advent of the rotator phase can be nicely followed by probing the influence of temperature on infrared spectra of the SAM.[65,66] Figure 3.14(a) shows the temperature-induced variations of the IRAS spectra for the C_{18}H-SAM substrate used for this soft-landing experiments, and the plots of integrated intensity of the d^- mode at 2918 cm^{-1} (C–H asymmetric stretching) toward the substrate temperature is displayed in Fig. 3.14(b). The peak intensity of d^- mode decreases with the slope of -3×10^{-4}% per kelvin up to ~300 K, induced by a decrease in tilted angle of the alkyl chains,[72–74] nonetheless, the intensity grossly decreases above 300 K with the slope of -7×10^{-4}% per kelvin. This decrement is caused by appearance of *gauch* conformational defects[66,75,76] so that the phase transitions of the highly ordered phase (crystal phase) to rotator phase takes place around 290 K for the C_{18}H-SAM substrate used in this study. This phase-transition temperature is, as well, fairly close to the threshold desorption temperature of complexes supported on the C_{18}H-SAM substrate (~290 K). Thus, the crystal–rotator phase

transitions of the $C_{18}H$-SAM matrix probably assist in release of the trapping captured sandwich complexes from the SAM matrix.

Although there is no report that determines the value of enthalpy at the crystal–rotator phase transitions of *n*-alkanethiol SAMs, it is estimated to be ~30 kJ/mol for *n*-alkane whose chain length is around $n = 20$.[68,77] Compounding the *physisorption energy* of the complexes with surround alkyl chains in the SAM matrix and *enthalpy* at the crystal–rotator phase transitions of the SAMs would provide unusual large activation energy for desorption in this thermal desorption study. As a consequence, use of an organic surface, the enthalpy at phase transitions of which is considerably large, as a supporting matrix can realize dramatic enhancement in thermal stability of the trapping captured complexes.

5. Conclusion

$V(benzene)_2$ complex cations produced in the gas-phase have been soft-landed onto a bare gold surface and various chain-length (C_8H- to $C_{22}H$-) SAMs of *n*-alkanethiols. The C_nH-SAM species is found to serve as an excellent inert buffer matrix to discourage the decomposition of the neutralized $V(benzene)_2$ complex in a soft-landing process, similar to a rare gas matrix. The high incident energy of 20 eV in the soft-landing process results in the penetration of the complexes into the C_nH-SAM matrix. The incorporated complexes are highly oriented with their molecular axis canted 70–80° off the surface normal, a phenomenon which is probably due to the attractive CH-π interaction between the capping benzene rings of the complex and the lateral methylene groups of the alkanethiolates. In addition, the adsorption heat of the complexes penetrating into the C_nH-SAM increases with the chain-length of the SAM. The $V(benzene)_2$ complexes penetrating into the long-chain SAMs possess unusually large adsorption heats, comparable to a typical adsorption heat of

chemisorption, so that the thermal desorption of the complexes is suppressed, even at room temperature. In such a chemically unperturbed adsorption regime, the $M(benzene)_2$ complexes can retain the native 1D sandwich conformation; thus, it can be anticipated that they largely keep their intrinsic electronic and ferromagnetic properties in the SAM matrix.

The room-temperature isolation of gas-phase complexes succeeded in this study provides an advance, which opens up a new opportunity to study various properties of the complex-based materials by combining conventional surface science techniques. Furthermore, controlling the orientation of the anisotropic 1D sandwich complexes by means of the SAM matrix presented here illustrates that an understanding of the issues pertaining to the interactions between the deposited complexes and the support substrate will facilitate a fine-tuning of the complex functionality on the substrate.

Reference

1. Hoshino, K.; Kurikawa, T.; Takeda, H.; Nakajima, A.; Kaya, K. *J. Phys. Chem.* **1995**, *99*, 3035−3055.
2. Nakajima, A.; Kaya, K. *J. Phys. Chem. A* **2000**, *104*, 176−191.
3. Meyer, F.; Khan, F. A.; Armentrout, P. B. *J. Am. Chem. Soc.* **1995**, *117*, 9740−9748.
4. Weis, P.; Kemper, P. R.; Bowers, M. T.; *J. Phys. Chem. A* **1997**, *101*, 8207−8213.
5. van Heijnsbergen, D.; von Helden, G.; Meijer, G.; Maitre, P.; Duncan, M. A. *J. Am. Chem. Soc.* **2002**, *124*, 1562−1563.
6. Jaeger, T. D.; van Heijnsbergen, D.; Klippenstein, S. J.; von Helden, G.; Meijer, G.; Duncan, M. A. *J. Am. Chem. Soc.* **2004**, *126*, 10981−10991.
7. Jaeger, T. D.; Pillai, E. D.; Duncan, M. A. *J. Phys. Chem. A* **2004**, *108*, 6605−6610.
8. Lyon, J. T.; Andrews, L. *J. Phys. Chem. A* **2005**, *109*, 431−440.
9. Wang, J.; Jellinek, J. *J. Phys. Chem. A* **2005**, *109*, 10180−10182.
10. Yasuike, T.; Yabushita, S. *J. Phys. Chem. A* **1999**, *103*, 4533−4542.
11. Pendy, R.; Rao, B. K.; Jena, P.; Blanco, M. A. *J. Am. Chem. Soc.* **2001**, *123*, 3799−3808.
12. Kandalam, A.K.; Rao, B. K.; Jena, P.; Pandey, R. *J. Chem. Phys.* **2004**, *120*, 10414−10422.
13. Miyajima, K.; Nakajima. A.; Yabushita, S.; Knickelbein, M. B.; Kaya, K. *J. Am. Chem. Soc.* **2004**, *126*, 13202.
14. Wang, J.; Acioli, P. H.; Jellinek, J. *J. Am. Chem. Soc.* **2005**, *127*, 2812−2813.
15. Heiz, U.; Schneider, W. -D. *J. Phys. D* **2000**, *33*, R85−R102.
16. Heiz, U.; Bullock, E. L. *J. Mater. Chem.* **2004**, *14*, 564−577.
17. Yoon, B.; Häkkinen, H.; Landman, U.; Wörz, A. S.; Antonietti, J. -M.; Abbet, S.;

Judai, K.; Heiz, U. *Science*, **2005**, *307*, 403–407.

18. Dürr, H. A.; Dhesi, S. S.; Dudzik, E.; Knabben, D.; van der Laan, G.; Goedkoop, J. B.; Hillebrecht, F. U. *Phys. Rev. B* **1999,** *59*, R701–R704.
19. Edmonds, K. W.; Binns, C.; Baker, S. H.; Maher, M. J.; Thornton, S. C.; Tjernberg, O.; Brookes, N. B. *J. Magn. Magn. Mater.* **2001**, *231*, 113–119.
20. Moseler, M.; Häkkinen, H.; Landman, U. *Phys. Rev. Lett.* **2002**, *89*, 176103.
21. Ouyang, Z.; Takáts, Z.; Blake, T. A.; Gologan, B.; Guymon, A. J.; Wisemen, J. M.; Oliver, J. C.; Davisson, V. J.; Cooks, R. G. *Science* **2003**, *301*, 1351–1354.
22. Washburn, M. P. *Nature Biol.* **2003**, *21*, 1156–1157.
23. Gologan, B.; Takáts, Z.; Alvarez, J.; Wisemen, J. M.; Talaty, N.; Ouyang, Z.; Cooks, R. G. *J. Am. Soc. Mass Spectrom.* **2004**, *15*, 1874–1884.
24. Judai, K.; Sara, K.; Amatsutsumi, S.; Yagi, K.; Yasuike, T.; Yabushita, S.; Nakajima, A.; Kaya, K. *Chem. Phys. Lett.* **2001**, *334*, 277–284.
25. Cheng, H. -P. Landman, U.; *Science* **1993**, *260*, 1304–1307.
26. Bromann, K.; Felix, C.; Brune, H.; Harbich, W.; Monot, R.; Buttet, J.; Kern, K. *Science* **1996**, *274*, 956–958.
27. Pugmire, D. L.; Woodbridge, C. M.; Boag, N. M.; Langell, M. A. *Surf. Sci.* **2001**, *472*, 155–171.
28. Blass, P. M.; Akhter, S.; Seymour, C. M.; Lagowski, J. J.; White, J. M.; *Surf. Sci.* **1989**, *217*, 85–102.
29. Welipitiya, D.; Dowben, P. A.; Zhang, J.; Pai, W. W.; Wendelken, J. F. *Surf. Sci.* **1996**, *367*, 20–32.
30. Miller, S. A.; Luo, H.; Pachuta, S. J.; Cooks, R. G. *Science* **1997**, *275*, 1447–1450.
31. Luo, H; Miller, S. A.; Cooks, R. G.; Pachuta, S. J. *Int. J. Mass Spectrom. Ion*

Processes **1998**, *174*, 193–217.

32. Gologan, B; Green, J. R.; Alvarez, J.; Laskin, J.; Cooks, R. G. *Phys. Chem. Chem. Phys.* **2005**, *7*, 1490–1500.
33. Day, B. S.; Shuler, S. F.; Ducre, A.; Morris, J. R. *J. Chem. Phys.* **2003**, *119*, 8084–8096.
34. Bosio, S. B. M.; Hase, W. L. *J. Chem. Phys.* **1997**, *107*, 9677–9686.
35. Yan, T.; Isa, N.; Gibson, K. D.; Sibener, S. J.; Hase, W. L. *J. Phys. Chem. A* **2003**, *107*, 10600–10607.
36. Mitsui, M.; Nagaoka, S.; Matsumoto, T.; Nakajima, A. *J. Phys. Chem. B* **2006**, *110*, 2968–2978.
37. Schreiber, F. *Prog. Surf. Sci.* **2000**, *65*, 151–256.
38. Love, J. C.; Estroff, L. A.; Kriebel, J. K.; Nuzzo, R. G.; Whitesides, G. M. *Chem. Rev.* **2005**, *105*, 1103–1169.
39. Dubois, L. H.; Zegarski, B. R.; Nuzzo, R. G. *J. Am. Chem. Soc.* **1990**, *112*, 570–579.
40. Linford, M. R.; Fenter, P.; Eisenberger, P. M.; Chidsey, C. E. D. *J. Am. Chem. Soc.* **1995**, *117*, 3145–3155.
41. Porter, M. D.; Bright, T. B.; Allara, D. L.; Chidsey, C. E. D. *J. Am. Chem. Soc.* **1987**, *109*, 3559–3568.
42. Rodriguez, K. R.; Shah, S.; Williams, S. M.; Teeters-Kennedy, S.; Coe, J. V. *J. Chem. Phys.* **2004**, *121*, 8671–8675.
43. Hill, I. R.; Levin, I. W. *J. Phys. Chem.* **1979**, *70*, 842–851.
44. McPhail, R. A.; Snyder, R. G.; Strauss, H. L.; Ellinger, C. A. *J. Phys. Chem.* **1984**, *88*, 334–341.
45. Andrew, M. P.; Mattar, S. M.; Ozin, G. A. *J. Phys. Chem.* **1986**, *90*, 744–753.

46. Hayden, B. E. In *Vibrational Spectroscopy of Molecules on Surface*; Yates, J. T., Jr.; Modey, T. E., Eds.; Method of Surface Characterization · vol. 1; Plenum Press; New York, NY, 1987; Chapter 7.
47. Debe, M. K. *J. Appl. Phys.* **1984**, *55*, 3354–3366.
48. Parker, D. H.; Jones, M. E.; Koel, B. E. *Surf. Sci.* **1990**, *233*, 65–74.
49. Kislyuk, M. U.; Rozanov, V. V. *Kinet. Catal.* **1995**, *36*, 80–88.
50. King, D. A. *Surf. Sci.* **1975**, *47*, 384–402.
51. Miller, J. B.; Siddiqui, H. R.; Gates, S. M.; Russell, J. N., Jr.; Yates, J. T., Jr.; Tully, J. C.; Cardillo, M. J. *J. Chem. Phys.* **1987**, *87*, 6725–6732.
52. Rakov, V. S.; Denisov, E. V.; Laskin, J.; Futrell, J. H. *J. Phys. Chem. A* **2002**, *106*, 2781–2788.
53. Syomin, D.; Kim, J.; Koel, B. E.; Ellison, G. B. *J. Phys. Chem. B* **2001**, *105*, 8387–8394.
54. Hofmann, F.; Toennies, J. P. *Chem. Rev.* **1996**, *96*, 1307–1326.
55. Barth, J. V. *Surf. Sci. Rept.* **2000**, *40*, 75–149.
56. Vogt, A. D.; Beebe, T. P., Jr. *J. Phys. Chem. B* **1999**, 103, 8482–8489.
57. Nagaoka, S.; Okada, E.; Doi, S.; Mitsui, M.; Nakajima, A. *Eur. Phys. J. D* **2005**, *34*, 239–242.
58. Poirier, G. E.; Tarlov, M. J.; Rushmeier, H. E. *Langmuire* **1994**, *10*, 3383–3386.
59. Fenter, P.; Eberhardt, A.; Liang, K. S.; Eisenberger, P. *J. Chem. Phys.* **1997**, *106*, 1600–1608.
60. Lyon, J. T.; Andrews, L. *J. Phys. Chem. A* **2006**, *110*, 7806.
61. Philip, D.; Robinson, J. M. A. *J. Chem. Soc.*, *Perkin Trans.* **1988**, *2*, 1643.
62. Fujii, A.; Morita, S.; Miyazaki, M.; Ebata, T.; Mikami, N. *J. Phys.Chem. A* **2004**, *108*,

2652.

63. Morita, S; Fujii, A.; Mikami, N.; Tsuzuki, S. *J. Phys. Chem. A* **2006**, *110*, 10583.
64. Fogarty, D. P.; Kauts, N. A.; Kandel, S. A. *Surf. Sci.* **2007**, *601*, 2117.
65. Nuzzo, R.G.; Korenic, E. M.; Dubois, L. H., *J. Chem. Phys.* **1990**, *93*, 767.
66. Bensebaa, F.; Ellis, T. H.; Badia, A.; Lennox, R. B. *J. Vac. Sci. Technol. A* **1995**, *13*, 1331.
67. NIST Chemistry WebBook, NIST Standard Reference Database No. 69, June 2005; Linstrom, P. J.; Mallard, W. G., Eds.; National Institute of Standards and Technology; Gaithersburg, MD; (http://webbook.nist.gov).
68. Schaerer, A. A.; Busso, C. J.; Smith, A. E.; Skinner, L. B. *J. Am. Chem. Soc.* **1955**, *77*, 2017.
69. Sirota, E. B.; King, H. E., Jr.; Singer, D. M.; Shao, H. H. *J. Chem. Phys.* **1993**, *98*, 5809.
70. Sirota, E. B.; Singer, D. M. *J. Chem. Phys.* **1994**, *101*, 10873.
71. Rajabalee, F.; Negrier, P.; Mondieig, D. *Chem. Mater.* **2002**, *14*, 4081.
72. Hautman, J.; Klein, M. L. *J. Chem. Phys.* **1990**, *93*, 7483.
73. Mar, W.; Klein, M. L. *Langmuir* **1994**, *10*, 188.
74. Parikh, A. N.; Allara, D. L.; *J. Chem. Phys.* **1992**, *96*, 927.
75. Maroncelli, M.; Qi, S. P.; Strauss, H. L.; Snyder, R. G. *J. Am. Chem. Soc.* **1982**, *104*, 6237
76. Snyder, R. G.; Maroncelli, M.; Strauss, H. L.; Hallmark, V. M. *J. Phys. Chem.* **1986**, *90*, 5623.
77. Berger, R.; Gerber, C.; Gimzewski, J. K.; Meyer, E.; Güntherodt, H. J. *Appl. Phys. Lett.* **1996**, *69*, 40.

Table 3.1: Orientation angle (Θ, deg.) and adsorption heat (E_d, kJ/mol) of the V(benzene)$_2$ complexes soft-landed on each substrate.

Substrate	Θ	E_d
bare gold		64 ± 13
C_8H-SAM	69 ± 2	90 ± 19
C_{12}H-SAM	71 ± 1	110 ± 26
C_{16}H-SAM	73 ± 2	130 ± 10
C_{18}H-SAM	72 ± 1	138 ± 21
C_{22}H-SAM	78 ± 6	153 ± 27

Table 3.2. Vibrational mode assignments for M(benzene)$_2$ sandwich complexes supported on the C_{18}H-SAM substrate in 650–1550 cm^{-1} region

		complex		
mode[a]	symmetry	Ti(benzene)$_2$	V(benzene)$_2$	Cr(benzene)$_2$
$\nu_{o\text{-}p}$(CH)	A_{2u}	(700)	747 (742)	(796)
ν_r(CC)	A_{2u}	945 (947)	956 (956)	972 (972)
$\nu_{i\text{-}p}$(CH)	E_{1u}	977 (979)	988 (988)	996 (996)
ν(CC)	E_{1u}	1410	1418 (1419)	1429 (1429)

[a]Vibrational modes: $\nu_{o\text{-}p}$(CH), CH out-of-plane bending; ν_r(CC), ring breathing; $\nu_{i\text{-}p}$(CH), CH in-plane bending; ν(CC), in-plane CC ring stretching and deforming. Values in parentheses are corresponding frequencies in the condensed phase.

Table 3.3. Activation energy for desorption (E_d, kJ/mol) of M(benzene)$_2$ sandwich complexes supported on $C_{18}H$-SAM substrate

complex	E_d	deposition method
Cr(benzene)$_2$	71 ± 12	PVD
Cr(benzene)$_2$	130 ± 40	Soft-Landing
V(benzene)$_2$	138 ± 21	Soft-Landing
Ti(benzene)$_2$	125 ± 27	Soft-Landing

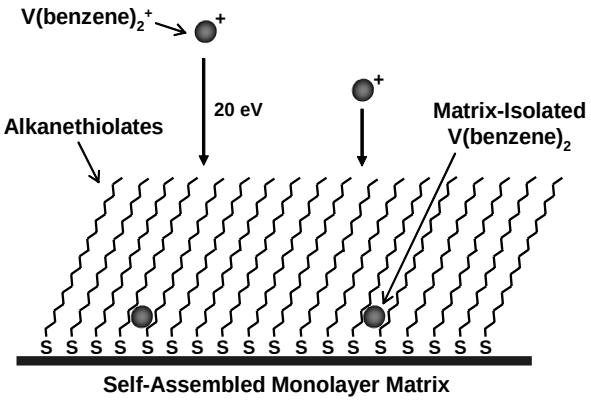

Figure 3.1. Schematic illustration of the soft-landing isolation of gas-phase synthesized $V(benzene)_2$ cations into an *n*-alkanethiol self-assembled monolayer (SAM) matrix where the alkyl chains are densely packed and tilted ~30° with respect to the surface normal. The incoming complex cations with high incident energy of 20 eV penetrate into the SAM matrix and are neutralized by charge transfer from the substrate. The structural disordering in the alkanethiolates induced by collisions with the complex ions and capturing of the penetrated complexes is not shown here.

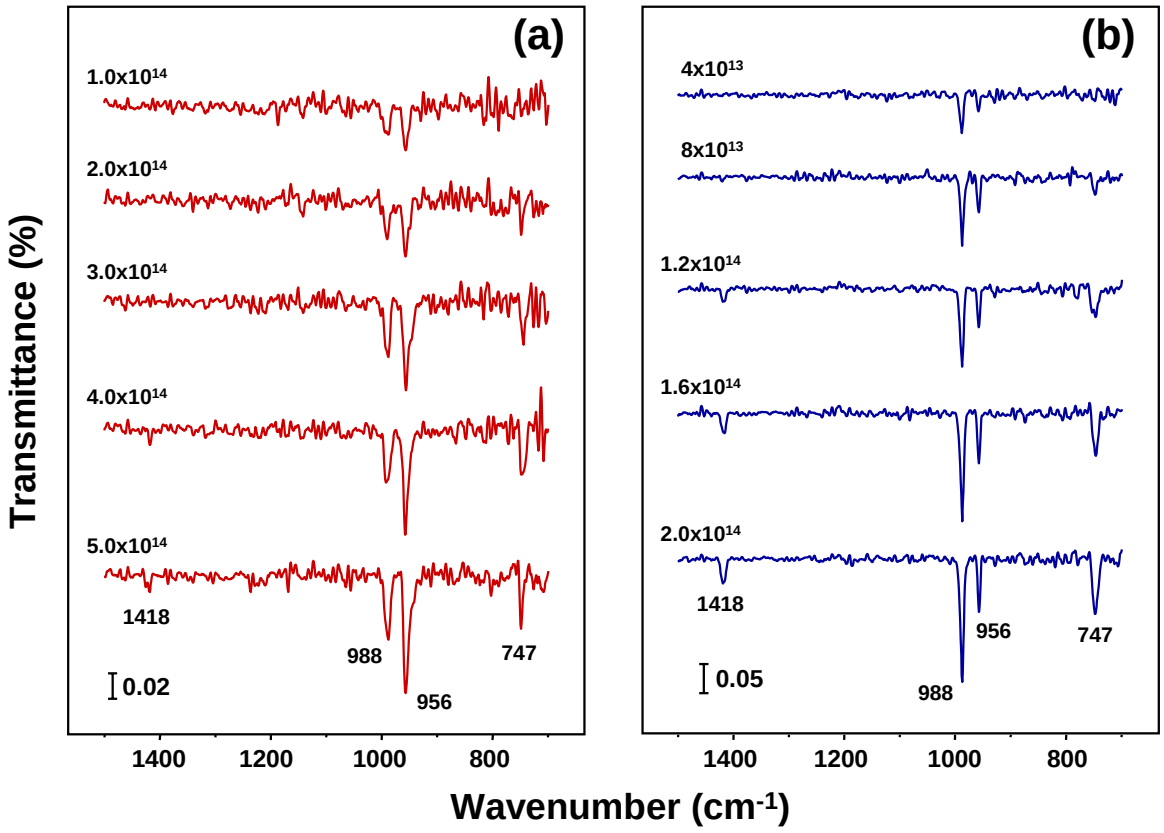

Figure 3.2. IRAS spectra in the 700–1500 cm^{-1} region for the V(benzene)$_2$ complexes at several deposition numbers on (a) gold and (b) C_{18}H-SAM at 180 K

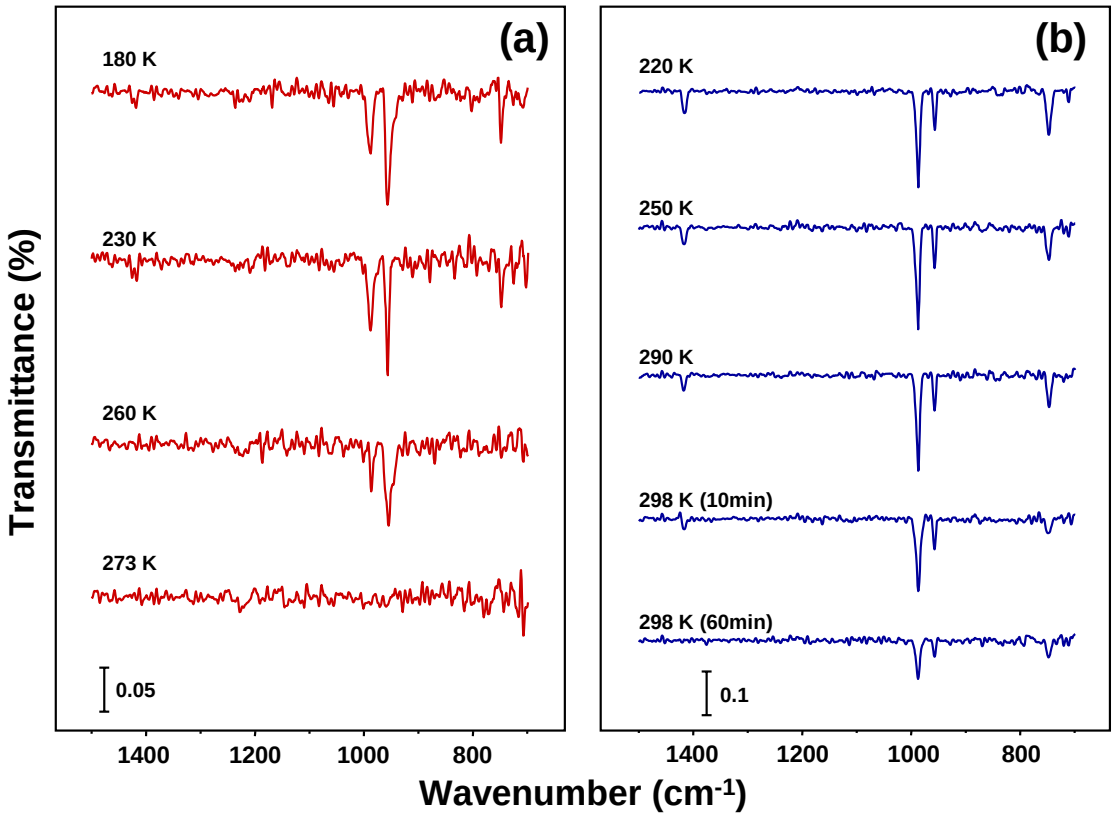

Figure 3.3. IRAS spectra showing the temperature-dependent variation of the $V(benzene)_2$ complexes after deposition of (a) 5.0×10^{14} ions onto gold and (b) 2.0×10^{14} ions onto $C_{18}H$-SAM at 180 K.

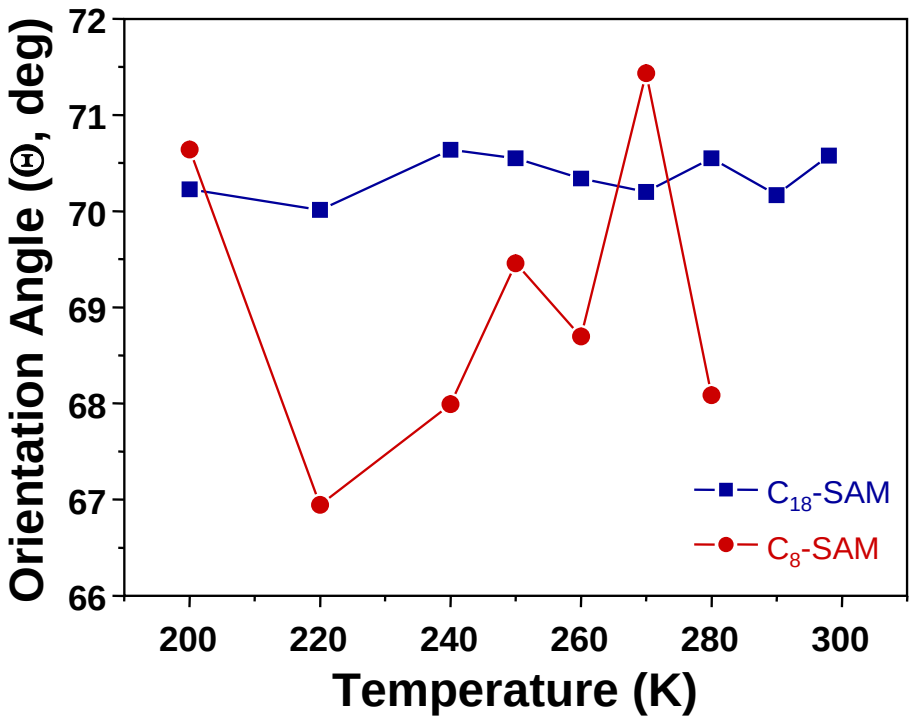

Figure 3.4. Temperature dependence of the average orientation angle of the $V(benzene)_2$ complexes soft-landed on (■) C_8H-SAM and (●) $C_{18}H$-SAM at 200 K.

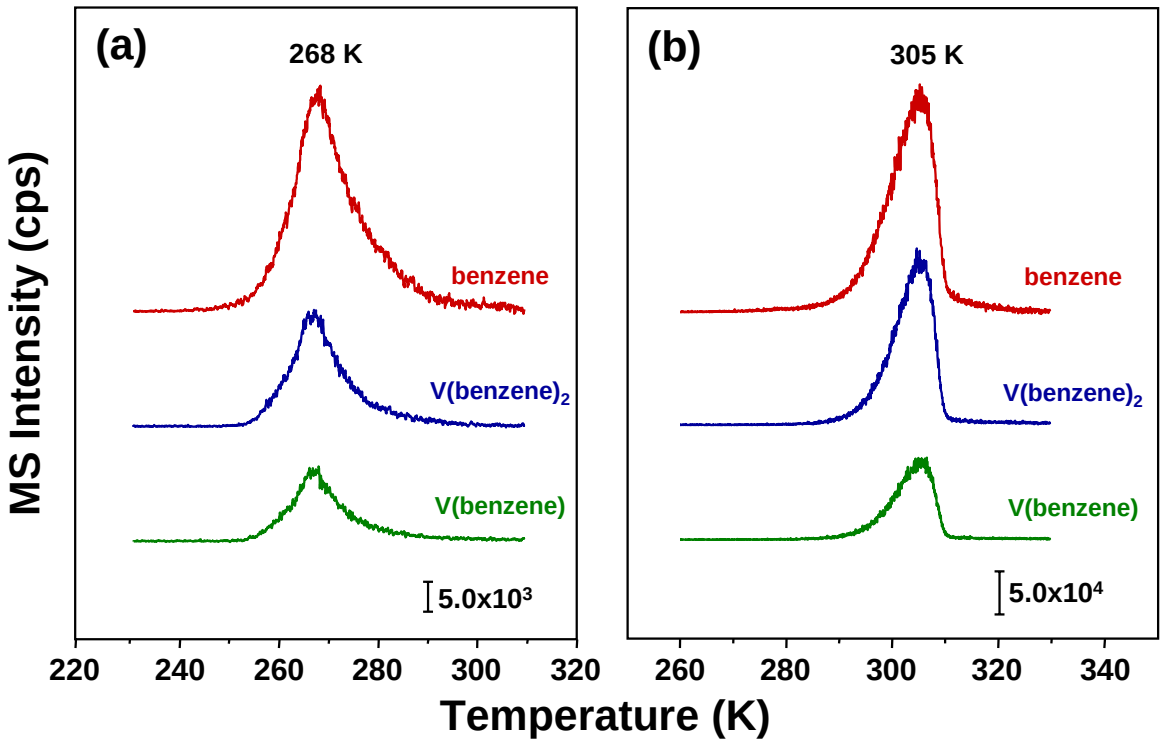

Figure 3.5. Multiplexed thermal desorption data for the $V(benzene)_2$ complexes soft-landed on (a) gold and (b) $C_{18}H$-SAM after deposition of 4×10^{13} complex ions at 180 K.

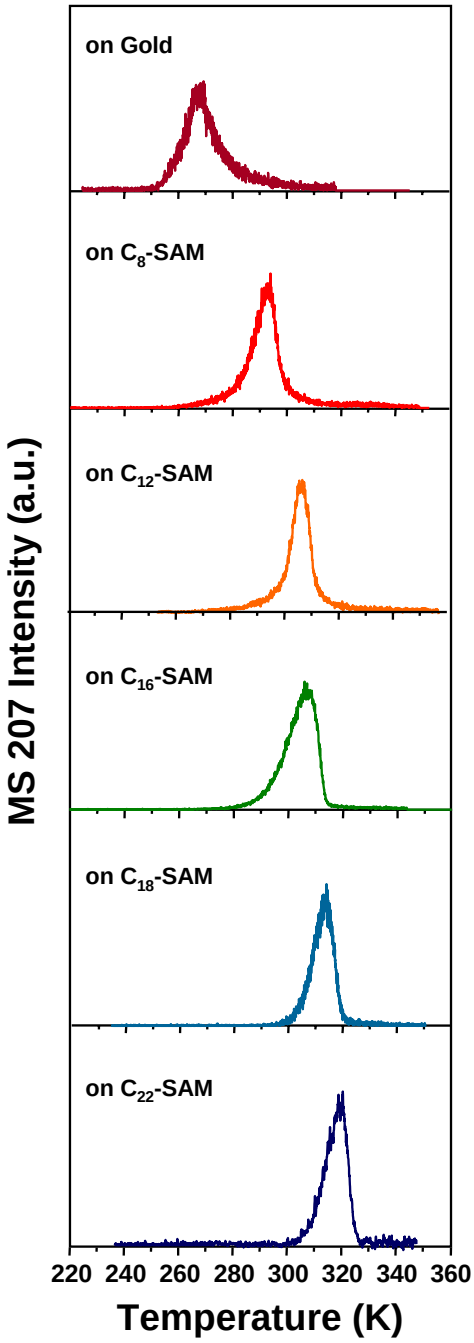

Figure 3.6. Thermal desorption spectra obtained for the V(benzene)$_2$ (m/z = 207) complexes soft-landed on the C_8H- to $C_{22}H$-SAMs, together with the gold substrate after deposition of 4×10^{13} complex ions at 180 K.

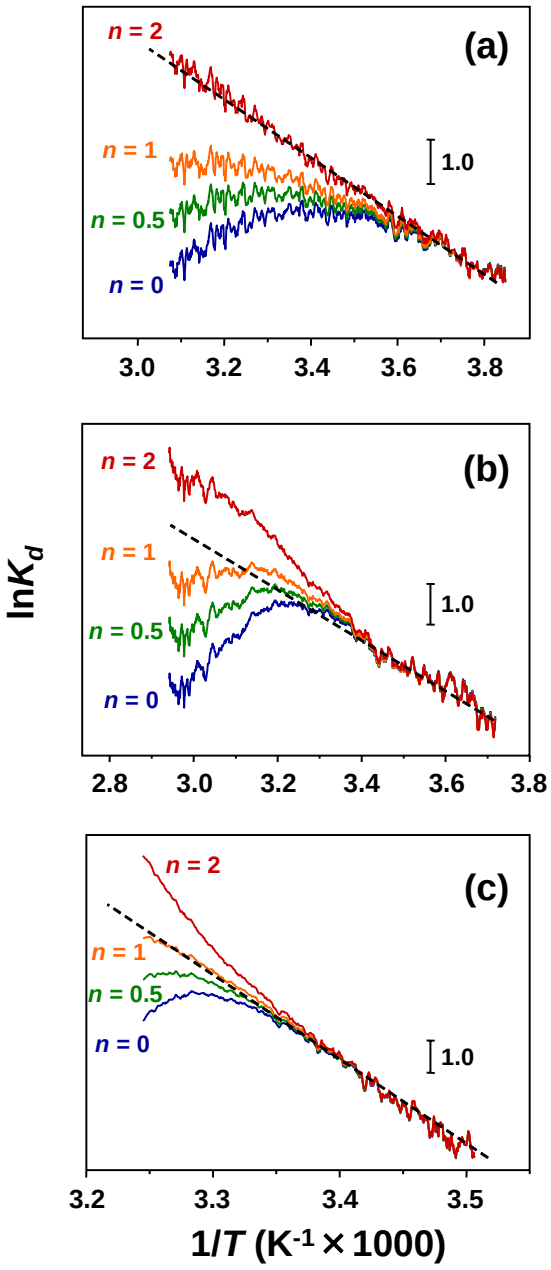

Figure 3.7. Arrhenius plots based on eq. (2) from the TDS spectra of the V(benzene)$_2$ complexes obtained for (a) gold surface, (b) C_8H-SAM, and (c) C_{18}H-SAM with reaction orders of n = 0, 0.5, 1, and 2. The reaction orders were obtained by the best linear fit (the dotted line) to the plot of n = 2 for the gold and n = 1 for C_{18}H-SAM, but a linear plot could not be obtained for the C_8H-SAM for all values of n.

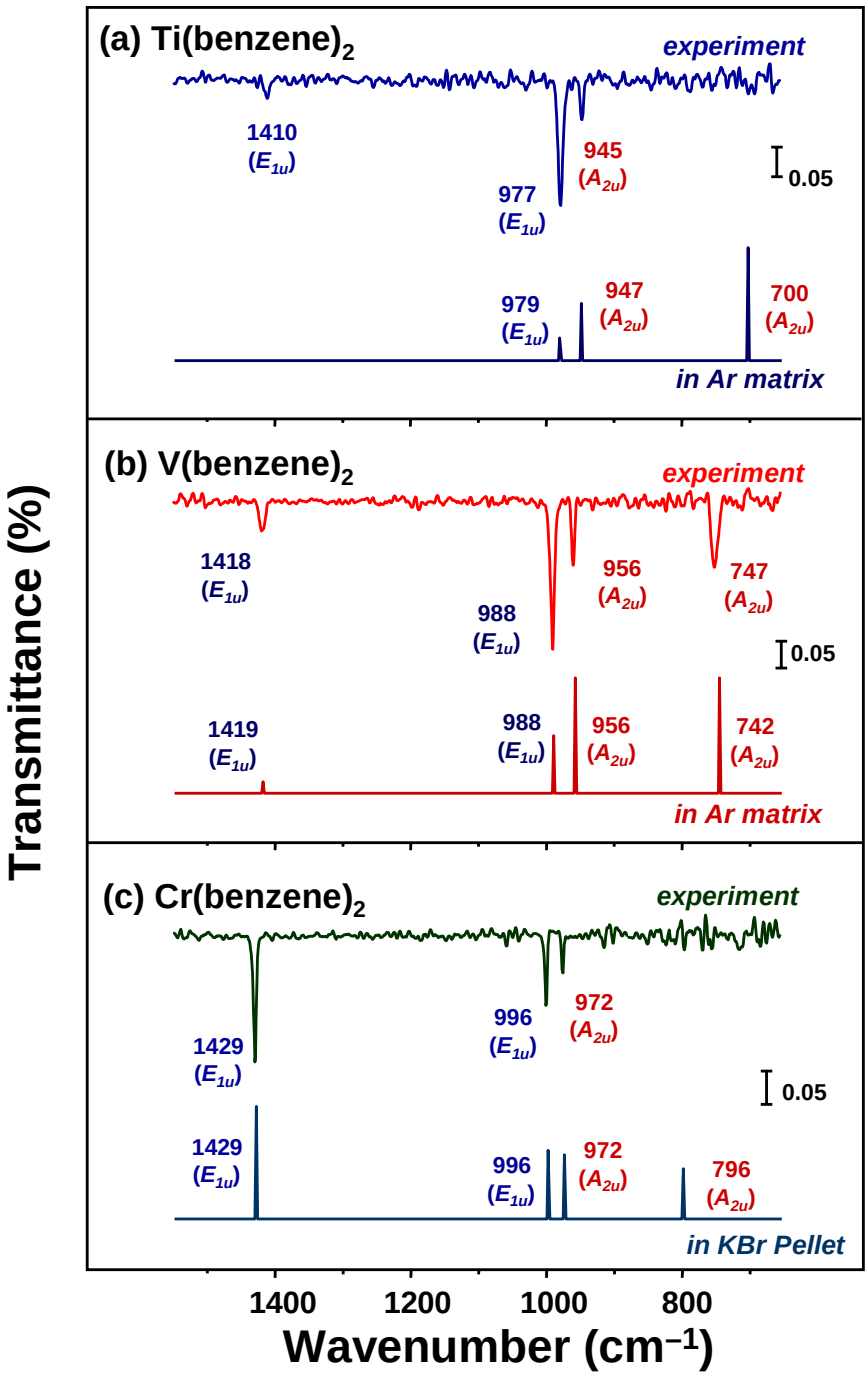

Figure 3.8. IRAS spectrum in the 650–1550 cm^{-1} region for (a) $Ti(benzene)_2$, (b) $V(benzene)_2$, and (c) $Cr(benzene)_2$ after soft-landing of 2.0×10^{14} complexes onto the $C_{18}H$-SAM substrate at 200 K, along with their IR fundamental in the condensed-phase.

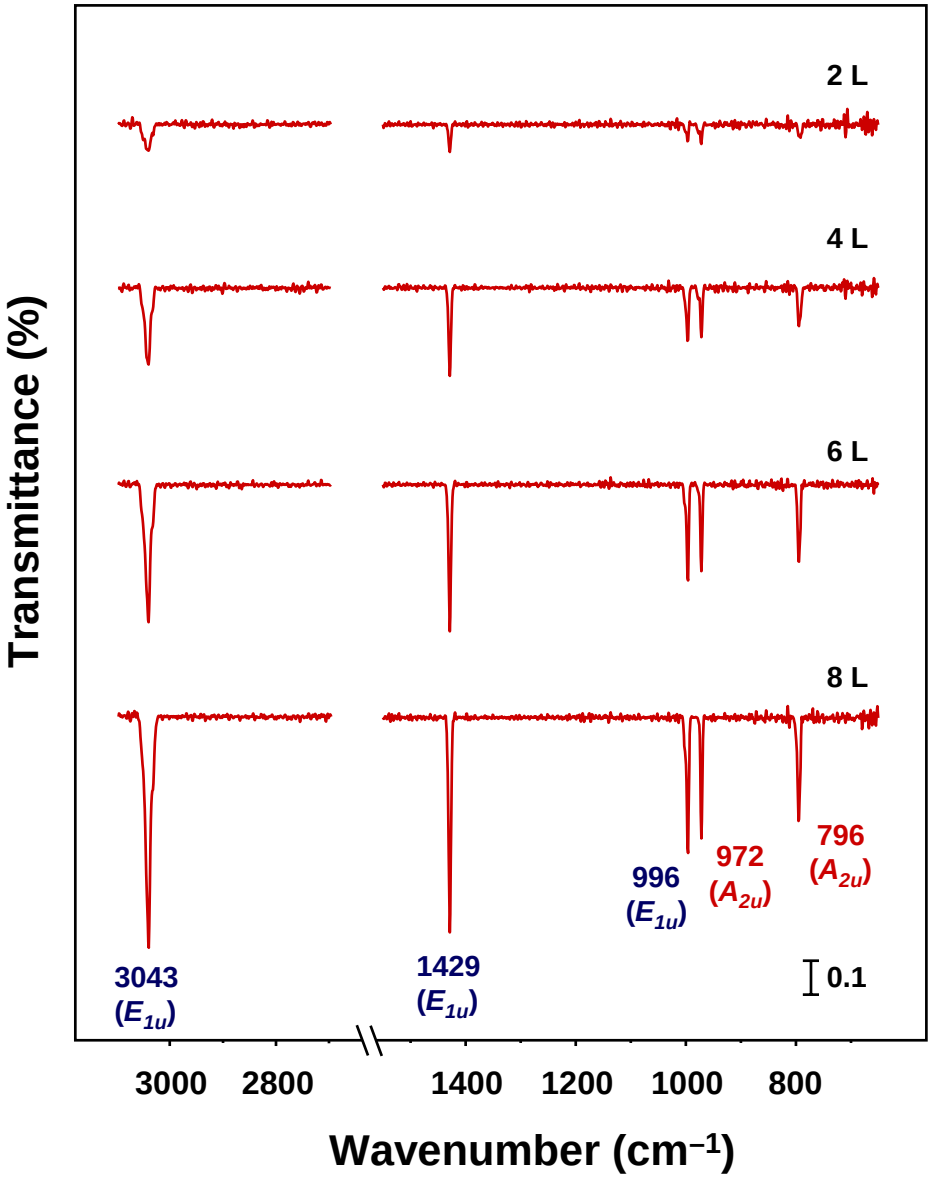

Figure 3.9. IRAS spectra in the 650–1550 and 2700–3100 cm^{-1} regions after the PVD of $Cr(benzene)_2$ complexes onto $C_{18}H$-SAM at several coverages.

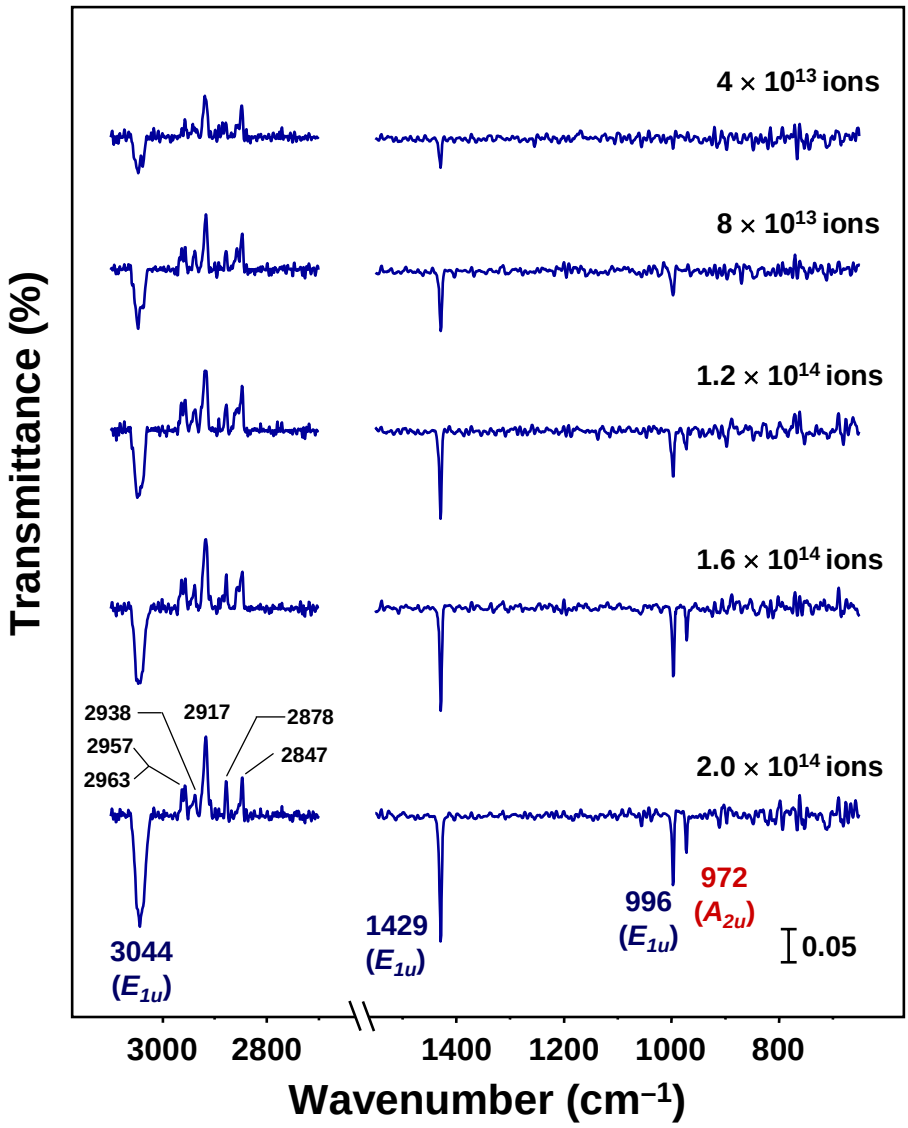

Figure 3.10. IRAS spectra in the 650–1550 and 2700–3100 cm^{-1} regions after the soft-landing of $Cr^{+}(benzene)_2$ complexes onto $C_{18}H$-SAM at several deposition numbers.

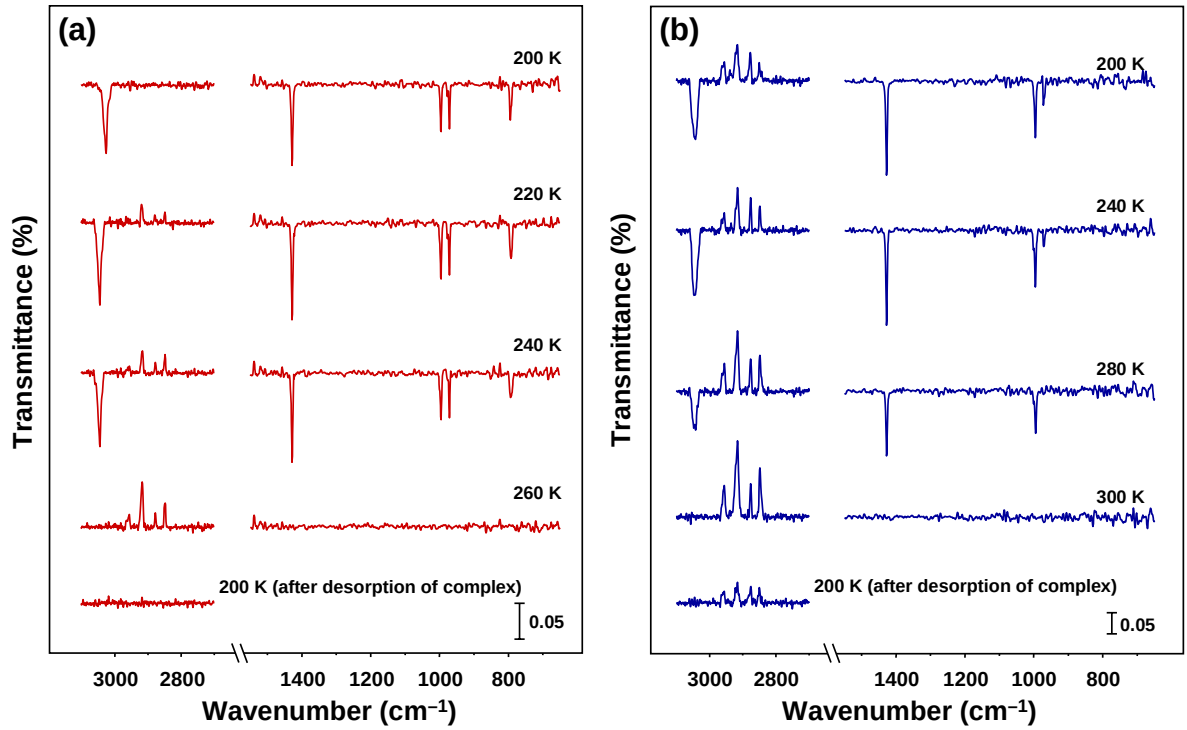

Figure 3.11. IRAS spectra showing the temperature-dependent variation of $Cr(benzene)_2/C_{18}H$-SAM after (a) the PVD of 8 L and (b) soft-landing of 2.0×10^{14} complexes.

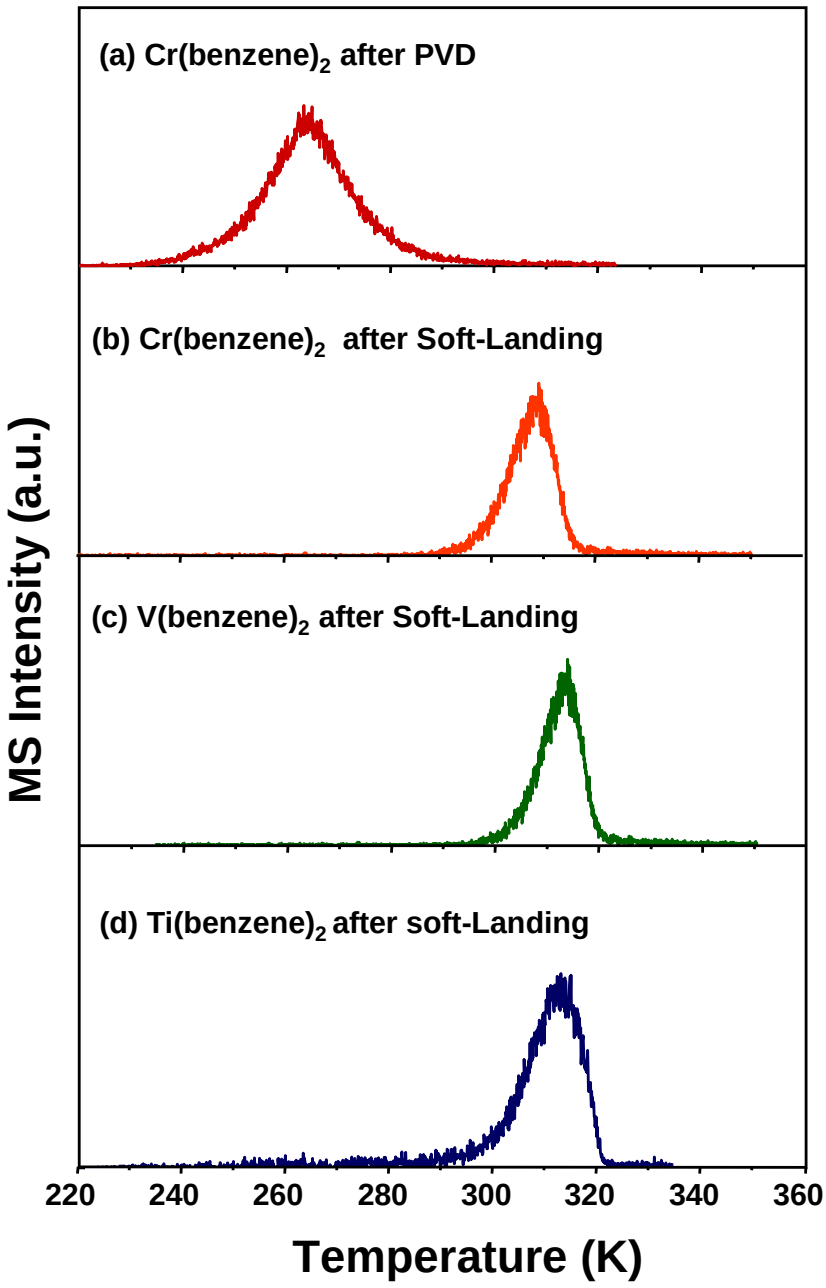

Figure 3.12. TDS spectra obtained for (a) $Cr(benzene)_2$ after the PVD of 1 L, (b) $Cr(benzene)_2$ after soft-landing of 4.0×10^{13} complexes, (c) $V(benzene)_2$ after soft-landing of 4.0×10^{13} complexes, and (d) $Ti(benzene)_2$ after soft-landing of 4.0×10^{13} complexes onto $C_{18}H$-SAM substrate at 200 K.

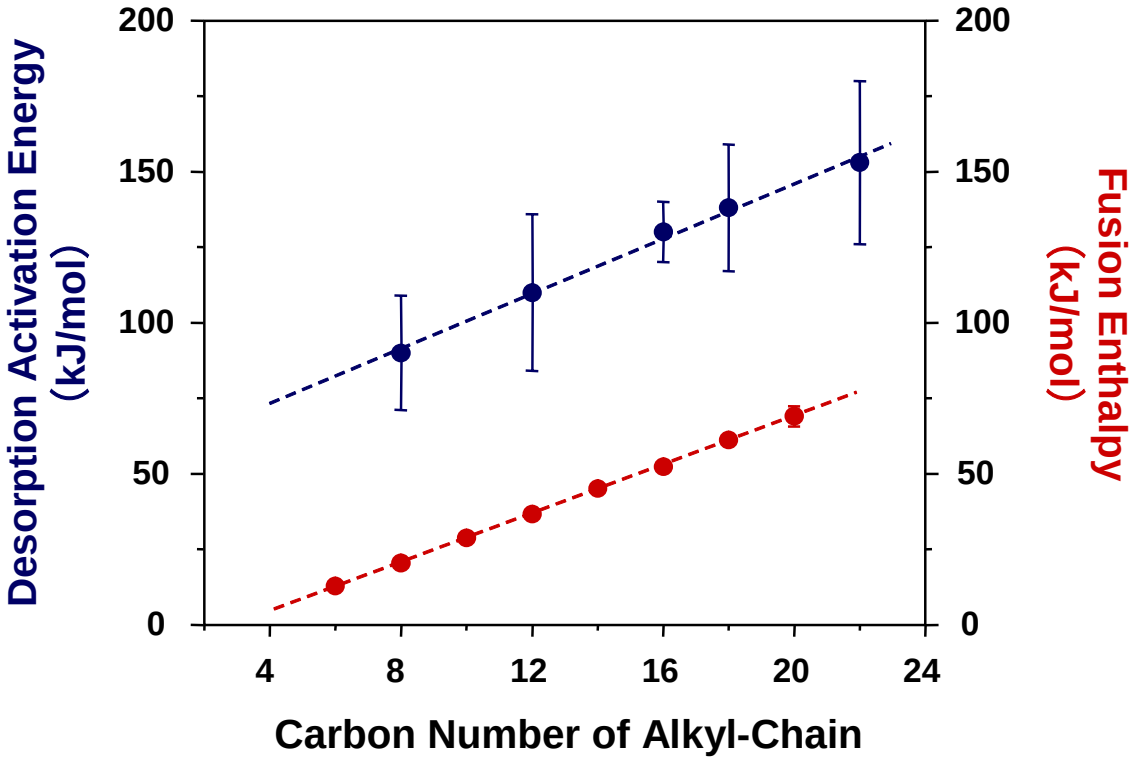

Figure 3.13. Activation energy for desorption of the V(benzene)$_2$ complexes soft-landed on the *n*-alkanethiol SAM matrices plotted against the chain length of the SAM (●), along with the fusion enthalpy of corresponding chain-length *n*-alkanes (○). The dashed line was provided by least-squares fitting of each data.

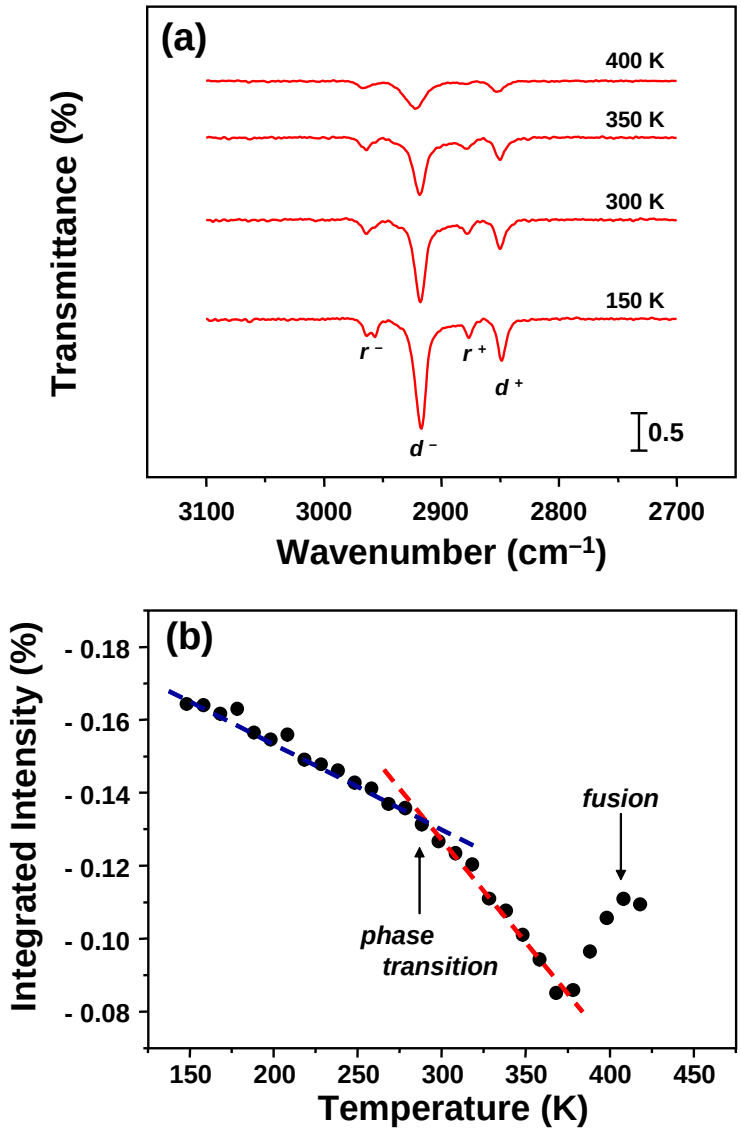

Figure 3.14. (a) IRAS spectra in the C–H stretching region of *n*-octadecanethiol on a gold surface at four representative temperatures. (b) Temperature dependence of the integrated intensity of the anti-symmetric (d^-) C–H stretching mode. The blue dashed-line represents the slope due to decrement in tilted angle of the alkyl-chains, and the slope of the red dashed-line is brought about by appearance of *gauch* conformational defects (rotator phase) in the SAM.

CHAPTER 4

The Effect of Fluorination of Organic Monolayer Matrices on Soft-Landing Isolation Regime

Abstract

Fluorination effect of the organic monolayers on the adsorption properties of the supported metal-benzene sandwich complex are investigated via soft-landed of $Cr(benzene)_2$ complexes onto a self-assembled monolayer of perfluoro-alkanethiol ($C_{10}F$-SAM). The adsorption state and thermal stability of the soft-landed complexes are studied with infrared reflection absorption spectroscopy (IRAS) and thermal desorption spectroscopy (TDS). The complexes are keeping their native sandwich structure intact even after soft-landing onto the $C_{10}F$-SAM matrix. As compared to the adsorption geometry in the alkanethiol SAMs, however, the orientational preference of the complexes is measurably changed to decrease the tilted angle on the $C_{10}F$-SAM substrate. The orientational change is probably caused by repulsive interaction between the π cloud of capping benzene rings of the complex and side-chain C-F groups of the fluorocarbon axes of the $C_{10}F$-SAM matrix. The thermal desorption study, moreover, provides a large desoption activation energy (~190 kJ/mol) for the complexes supported on the $C_{10}F$-SAM, as a result, the complexes can resist the thermal desorption until high-temperature region of ~320 K.

4.1. Introduction

Since the discovery of ferrocene in 1951,[1] complexes of metal atoms with aromatic molecules have been generated a special attraction in an old and well-established field of organometallic chemistry. In particular, transition-metal–benzene complexes have been studied extensively because these complexes can provide a basic model for understanding d–π binding interactions and also forming unique one-dimensional sandwich structure.[2–27] Using conventional chemical technique, among the first species of transition-metal (M)–dibenzene sandwich complexes, $M(benzene)_2$, to be synthesized was the $Cr(benzene)_2$ complex, reported in 1955.[2] Since that time, various kinds of $M(benzene)_2$ complexes have been produced and expansively studied for many years in the condensed phase.[3–9]

In gas-phase study, on the other hand, multiple-decker transition-metal–benzene complexes have been successfully synthesized by combining laser-vaporization technique with molecular beam methods.[10] The complexes of scandium (Sc), titanium (Ti), and vanadium (V) form a multiple-decker sandwich structure, where metal atoms and benzene molecules are alternatively stacked in a one-dimensional fashion. After the discovery of these multiple-decker complexes, $M_n(benzene)_{n+1}$, a wide variety of experimental and theoretical efforts have been devoted to their characterization.[11–27] For example, it has been recently demonstrated that $M_n(benzene)_{n+1}$ complexes possess unique size-dependent ferromagnetic properties originating from their one-dimensional structures. For $Sc_n(benzene)_{n+1}$ and $V_n(benzene)_{n+1}$ complexes, the magnetic moments increase monotonically with the cluster size,[23,24] and the ground electronic state of $Ti_2(benzene)_3$ complex has been reported as quintet.[25] Hence, it is anticipated that they become one of the most promising candidates for building blocks in nanoscale spintronic devices.

While $Cr(benzene)_2$ complex is uniquely stable in ambient condition due to the

18-electon rule,[2] the other transition-metal–benzene complexes are relatively reactive so that the low-temperature rare-gas matrix-isolation technique has been hitherto exploited to characterize these complexes.[3–7,38] In order to utilize such attractive sandwich complexes as building blocks in functional materials, however, the matrix-isolation over room temperature is highly desired. Use of a self-assembled monolayer (SAM) as a room-temperature isolation matrix is one of the effectual approach to support such reactive sandwich complexes on substrates. Cooks and co-workers have reported the trapping of polyatomic ions inside the SAM matrix by means of *soft-landing* technique,[28–30] where "soft-landing" is defined as intact deposition of gaseous species onto substrates at hyperthermal energies (<100 eV).[28,31] In our recent works, soft-landing of gas-phase synthesized vanadium–benzene cation complexes onto the SAMs of *n*-alkanethiols have been examined.[32,33,35] As a result, we have succeeded in matrix isolation of the neutralized vanadium–benzene complexes, i.e. supporting the complexes by the SAM matrices with their native sandwich structure intact, around room temperature, a result which suggests that the complexes are trapped inside the SAM matrices.

In order to increase the functionality of cluster-assembled surface, development of new techniques which is realizing a *fine-control* of adsorption regime, i.e., orientational preference and thermal stability of the clusters at surfaces. In this chapter, the author presents the effect of fluorination of organic monolayer matrices on soft-landing isolation regime of transition-metal–benzene complexes. Soft-landing of gas-phase synthesized $Cr(benzene)_2$ complexes onto a fluorinated SAM ($C_{10}F$-SAM) comprised of $CF_3(CF_2)_7(CH_2)_2SH$ was carried out at hyperthermal collision energy of 20 eV. The thermal deposition of the $Cr(benzene)_2$ vapor onto the $C_{10}F$-SAM is also performed via physical vapor deposition (PVD) technique. The resulting deposited complexes were investigated by the infrared reflection absorption spectroscopy (IRAS) and thermal desorption spectroscopy (TDS) to

evaluated the orientational preference and thermal stability of the complexes supported on the $C_{10}F$-SAM.

4.2. Experimental Section

Details of SAM preparation and experimental setup have been described Chapter 2. Briefly, a commercially available 10×10 mm^2 gold substrate, Au(100 nm thickness)/Ti/Silica (Auro Sheet, Tanaka Precious Metals Co. Ltd.), was immersed in a piranha solution (3:1 concentrated H_2SO_4:H_2O_2) for about 20 min to remove organic contaminants from the surface.[36,37] Dipping the gold substrate into a 0.5 mM ethanolic solution of heptadecafluoro-1-decanethiol (>99%, Aldrich) at ambient temperature for 20 h forms a $C_{10}F$-SAM on the surface. The formation of the $C_{10}F$-SAM/gold was confirmed by infrared reflection absorption spectroscopy (IRAS) and contact angle measurements (Drop Master 300, Kyowa Interface Science) of a water droplet (10 μl) at room temperature. The substrates were mounted on a sample holder capable of heating by a ceramic heater and cooling with liquid nitrogen reservoir.

Chromium (Cr)–benzene sandwich complexes are produced in a molecular beam by laser vaporization. Cation complexes are extracted by a quadrupole deflector and only the $Cr(benzene)_2$ complexes are size-selected by a quadrupole mass spectrometer (QMS), respectively. The cations are subsequently deposited onto the $C_{10}F$-SAM substrate, which is cooled to 220 K by a liquid nitrogen cryostat, with an incident energy of ~5–20 eV. Thermal deposition of $Cr(benzene)_2$ vapor onto the $C_{10}F$-SAM is also performed via admission of the sublimed complexes at 300 K to the chamber trough a standard leak valve. The exposures was recorded in Langmuires (1L = 10^{-6} Torr·s) and during the exposure time, the substrate temperature was kept at 180 K. The IRAS spectra for the deposited complexes are obtained

with IR incident angle of ~80° with respect to the surface normal. The TPD measurements are carried out with a heating rate of 1 K/s after the deposition of the complexes and the desorption species are detected by another QMS via electron impact ionization (~70 eV).

During the deposition of gas-phase synthesized $Cr(benzene)_2$ cation complexes onto the $C_{10}F$-SAM, we can measure ion current on the substrate caused by neutralization event of deposited complexes. It has been reported that fluorinated SAMs reduce neutralization of projectile ions in the deposition process and also trap the ions, in this study we have, however, measured similar ion current of ~12 nA for the deposition of $Cr(benzene)_2^+$ onto among the fluorinated SAM, alkanethiolate SAMs, and also a bare gold surface Thus, $Cr(benzene)_2^+$ will be efficiently neutralized after the deposition onto $C_{10}F$-SAM like the alkanethiolate SAM and gold surface.

4.3. Results

4.3.1. Infrared Spectroscopic Study

The IRAS spectra in 650–1550 cm^{-1} region of thermally deposited $Cr(benzene)_2$ complexes on the $C_{10}F$-SAM substrate at several coverage are shown in Figure 4.1. After exposure of 4 L, two absorption bands with E_{1u} symmetric vibrational modes at 996 and 1429 cm^{-1} start to appear, and additional band with A_{2u} symmetric mode appears at 972 cm^{-1} when the exposure reaches 8 L. The peak positions of these IR absorption bands are in good agreement with the IR fundamentals for the condensed-phase $Cr(benzene)_2$ complexes measured in a KBr pellet. Thus, the thermally deposited $Cr(benzene)_2$ complexes are molecularly adsorbed with keeping their native sandwich structure on the $C_{10}F$-SAM substrate. In the IRAS spectra, however, the relative intensity of the IR bands for the thermally deposited $Cr(benzene)_2$ complexes are rather different from that for the

condensed-phase complexes. For instance, the IR bands at 996 cm^{-1} (E_{1u} symmetric mode) is strongly observed as compared to that at 972 cm^{-1} (A_{2u} symmetric mode) for $Cr(benzene)_2$ supported on $C_{10}F$-SAM after the thermal deposition, while KBr-isolated $Cr(benzene)_2$ illustrates similar peak intensity between the two modes in the IR spectrum. Owing to the IRAS surface selection rule, the relative IR intensity of the A_{2u} and E_{1u} modes reflects the orientational preference of the ideally D_{6h}-symmetric $Cr(benzene)_2$ complexes on the substrate, and the predominant observation of E_{1u} modes implies that the $Cr(benzene)_2$ complex tilts its molecular axis far from the surface normal on the SAM substrate.

In addition, negative IR peaks are observed after the thermal deposotion of the complexes in Fig. 4.1. The peak positions of these negative peaks are assignable to vibrational frequencies for $CF_3(CF_2)_7(CH_2)_2SH$ molecules within the $C_{10}F$-SAM.[39,40] The assignment of vibrational modes for $CF_3(CF_2)_7(CH_2)_2SH$ molecules on a gold surface is indicated in Table 2.3 (in Chapter 2). The negative peaks at 667 and 693 cm^{-1} originating from CF_2 wagging and rocking modes, and the peaks at 1341 and 1378 cm^{-1} attributed to axial CF_2 stretching modes are predominantly observed. In this study, the background IR spectra were recorded before the depositions of complexes so that the appearance of negative peaks in measured IRAS spectra represent decrease in IR absorption intensity of the vibrational modes for $CF_3(CF_2)_7(CH_2)_2SH$ molecules due to the thermal deposition of the $Cr(benzene)_2$ complexes. Furthermore, it should be noted that the transition dipole moment of all the vibrational modes making the negative peaks taken after the thermal deposition are arise along the fluorocarobon helical axis.

Displayed in Figure 4.2 is the IRAS spectra for the $Cr(benzene)_2$ complexes soft-landed on the $C_{10}F$-SAM substrate at 220 K with hyperthermal collision energy of ~20 eV, as a function of the deposition-number of the $Cr(benzene)_2$ cations. As shown in Figure 4.2, two

absorption bands at 972 and 1429 cm^{-1} are first appeared until 1.0×10^{14} cations have been deposited onto the $C_{10}F$-SAM substrate. At the deposition number of 3.0×10^{14} ions, an additional mode is clearly observed at 996 cm^{-1}. The peak positions of these IR absorption bands are in good agreement with the IR fundamentals for the complexes in a KBr pellet. Although, it has been reported that fluorinated SAMs have the ability to trap the penetrated projectile ions *with retaining their charge* after the soft-landing,[28,29] the IRAS spectra obtained herein represent the IR signals originating only from neutral complexes. Thus, the results reveal that the soft-landed $Cr(benzene)_2$ cation complexes mostly lost their charge and the resulting *neutral* complexes adsorb on the $C_{10}F$-SAM substrate with their native sandwich structure intact. As compared to the IR spectrum for condensed-phase $Cr(benzene)_2$ in KBr pellet, furthermore, the IR peak at 972 cm^{-1} with A_{2u} symmetry is strongly observed with respect to that at 996 cm^{-1} with E_{1u} mode for the complexes soft-landed on the $C_{10}F$-SAM. Due to the IRAS selection rule, as mentioned above, the results suggest that appearance of orientaional preference of the $Cr(benzene)_2$ complexes soft-landed on the $C_{10}F$-SAM matrix. The preponderant observation of A_{2u} mode reflects that the $Cr(benzene)_2$ complexes tend to prefer the orientation with its molecular axis approximately perpendicular to the surface. The orientational preference of the complexes soft-landed on the $C_{10}F$-SAM is significantly changed from that of thermally deposited complexes.

As shown in Fig. 4.2, negative peaks were also appeared in the IRAS taken after soft-landing of $Cr(benzene)_2$ complexes onto the $C_{10}F$-SAM. However, the peak positions of the negative IR bands are different from that observed after the thermal deposition study. Prominently observed peaks at 1156 and 1252 cm^{-1} are assignable to CF_2 stretching, bending, and rocking modes and the peak at 1220 cm^{-1} is attributed to the modes comprising the bending and stretching of the carbon chain within $CF_3(CF_2)_7(CH_2)_2SH$ molecules forming the

$C_{10}F$-SAM, respectively. After the deposition of 3.0×10^{14} ions of Cr(benzene)$_2$ complexes, while the negative peaks originating from axial CF_2 stretching modes at 1339 and 1377 cm^{-1}, which are predominantly observed after the thermal deposition, were slightly appeared, only the vibrational modes with transition dipole moment perpendicular to the helical axis are pronouncedly observed in the IRAS spectrum after the soft-landing event.

4.3.2. Thermal Desorption Study

In order to evaluate the thermal stability of thermally deposited and soft-landed Cr(benzene)$_2$ complexes on the $C_{10}F$-SAM substrate, temperature-induced variations of the IRAS spectra was examined, as shown in Figure 4.3. The upper traces in Figs. 4.3(a) and (b) represent the IR spectra of the Cr(benzene)$_2$ complexes on the $C_{10}F$-SAM substrates taken after thermal deposition of 8 L and soft-landing of 3.0×10^{14} cations with hyperthermal collision energy of ~20 eV, respectively. In the case of the thermally deposited complex, the IR intensity reduction begins to occur around 240 K, and the bands are completely vanished at 270 K. These IR bands never return to their initial intensity, even if the substrate is cooled down again to the initial surface temperature of 220 K so that decrease in IR intensity reflects thermal desorption of the adsorbed complexes from the SAM substrates. For the soft-landed complexes, in contrast, all the IR peaks in the spectra start to decrease at a much higher temperature of 320 K and completely vanished at 330 K. Namely, the desorption temperature of the soft-landed Cr(benzene)$_2$ complex is approximately 60 K higher than that of thermally deposited complex on the $C_{10}F$-SAM substrate.

With increase in the surface temperature, we can find growth of negative peaks originating from the vibrations of fluorocarbon chains within the $C_{10}F$-SAM in the IRAS spectra. The growth of the negative peaks in this instance reflects the decrease in the absorption intensity of the vibration signal due to the change in the tilt angle and/or

appearance of conformational disordering of the molecular chains within the SAM matrices with the surface temperature.

The thermal desorption kinetics of the $Cr(benzene)_2$ complexes supported on the $C_{10}F$-SAM substrates was evaluated by the TDS study in detail. Figure 4.4 (a) and (b) show the TDS spectra for $Cr(benzene)_2$ complexes on the $C_{10}F$-SAM substrates taken after thermal deposition of 2 L and soft-landing of 1.0×10^{14} cations, respectively. In order to reduce the aggregations and interactions between the adsorbed complexes themselves on the substrate, in this TDS measurement, the deposition number of the landed complexes was set to provide a relatively low coverage.

In the case of the thermally deposited complex, as shown in Fig. 4.4 (a) the thermal desorption of the supported complexes starts ~210 K and the desorption rate reaches maximum at ~240 K. The TDS curve displays a nearly symmetric shape in which the ion intensity slowly decreases after the peak maximum to have a tail on their high-temperature side. The identical feature was also observed in the TDS spectra of physisorbed $M(benzenen)_2$ complexes on a gold surface and methyl-surface of the C_nH-SAM matrices, thermally deposited $Cr(benzene)_2$ complexes would be thus physisorbed on the surface of the $C_{10}F$-SAM. In addition, the illustration of tailing in the high-temperatures in the TDS spectrum can be brought about by a surface diffusion of the complexes on the SAM surface.

For the soft-landed complexes, however, the TDS spectral feature is pronouncedly difference from that for thermally deposited complexes. The thermal desorption of the complexes soft-landed on the $C_{10}F$-SAM starts much higher temperature of ~320 K, and the desorption rate reaches maximum at ~350 K. The drastic increase in the desorption temperature indicates that the soft-landed $Cr(benzene)_2$ complexes are more strongly bounded on the SAM substrate relative to the thermally deposited complexes. In addition, the TPD

curves for the soft-landed complexes illustrate asymmetric peak profiles in which the desorption rate rapidly decrease after the peak maximum. This result demonstrates that the soft-landed complexes desorb from the $C_{10}F$-SAM substrate via a first order desorption kinetics: namely, the thermal diffusions of the complexes in the desorption process are effectually inhibited. The increase in the desorption temperature and first order desorption kinetics obtained herein most likely suggest the incorporation of the M(benzene)$_2$ complexes inside the SAM matrix (i.e. matrix-isolation regime) after their soft-landing due to the hyperthermal collision event. As a consequence, the Cr(benzene)$_2$ complexes trapped firmly by fluorocarbon chains inside the $C_{10}F$-SAM matrix acquires unusual high thermal stability.

The activation energy for desorption of the complexes supported by the SAM substrates can be quantitatively determined by taking Arrhenius plots of the measured TDS spectra. For the Cr(benzene)$_2$ complexes thermally deposited on the $C_{10}F$-SAM substrate after the PVD, the desorption activation energy was calculated to be 68 ± 18 kJ/mol. This value is comparable to the desorption activation energy for other M(benzene)$_2$ complexes physisorbed on a gold surface and methyl-surface of C_nH-SAM matrices. In contrast, the Cr(benzene)$_2$ complexes soft-landed on the $C_{10}F$-SAM matrix obtain much larger desorption activation energy of 195 ± 31 kJ/mol. This considerable enhancement of the desorption activation energy clearly demonstrates that the Cr(benzene)$_2$ complexes are not physisorbed on the surface but it supports the existence of complexes inside the $C_{10}F$-SAM matrix after the soft-landing.

4.4. Discussion

Hyperthermal collision of the incoming Cr(benzene)$_2$ complexes with the $C_{10}F$-SAM surface would result in penetration of the complexes into the SAM matrix, while the

thermally deposited Cr(benzene)$_2$ complexes certainly adsorbed on the surface of the C_{10}F-SAM matrix. Indeed, penetration of landed complexes into the SAM matrices during hyperthermal collision event is also demonstrated for soft-landing onto the C_nH-SAM substrates. Drastic increment in thermal stability of the soft-landed complexes indicates that the penetrated complexes are firmly trapped inside the C_{10}F-SAM matrix.

Both the thermally deposited and soft-landed complexes exhibit orientational preference on the C_{10}F-SAM substrates. The orientational preference of the sandwich complex inside the SAM matrix is probably due to a weak chemical interaction between the complex and organo-chains forming the SAM matrix. In the case of the complexes isolated in the C_nH-SAM, indeed, attractive CH-π interaction between the capping benzene rings of the complex and the hydrogen atoms of methylene groups of the surrounding alkyl chains would make an orientation of the complex inside the SAM matrix, where the complex greatly tilts its molecular axis to the surface plane. The complexes isolated in the C_{10}F-SAM matrix, however, favor different orientational geometry, which the complexes cant its molecular axis approximately perpendicular to the surface. This orientational geometry would result from repulsive interaction between the capping benzene rings of the complex and the fluorine atoms of side-chain CF_2 groups of fluorocarbon molecules. Due to the high electro-negativity of a fluorine atom, the electric charge of C–F bonding mostly distributed on the fluorine side. Hence, electrostatic repulsion between highly-charged fluorine atom with π-electronic clouds of benzene rings would give rise to the orientational preference of the complex inside C_{10}F-SAM matrix, which is different from that inside the C_nH-SAM matrix.

Such electrostatic repulsion between the benzene π rings and C–F is also suggested by the IRAS measurement of thermally deposited Cr(benzene)$_2$ on the C_{10}F-SAM. When the M(benzene)$_2$ complexes adsorb on the methyl-surface via their thermal deposition onto

C_nH-SAM matrix, the complexes are randomly oriented on the surface. However, the IRAS spectra obtained herein represent that the $Cr(benzene)_2$ complexes are adsorbed on the CF_3-terminated surface with their benzene planes approximately perpendicular to the surface after their thermal deposition onto $C_{10}F$-SAM matrix. Because of the electrostatic repulsion between the π rings and C–F group, the orientational preference of the complexes may be occurred even on the surface of $C_{10}F$-SAM matrix.

The IRAS measurement obtains negative peaks originating from vibrational modes of fluorocarbon chains within the $C_{10}F$-SAM matrix after the depositions of the complexes; however, positions of the negative IR peaks are depending on the deposition energy, i.e. adsorption regime, of the complexes to the SAM surface. Only the vibrational modes whose transition dipole moment is arise along the fluorocarobon helical axis makes negative peaks after the thermal deposition, while the soft-landing with hyperthermal collision energy predominantly provides negative peaks attributed to vibrational modes with transition dipole moment perpendicular to the helical axis. This selective decrement in IR intensity for the vibrations of the $C_{10}F$-SAM may result from induced dipole field due to adsorption or penetration of the complexes on/in the SAM matrices. Indeed, such induced dipole field usually affects IR absorption intensity of vibrational modes.[39–42]

Although, a fluorocarbon chain and benzene monomer has few or no dipole moment, respectively, their complex induces dipole moment between from the benzene to fluorocarbon chain. As shown in Figure 4.5, induced dipole moment in fluorocarbon–benzene complex with different two conformations is calculated by Gaussian 03 program[43] in order to roughly evaluate the induced dipole field in the system for $Cr(benzene)_2$ complexes supported on the $C_{10}F$-SAM. Density functional theory (DFT) was used with B3LYP functional and 6-31G(d) basis set was employed for each atom in the complex. Displayed in Fig. 4.5 (a) is a model

complex where a benzene monomer attaches to terminal CF_3 group of a fluorocarbon chain with benzene plane parallel to the chain axis, simply representing the adsorption system of $Cr(benzene)_2$ complexes on the surface of the $C_{10}F$-SAM. In this model, the induced dipole moment of 0.1897 Debye arises along the molecular axis of the fluorocarbon chain. On the other hand, another model complex shown in Fig. 4.5 (b) where a benzene monomer adheres to the side CH_2 groups of a fluorocarbon chain with benzene plane perpendicular to the chain axis, the conformation which is formally representing the system of matrix-isolation of $Cr(benzene)_2$ complexes inside the $C_{10}F$-SAM. In this model complex, the induced dipole moment of 0.4072 Debye arises perpendicular to the molecular axis of the fluorocarbon chain. Thus, when the $Cr(benzene)_2$ complexes are adsorbed on the $C_{10}F$-SAM after the thermal deposition, the induced dipole filed most likely affects only the vibrational modes with transition dipole parallel to the fluorocarbon axis to make negative peaks in the IRAS spectrum. In contrast, incorporation of $Cr(benzene)_2$ into the $C_{10}F$-SAM matrix after soft-landing produces dipole field perpendicular to the fluorocarbon axis so that only the vibrational modes whose transition dipole perpendicular to the axis would be influenced. Since IR absorption intensity for vibrations of highly polarized C–F group is particularly large enough with respect to other functional groups in organic compounds (e.g. about ten times lager than C–H group), the effect of induced dipole field on the IR absorption intensity can be successfully detected under the system of $Cr(benzene)_2$ deposition onto the $C_{10}F$-SAM substrate.

Thermal desorption study disclosed the unusual large desorption activation energy for the complexes trapped inside the $C_{10}F$-SAM matrix after the soft-landing. Interestingly enough, this value is about 60 kJ/mol larger than the desorption activation energy of $M(benzene)_2$ complexes isolated inside the $C_{18}H$-SAM matrix. There are two plausible

reasons to explain the pronounced increase in desorption temperature as well as desorption activation energy of the sandwich complexes by fluorination of the supporting organic monolayer matrices. The first explanation is that the isolated complexes are stabilized due to attractive quadrupole–quadrupole interaction between the capping benzene rings of the complex and side-chain CF groups of the fluorocarbon chains inside the C_{10}F-SAM matrix. As mentioned above, both the benzene ring and fluorocarbon chain possess imperceptible electric dipole moments, however, they will be highly polarized in quadrupole electric field. Thus, the attractive quadrupole–quadrupole interaction may induce the stabilization of the $Cr(benzene)_2$ complexes in the C_{10}F-SAM matrix. The other origin is enhancement of the enthalpy at phase transition of the monolayer matrix. As mentioned in Chapter 3, the thermal desorption of the matrix-isolated complexes would be associated with the crystal-rotator phase transition of the monolayer matrices, and the enthalpy at the crystal-rotator phase transition may involve in increasing the desorption activation energy of the complexes in the SAM matrices.

In contrast to the flexible *n*-alkyl chain, the fluorocarbon axis is intramolecularly stabilized, i.e. possesses large intramolecular rotational barrier to make a conformational rigidity.[44,45] The appearance of the rotator phase is brought about by the rotational excitation of molecular chains in the monolayer matrix; so that the enthalpy at the phase transition of the C_{10}F-SAM matrix formed by intramolecularly stabilized fluorocarbon axis would be larger than that of C_nH-SAM matrices consisting of flexible alkyl-chains. Indeed, I evaluate the temperature for the crystal-rotator phase transition of the C_{10}F-SAM by plotting the IR intensity for CF_2 stretching at 1156 cm^{-1} versus surface temperature as shown in Figure 4.6. The slope of the intensity decrease drastically changed at around 320 K may due to the crystal-rotator phase transition, and the value is about 30 K higher than temperature of the

crystal-rotator phase transition for the $C_{18}H$-SAM and also well accorded with the desorption temperature of the complexes trapped in the $C_{10}F$-SAM matrix. The results strongly suggest that the crystal-rotator phase transition most likely assist the release of embedded complexes from the SAM matrix and increscent in enthalpy at the crystal-rotator phase transition of organic monolayer matrix causes the increase in the desorption activation energy of the matrix-isolated complexes

4.5. Conclusion

In order to investigate the effect of fluorination of organic monolayer matrices, gas-phase synthesized chromium–benzene 1:2 cation complexes, $Cr^{+}(benzene)_2$ were size-selectively deposited onto the $C_{10}F$-SAM matrix with the hyperthermal collision energy of 20 eV. The complexes were neutralized even on the fluorinated SAM matrix, and retain their native sandwich structure intact. The hyperthermal collision event in the soft-landing process results in penetration of incoming complexes into the SAM matrix, while the extremely low energy (thermal) deposition (~25 meV) of $Cr(benzene)_2$ complexes via PVD technique poses physisorption of the complexes on a top of the SAM. Although the complexes are weakly physisorbed on the $C_{10}F$-SAM with their molecular axis largely canted to the surface plane, the complexes embedded in the $C_{10}F$-SAM matrix are oriented with their molecular axis approximately perpendicular to the surface. Such orientational preferences is probably due to the repulsive interaction between the π cloud of capping benzene rings of the complex and the outmost CF_3 group and side-chain C-F groups of the fluorocarbon axes of the $C_{10}F$-SAM matrix, respectively. In addition, the complexes penetrating into the SAM matrix exhibits unusual large activation energy for desorption of over 190 kJ/mol, with the result that the thermal desorption of the complexes can be suppressed over room temperature. It can be

conclude that the orientational preference as well as thermal stability can be control well by modification of organothiolates forming the SAM matrices.

References

1. Kealy, T. J.; Pauson. P. L. *Nature* **1951**, *168*, 1039.

2. Fisher, E. O.; Hafner, W. Z. *Naturforsch* **1955**, 10B, 665.

3. Andrews, M. P.; Huber, H. X.; Mattar, S. M.; McIntosh, D. F.;Ozin, G. A. *J. Am. Chem. Soc.* **1983**, *105*, 6170.

4. Andrew, M. P.; Mattar, S. M.; Ozin, G. A. *J. Phys. Chem.* **1986**, *90*, 744.

5. Mattar, S. M.; Sammynaiken, R. *J. Chem. Phys.* **1997**, *106*, 1080.

6. Lyon, J. T.; Andrews, L. *J. Phys. Chem. A* **2005**, *109*, 431.

7. Lyon, J. T.; Andrews, L. *J. Phys. Chem. A* **2006**, *110*, 7806.

8. Cirelli, G.; Russu, A.; Wolf, R.; Rudin, M.; Schweiger, A.;Gunthard, Hs. H. *Chem. Phys. Lett.* **1982**, *92*, 223.

9. McCamley, A.; Perutz, R. N. *J. Phys. Chem.* **1991**, *95*, 2738.

10. Hoshino, K.; Kurikawa, T.; Takeda, H.; Nakajima, A.; Kaya, K. *J. Phys. Chem.* **1995**, *99*, 3035.

11. Nakajima, A.; Kaya, K. *J. Phys. Chem. A* **2000**, *104*, 176.

12. Jena, P.; Castleman, A. W., Jr. *Proc. Natl. Acad. Sci. USA* **2006**, *103*, 10560.

13. Weis, P.; Kemper, P. R.; Bowers, M. T.; *J. Phys. Chem. A* **1997**, *101*, 8207.

14. van Heijnsbergen, D.; von Helden, G.; Meijer, G.; Maitre, P.; Duncan, M. A. *J. Am. Chem. Soc.* **2002**, *124*, 1562.

15. Jaeger, T. D.; van Heijnsbergen, D.; Klippenstein, S. J.; von Helden, G.; Meijer, G.; Duncan, M. A. *J. Am. Chem. Soc.* **2004**, *126*, 10981.

16. Jaeger, T. D.; Pillai, E. D.; Duncan, M. A. *J. Phys. Chem. A* **2004**, *108*, 6605.

17. Pendy, R.; Rao, B. K.; Jena, P.; Blanco, M. A. *J. Am. Chem. Soc.* **2001**, *123*, 3799.

18. Kandalam, A.K.; Rao, B. K.; Jena, P.; Pandey, R. *J. Chem. Phys.* **2004**, *120*, 10414.

19. Wedderburn, K. M.; Bililign, S.; Levy, M.; Gdanitz, R. *J. Chem. Phys.* **2006**, *326*, 600.

20. Yasuike, T.; Yabushita, S. *J. Phys. Chem. A* **1999**, *103*, 4533.

21. Wang, J.; Jellinek, J. *J. Phys. Chem. A* **2005**, *109*, 10180.

22. Wang, J.; Acioli, P. H.; Jellinek, J. *J. Am. Chem. Soc.* **2005**, *127*, 2812.

23. Miyajima, K.; Nakajima. A.; Yabushita, S.; Knickelbein, M. B.; Kaya, K. *J. Am. Chem. Soc.* **2004**, *126*, 13202.

24. Miyajima, K.; Yabushita, S.; Knickelbein, M. B.; Nakajima. A. *J. Am. Chem. Soc.* **2007,** *129*, 8473.

25. Kua, J.; Tomlin, K. M. *J. Phys. Chem. A* **2006**, *110*, 11988.

26. Xiang, H.; Yang, J.; Hou, J. G.; Zhu, Q. *J. Am. Chem. Soc.* **2006**, *128*, 2310.

27. Maslyuk, V. V.; Bagrets, A.; Meded, V.; Arnold, A.; Evers, F.; Brandbyge, M.; Bredow, T.; Mertig, I. *Phys. Rev. Lett.* **2006**, *97*, 097201.

28. Miller, S. A.; Luo, H.; Pachuta, S. J.; Cooks, R. G. *Science* **1997**, *275*, 1447.

29. Luo, H; Miller, S. A.; Cooks, R. G.; Pachuta, S. J. *Int. J. Mass Spectrom. Ion Processes* **1998**, *174*, 193.

30. Gologan, B; Green, J. R.; Alvarez, J.; Laskin, J.; Cooks, R. G. *Phys. Chem. Chem. Phys.* **2005**, *7*, 1490.

31. Heiz, U.; Vanolli, F.; Trento, L.; Schneider, W. D. *Rev. Sci. Instrum.* **1997**, *68*, 1986.

32. Nagaoka, S.; Okada, E.; Doi, S.; Mitsui, M.; Nakajima, A. *Eur. Phys. J. D* **2005**, *34*, 239.

33. Mitsui, M.; Nagaoka, S.; Matsumoto, T.; Nakajima, A. *J. Phys. Chem. B* **2006**, *110*, 2968.

34. Nagaoka, S.; Matsumoto, T; Okada, E.; Mitsui, M.; Nakajima, A. *J. Phys. Chem. B* **2006**, *110*, 16008.

35. Nagaoka, S.; Matsumoto, T; Ikemoto, K.; Mitsui, M.; Nakajima, A. *J. Am. Chem. Soc.* **2007**, *129*, 1528.

36. Schreiber, F. *Prog. Surf. Sci.* **2000**, *65*, 151.

37. Love, J. C.; Estroff, L. A.; Kriebel, J. K.; Nuzzo, R. G.; Whitesides, G. M. *Chem. Rev.* **2005**, *105*, 1103.

38. Judai, K.; Sara, K.; Amatsutsumi, S.; Yagi, K.; Yasuike, T.; Yabushita, S.; Nakajima, A.; Kaya, K. *Chem. Phys. Lett.* **2001**, *334*, 277.

39. Qian W.; Krimm, S. *J. Phys. Chem. A* **2002**, *106*, 6628.

40. Bulanin, M. O.; Domanskaya, A. V.; Kerl, K.; Maul, C. *Molecular Physics* **2006**, *104*, 2685.

41. Gole, J. L.; Prokes, S. M.; White, M. G.; Wang, T. –H.; Craciun, R.; Dixon, D. A. *J. Phys. Chem. C* **2007**, *111*, 16871.

42. Rai, D.; Joshi, H.; Kulkarni, A. D.; Gejji, S. P.; Pathak, R. K. *J. Phys. Chem. A* **2007**, *111*, 9111.

43. Frisch, M. J.; Trucks, G. W.; Schlegel, H. B.; Scuseria, G. E.; Robb, M. A.; Cheeseman, J. R.; Montgomery, J. A., Jr.; Vreven, T.; Kudin, K. N.; Burant, J. C.; Millam, J. M.; Iyengar, S. S.; Tomasi, J.; Barone, V.; Mennucci, B.; Cossi, M.; Scalmani, G.; Rega, N.; Petersson, G. A.; Nakatsuji, H.; Hada, M.; Ehara, M.; Toyota, K.; Fukuda, R.; Hasegawa, J.; Ishida, M.; Nakajima, T.; Honda, Y.; Kitao, O.; Nakai, H.; Klene, M.; Li, X.; Knox, J. E.; Hratchian, H. P.; Cross, J. B.; Bakken, V.; Adamo, C.; Jaramillo, J.; Gomperts, R.; Stratmann, R. E.; Yazyev, O.; Austin, A. J.; Cammi, R.; Pomelli, C.; Ochterski, J. W.; Ayala, P. Y.; Morokuma, K.; Voth, G. A.; Salvador, P.; Dannenberg, J. J.; Zakrzewski, V. G.; Dapprich, S.; Daniels, A. D.; Strain, M. C.; Farkas, O.; Malick, D. K.; Rabuck, A. D.; Raghavachari, K.; Foresman, J. B.; Ortiz, J. V.; Cui, Q.; Baboul, A. G.; Clifford, S.; Cioslowski, J.; Stefanov, B. B.; Liu, G.; Liashenko, A.; Piskorz, P.; Komaromi, I.; Martin, R. L.; Fox, D. J.; Keith, T.; Al-Laham, M. A.; Peng, C. Y.; Nanayakkara, A.; Challacombe, M.; Gill, P. M. W.; Johnson, B.; Chen, W.; Wong, M. W.; Gonzalez, C.; Pople, J. A. Gaussian 03, Revision D.02, Gaussian, Inc.: Pittsburgh, PA, 2003.

44. Lenk, T. J.; Hallmark, V. M.; Hoffmann, C. L.; Rabolt, J. F.; Castner, D. G.; Erdelen, C.; Rengsdorf, H. *Langmuir* **1994**, *10*, 4610.

45. Tsao, M. –W.; Hoffmann, C. L.; Rabolt, J. F.; Johnson, H. E.; Castner, D. G.; Erdelen, C.; Rengsdorf, H. *Langmuir* **1997**, *13*, 4317.

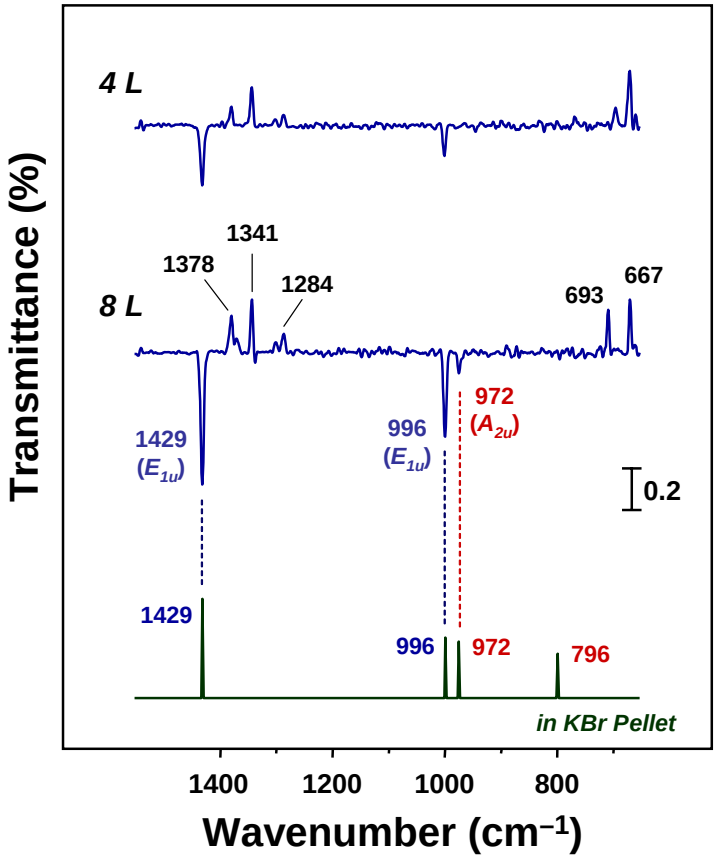

Figure 4.1. IRAS spectra in the 650–1550 cm^{-1} region after the PVD of $Cr(benzene)_2$ complexes onto $C_{10}F$-SAM at several coverage.

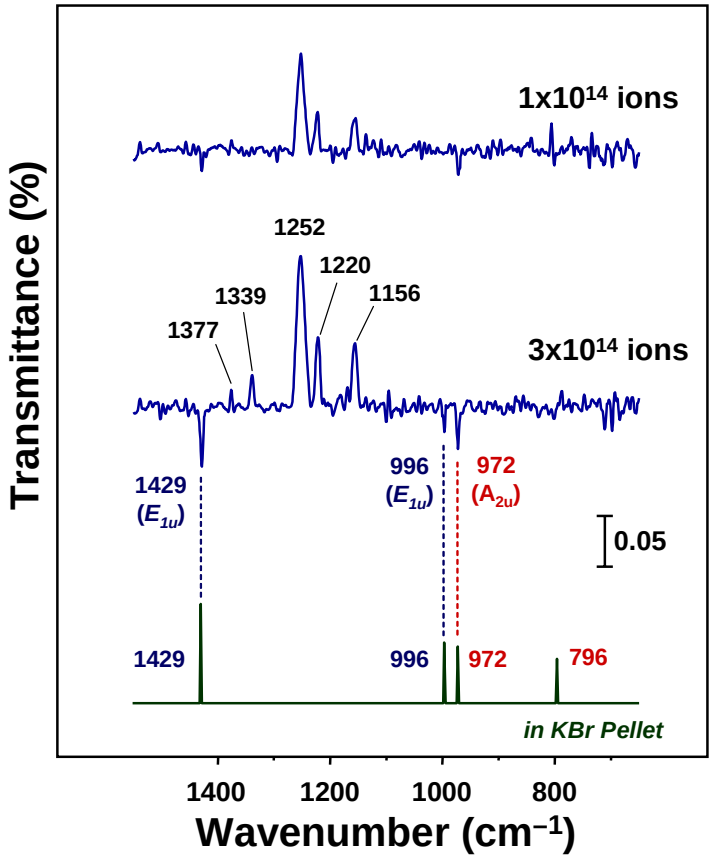

Figure 4.2. IRAS spectra in the 650–1550 cm^{-1} regions after the soft-landing of $Cr^{+}(benzene)_2$ complexes onto $C_{10}F$-SAM at several deposition numbers.

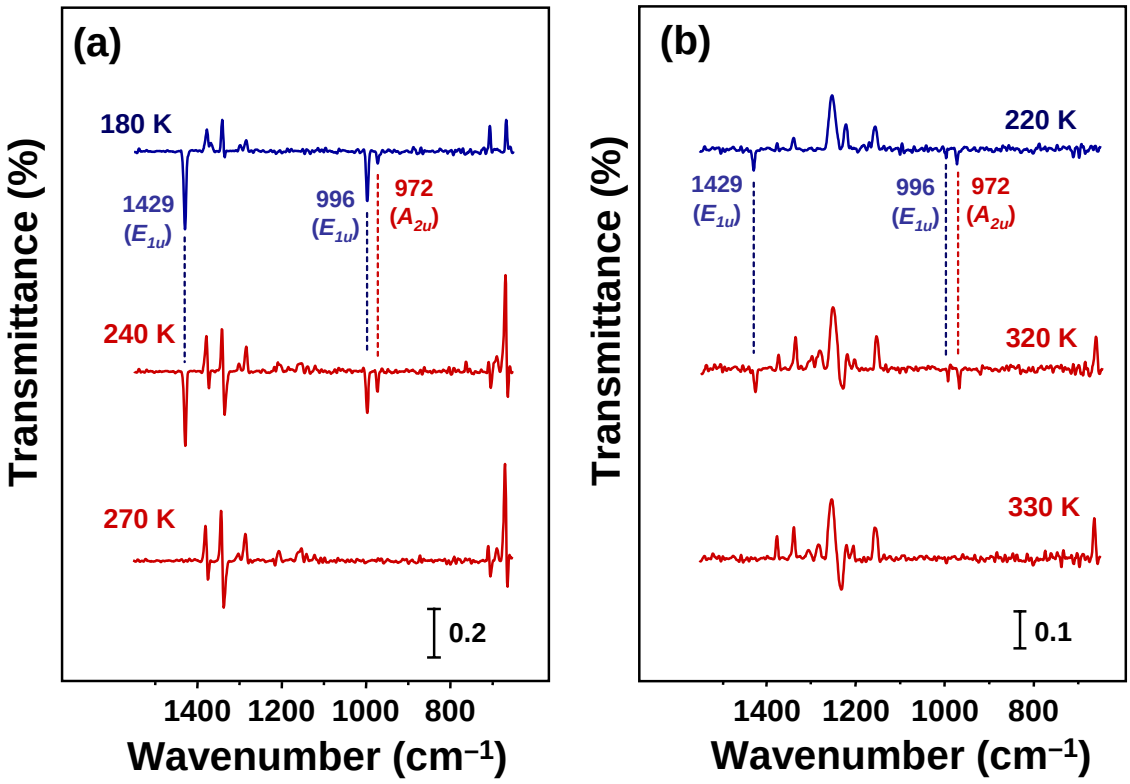

Figure 4.3. IRAS spectra showing the temperature-dependent variation of $Cr(benzene)_2/C_{10}F$-SAM after (a) the PVD of 8 L and (b) soft-landing of 3.0×10^{14} complexes.

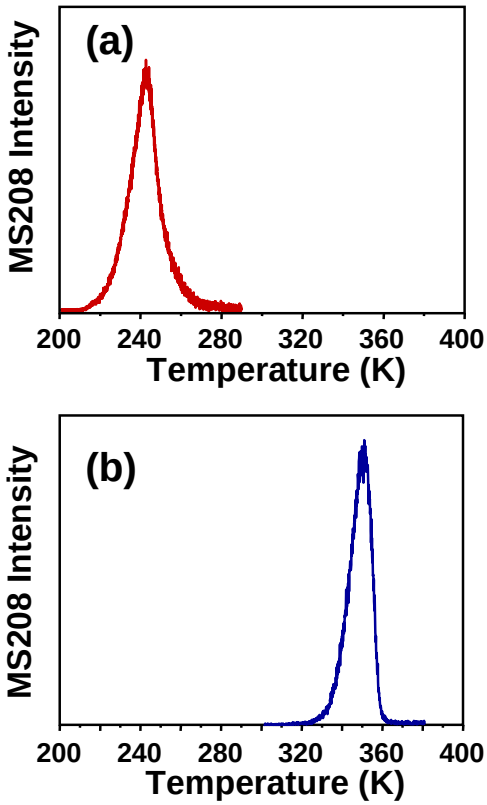

Figure 4.4. TPD spectra obtained for (a) $Cr(benzene)_2$ after the PVD of 1 L, (b) $Cr(benzene)_2$ after soft-landing of 4.0×10^{13} complexes onto $C_{10}F$-SAM substrate at 220 K.

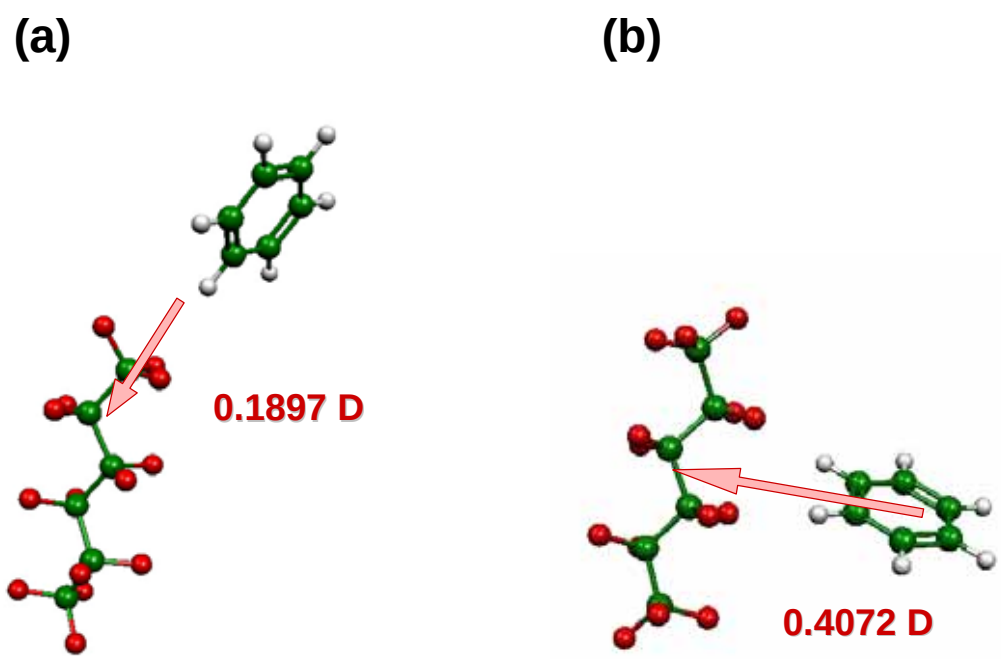

Figure 4.5. Induced dipole moment in complex of C_6H_{14} chain and benzene monomer calculated using DFT with B3LYP/6-31G(d) level.

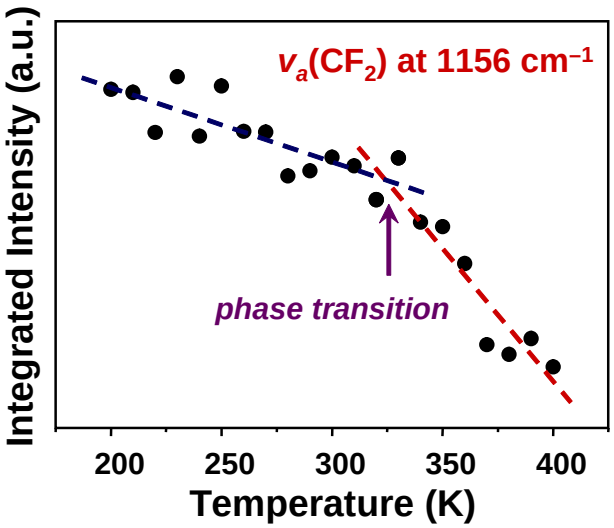

Figure 4.6. Temperature dependence of the integrated intensity of the C–F stretching mode at 1156 cm^{-1}. The blue dashed-line represents the slope due to decrease in tilt angle of the fluorocarbon chains, and the slope of the red dashed-line is brought about by appearance of *gauch* conformational defects (rotator phase) in the C_{10}F-SAM.

CHAPTER 5

Soft-Landing Isolation of Multiple-Decker V_2(benzene)$_3$ Complex

Abstract

Gas-phase synthesized multiple-decker $V_2(benzene)_3$ sandwich complexes are soft-landed onto a self-assembled monolayer of an *n*-octadecanethiol ($C_{18}H$-SAM). The infrared absorption spectrum of this complex supported on the $C_{18}H$-SAM was obtained by infrared reflection absorption spectroscopy (IRAS). The vibrational assignment of the IRAS spectrum for the $V_2(benzene)_3$ sandwich was based on a harmonic frequency analysis that employed density functional theory. The close similarity between the experimental and calculated results for the IR absorption frequencies demonstrates that the $V_2(benzene)_3$ complexes have a multiple-decker sandwich structure on the SAM substrate. Moreover, our thermal desorption study established that the sandwich complexes can be isolated on the SAM substrate up to a high temperature of ~350 K.

5.1. Introduction

Gas-phase synthesized metal–benzene sandwich complexes have generated a grate deal of attentions due to unique metal- and size-dependent characteristics, originating from their one-dimensional (1D) anisotropic structures.[1–12] Especially, the complex consisting of vanadium (V) and benzene efficiently forms multiple-decker sandwich structure: $V_n(benzene)_{n+1}$ so that, heretofore, a number of experimental and theoretical studies has been devoted to characterize its geometric,[1–5,8] electronic,[1,4–6,8] and magnetic properties.[3,6,7] Due to an 1D sandwich structure, for instance, the $V_n(benzene)_{n+1}$ clusters possess a quasi-band electronic structure[1,4] and their magnetic moments increase monotonically with the cluster size[3,8] because the unpaired d_σ electron on the V atoms coupled ferromagnetically in the cluster. Thus, the multiple-decker V–benzene cluster is one of the most attractive candidates for molecular-scale building blocks in future spin-electronic devices.

Nondissociative deposition of these gas-phase clusters through size-selection onto a pertinent substrate, a so-called "soft-landing", is one of the most emerging approaches to build up cluster-based materials. Besides, collaborating the soft-landing with a conventional surface science technique can disclose various characteristics of the gas-phase clusters accumulated on substrates. Recently, I have achieved room-temperature isolation of the gas-phase synthesized $V(benzene)_2$ complex via their soft-landing into a self-assembled monolayer (SAM) of *n*-alkanethiols.[13,14] The sandwich structure and orientation preference of the $V(benzene)_2$ supported in the SAM matrix is confirmed by infrared reflection absorption spectroscopy (IRAS), and the thermal stability and desorption kinetics are evaluated with thermal desorption spectroscopy (TDS) study. In this work, we, for the first time, examined soft-landing of multiple-decker $V_2(benzene)_3$ complex onto an *n*-octadecanethiol SAM ($C_{18}H$-SAM) substrate to perform infrared spectroscopy of the

multi-decked sandwich cluster and also evaluate their thermal stability on the SAM substrate.

5.2. Experimental and Computational Details

Details of experimental setup have been described elsewhere.[14,15] Vanadium-benzene sandwich complexes are produced in a molecular beam by laser vaporization. Cation complexes are extracted by a quadrupole deflector and only the $V_2(benzene)_3$ complexes are size-selected by a quadrupole mass spectrometer (QMS). The cations are subsequently deposited onto a $C_{18}H$-SAM substrate, which is cooled to 200 K by a liquid nitrogen cryostat, with an incident energy of ~20 eV. The deposited cations will be neutralized on the SAM substrate[14] so that the deposition number of the cluster cations can be determined by monitoring the ion current on the substrate during the deposition time. IRAS spectra for the deposited clusters are obtained with IR incident angle of ~80° with respect to the surface normal. TDS measurements are carried out with a heating rate of 1 K/s after the cluster deposition and the desorption species are detected by another QMS via electron impact ionization (~70 eV). Harmonic frequency analysis of the ideally D_{6h}-symmetric $V_2(benzene)_3$ in the singlet and triplet electronic states is performed by Gaussian 03[16] using density functional theory (DFT) with the BLYP functional. The 6-311++G(d,p) basis set is employed for benzene, while the V atoms is represented by a TZVP. The selection of the BLYP functional provides excellent results for V–benzene complex.[2,3] In this study, no imaginary frequency was calculated for any species treated.

5.3. Results and Discussion

5.3.1. Infrared Spectrum of $V_2(benzene)_3$ Complexes

Figure 5.1 shows the IR absorption spectrum in the 800–1500 cm^{-1} region obtained after the soft-landing of 2.0×10^{14} cations (~1 monolayer) of $V_2(benzene)_3$ complexes onto the $C_{18}H$-SAM substrate at 200 K, together with the calculated IR spectra of the two different electronic spin states. The close similarity in the IR absorption feature between the experimental and calculated results unequivocally indicates that the soft-landed $V_2(benzene)_3$ complexes on the substrate have a multidecker sandwich structure. Although the IR spectrum seems similar to the calculation in the triplet state rather than to that in the singlet state, the electronic spin state of the supported $V_2(benzene)_3$ complexes is not conclusively determined at present; the calculated spectra for species free from the SAM environment are too similar to distinguish the spin states for the species on the SAM. Furthermore, I did not observe any IR peaks assignable to the smaller $V(benzene)_2$ complex, which might be produced by fragmentation collisions with the surface. For example, no peak at 988 cm^{-1} for $V(benzene)_2$ on the $C_{18}H$-SAM [16] could be observed.

Based on the harmonic frequency analysis, I can assign the three IR absorption bands of $V_2(benzene)_3$ as follows: the first at 957 cm^{-1} to the symmetric ring-breathing mode [ν_s(CC)] of the two terminal benzene rings, the second at 979 cm^{-1} to the C–H in-plane bending mode [ν_{i-p}(CH)] of the terminal rings, and the third at 1379 cm^{-1} to the asymmetric C–C stretching mode [ν_a(CC)] of the middle ring. The vibrational frequency of ν_s(CC) for $V_2(benzene)_3$ is the same as that for $V(benzene)_2$ at 956 cm^{-1}, while the frequencies of the ν_{i-p}(CH) and ν_a(CC) modes are red-shifted from those for $V(benzene)_2$ at 988 and 1418 cm^{-1}, respectively.[12,15–16] The measured red-shift of these modes with the complex size is consistent with the computed results.[11]

5.3.2. Thermal Desorption study

Displayed in Figure 5.2 is the temperature-induced variation of the IRAS spectra for

V_2(benzene)$_3$/ C_{18}H-SAM, which evaluates the thermal stability of the soft-landed clusters on the substrate. While I observe no spectral change up to surface temperature of 300 K, the peak intensity of the ν_s(CC) mode (A_{2u} symmetry) at 957 cm^{-1} starts to decrease at 310 K. Subsequent to the partial intensity reduction, the IR spectrum remains unchanged around 320 to 340 K. However, increasing surface temperature up to 350 K poses the intensity of all the peaks to decrease, and the bands are completely vanished at 360 K. The results represent that the thermal desorption of the V_2(benzene)$_3$ supported on the C_{18}H-SAM substrate is suppressed upon high temperature region of ~80 °C, which is much higher than the desorption temperature for V(benzene)$_2$/ C_{18}H-SAM of ~25 °C.[14] Decrease in only the A_{2u} mode at 310 K may indicate an orientational change of the V_2(benzene)$_3$ cluster on the SAM substrate because the relative IR intensity between the A_{2u} and E_{1u} modes reflects the orientational preference of the D_{6h}-symmetric clusters on the surface in this IRAS measurement.[13,14]

Figure 5.3 demonstrates the TDS spectra taken after deposition of 3×10^{13} V_2(benzene)$_3$ cations onto the C_{18}H-SAM at 200K. I recorded the desorption species for the parent ion: V_2(benzene)$_3^+$ and for its fragment ions: V_2(benzene)$_2^+$, V(benzene)$_2^+$, and benzene$^+$. Only one peak was observed in the desorption spectrum of the V_2(benzene)$_3^+$ at 378 K, however, the other fragments species display two peaks in the spectra. The peak at 378 K, which is observed in all the fragment spectra, is attributed to the desorption of the V_2(benzene)$_3$ and the signals of the fragments are caused by the electron impact ionization event of the desorbed parent clusters in the mass spectrometer. The peak at 320 K displayed in the spectra for benzene$^+$ and V(benzene)$_2^+$ would be due to the desorption of the V(benzene)$_2$ clusters produced by the collision of the V_2(benzene)$_3$ with the surface. In this study, the kinetic energy distribution of the cluster beam is estimated to be ~20 eV at full-width half-maximum so that a small amount of the clusters were inevitably deposited with high collision energy

(>40 eV), which would induce dissociation of the projectile V_2(benzene)$_3$ clusters in the landing process on the substrate. Furthermore, the peak at 335 K clearly observed in the signal for V_2(benzene)$_2^+$ would be assigned to the desorption of the V_2(benzene)$_2$ which is also produced on the surface in the landing process. The TDS results indicate that the some of deposited V_2(benzene)$_3$ clusters dissociate to V(benzene)$_2$ and V_2(benzene)$_2$ in the landing process, and these fragments are co-adsorbed on the C_{18}H-SAM substrate together with the non-dissociatatively deposited V_2(benzene)$_3$.

As noted above, however, I observed no IR absorption peak originated from these co-adsorbed fragments in the IRAS measurement, indicating that the quantity of the fragments is under detection limit of the IRAS measurement. The IR absorption intensity for the fragments, furthermore, would be much weaker than that for V_2(benzene)$_3$. Indeed, the DFT calculation represents that magnitudes of IR absorption for V(benzene)$_2$ and V_2(benzene)$_2$ reduces to about one-third and half with respect to that for V_2(benzene)$_3$, respectively. Ultimately, it should be emphasized that every peak on the IRAS spectra taken at over the desorption temperature of the fragments (~310 K), displayed in Figure 5.2. originates thoroughly from the V_2(benzene)$_3$ clusters supported on the C_{18}H-SAM matrix. In closing, matrix-isolation of gas-phase synthesized multiple-decker V_2(benzene)$_3$ sandwich complexes in the SAM substrate with high thermal stability is anticipated to open up new possibilities for exploiting these complexes as molecular-scale photo-magnetic building blocks in applications for future cluster-based materials.

5.4. Conclusion

Gas-phase synthesized multiple-decker V_2(benzene)$_3$ complexes are isolated in the C_{18}H-SAM matrix. The infrared spectrum of the multiple-decker V_2(benzene)$_3$ complexes

are obtained for the first time by use of the IRAS measurement. An agreement of the obtained IRAS spectrum with calculated IR spectrum demonstrates that the $V_2(benzene)_3$ complexes retain their one-dimensional multiple-decker structure intact. Thermal desoption study reveals that the matrix-isolated $V_2(benzene)_3$ complexes resist the thermal desorption up to a high temperature of ~350 K. The achievement of soft-landing isolation of gas-phase synthesized multiple-decker $V_2(benzene)_3$ sandwich complexes, presented in this study, with high thermal stability is anticipated to open up new possibilities for exploiting these complexes as molecular-scale photo-magnetic building blocks in applications for future cluster-based materials.

References

1. Hoshino, K.; Kurikawa, T.; Takeda, H.; Nakajima, A.; Kaya, K. *J. Phys. Chem.* **1995**, *99*, 3035.
2. Weis, P.; Kemper, P. R.; Bowers, M. T.; *J. Phys. Chem. A* **1997**, *101*, 8207.
3. Wang, J.; Acioli, P. H.; Jellinek, J. *J. Am. Chem. Soc.* **2005**, *127*, 2812.
4. Yasuike, T.; Yabushita, S. *J. Phys. Chem. A* **1999**, *103*, 4533.
5. Kandalam, A. K.; Rao, B. K.; Jena, P.; Pandey, R. *J. Chem. Phys.* **2004**, *120*, 10414.
6. Pendy, R.; Rao, B. K.; Jena, P.; Blanco, M. A. *J. Am. Chem. Soc.* **2001**, *123*, 3799.
7. Miyajima, K.; Nakajima. A.; Yabushita, S.; Knickelbein, M. B.; Kaya, K. *J. Am. Chem. Soc.* **2004**, *126*, 13202.
8. Nakajima, A.; Kaya, K. *J. Phys. Chem. A* **2000**, *104*, 176.
9. van Heijnsbergen, D.; von Helden, G.; Meijer, G.; Maitre, P.; Duncan, M. A. *J. Am. Chem. Soc.* **2002**, *124*, 1562.
10. Jaeger, T. D.; van Heijnsbergen, D.; Klippenstein, S. J.; von Helden, G.; Meijer, G.; Duncan, M. A. *J. Am. Chem. Soc.* **2004**, *126*, 10981.
11. Wang, J.; Jellinek, J. *J. Phys. Chem. A* **2005**, *109*, 10180.
12. Lyon, J. T.; Andrews, L. *J. Phys. Chem. A* **2005**, *109*, 431.
13. Mitsui, M.; Nagaoka, S.; Matsumoto, T.; Nakajima, A. *J. Phys. Chem. B* **2006**, *110*, 2968.
14. Nagaoka, S.; Matsumoto, T.; Okada, E.; Mitsui, M.; Nakajima, A. *J. Phys. Chem. B* **2006**, *110*, 16008.
15. Judai, K.; Sara, K.; Amatsutsumi, S.; Yagi, K.; Yasuike, T.; Yabushita, S.; Nakajima, A.; Kaya, K. *Chem. Phys. Lett.* **2001**, *334*, 277.
16. Frisch, M. J.; Trucks, G. W.; Schlegel, H. B.; Scuseria, G. E.; Robb, M. A.;

Cheeseman, J. R.; Montgomery, J. A., Jr.; Vreven, T.; Kudin, K. N.; Burant, J. C.; Millam, J. M.; Iyengar, S. S.; Tomasi, J.; Barone, V.; Mennucci, B.; Cossi, M.; Scalmani, G.; Rega, N.; Petersson, G. A.; Nakatsuji, H.; Hada, M.; Ehara, M.; Toyota, K.; Fukuda, R.; Hasegawa, J.; Ishida, M.; Nakajima, T.; Honda, Y.; Kitao, O.; Nakai, H.; Klene, M.; Li, X.; Knox, J. E.; Hratchian, H. P.; Cross, J. B.; Bakken, V.; Adamo, C.; Jaramillo, J.; Gomperts, R.; Stratmann, R. E.; Yazyev, O.; Austin, A. J.; Cammi, R.; Pomelli, C.; Ochterski, J. W.; Ayala, P. Y.; Morokuma, K.; Voth, G. A.; Salvador, P.; Dannenberg, J. J.; Zakrzewski, V. G.; Dapprich, S.; Daniels, A. D.; Strain, M. C.; Farkas, O.; Malick, D. K.; Rabuck, A. D.; Raghavachari, K.; Foresman, J. B.; Ortiz, J. V.; Cui, Q.; Baboul, A. G.; Clifford, S.; Cioslowski, J.; Stefanov, B. B.; Liu, G.; Liashenko, A.; Piskorz, P.; Komaromi, I.; Martin, R. L.; Fox, D. J.; Keith, T.; Al-Laham, M. A.; Peng, C. Y.; Nanayakkara, A.; Challacombe, M.; Gill, P. M. W.; Johnson, B.; Chen, W.; Wong, M. W.; Gonzalez, C.; Pople, J. A. Gaussian 03, Revision D.02, Gaussian, Inc.: Pittsburgh, PA, 2003.

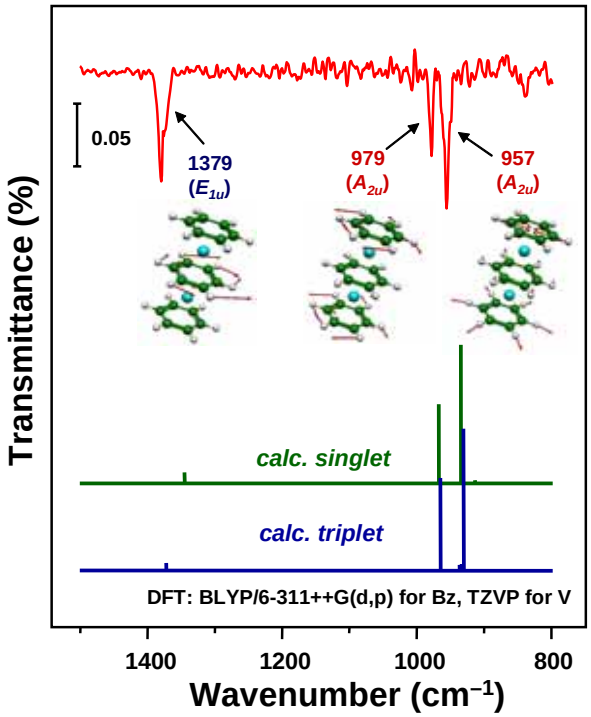

Figure 5.1. IRAS spectrum of the V_2(benzene)$_3$ complex on C_{18}H-SAM, along with calculated IR absorption spectra for singlet and triplet states.

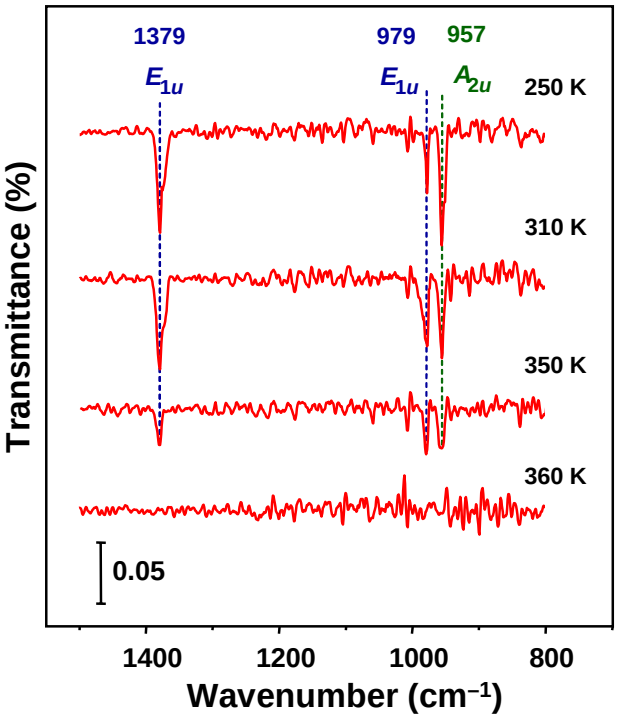

Figure 5.2. IRAS spectra showing the temperature-dependent variation of the V_2(benzene)$_3$ complex on C_{18}H-SAM.

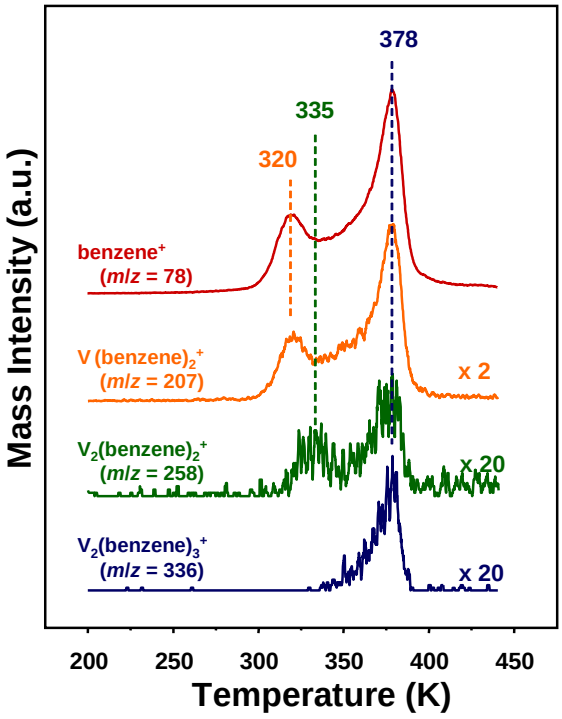

Figure 5.3. Multiplex thermal desorption data for $V_2(benzene)_3$ complex soft-landed on $C_{18}H$-SAM.

CHAPTER 6

Construction of Portable Cluster Source and its Application for Microscopic Study of Soft-Landed Clusters

Abstract

A newly designed portable cluster source mounted high-pressure, high-temperature, high-speed pulsed valves for generating supersonic beam is presented. A quadrupole deflector and time-of-flight mass spectrometer (TOF-MS) are equipped at outlet of the cluster generation stage; it is thus possible to extract the generated cluster ions via measurement of their mass distribution. The home-build TOF-MS system, consisting of three acceleration stages, performs with a high resolution ($t/\Delta t$ = 1000) in a small package whose flight tube length is only 200 mm. The portable cluster source is applied for cluster-deposition studies. Installing the portable cluster source into scanning probe microscope realizes the measurements of physical topographic images of the clusters soft-landed on the SAM matrices

6.1. Introduction

During the last two decade, the field of cluster science has seen a large growth and shed light on the size-specific novel properties of the clusters in gas phase. Advent of soft-landing technique further has opened up the new field of cluster science, where the physical and chemical properties of size-selected clusters at surfaces are well characterized by collaborating conventional surface science technique. Numerous experimental and theoretical efforts have demonstrated that the clusters supported on a surface have enough potential for application to innovative nanostructured functional materials.

There are a great number of surface science techniques that partially extract the information on a surface or adsorcates on the surfaces, e.g. structure, morphology, electronic state, magnetic response, and so on. However, a wide variety of surface science instruments are required in order to elucidate the various kinds of physical and chemical properties of the clusters supported on the surface. The opportunity to study the cluster/surface system can be provided by installing the surface science instruments into the large-scale soft-landing apparatus where the cluster generation source, ion optics, and mass filter are mounted. Thus, each conventional soft-landing apparatus can provide only limitary information about the cluster/surface system.

In order to make a breakthrough of the field of cluster/surface science, I developed a portable cluster source, which is capable to directly combine the various kinds of surface science instruments under high or ultra-high vacuum conditions. In this chapter, a newly designed portable cluster source equipped with a quadrupole deflector and time-of-flight mass spectrometer (TOF-MS) is presented. The schematic diagram of portable cluster source is shown in Figure 6.1. High-resolution performance was successfully obtained for the home-build TOF-MS even in a small package. The portable cluster source was applied to

microscopic study of vanadium-benzene complexes soft-landed on the SAM matrices by combining the cluster source with a scanning tunneling microscope. The first time measurement of the topographic images of sandwich complexes soft-landed on the SAM matrices are presented.

6.2. Experimental Section

6.2.1. Design of Cluster Generation Stage

In order to provide portability for the cluster source machine, the cluster generation chamber was designed to be both a small and lightweight package. For a material of the generation chamber, thus, a lightweight aluminum alloy (A5052) was used. A cubic chamber 130 mm on a side is adapted for the generation chamber where standard ISO 100 flanges (130ϕ × 12T) can be mounted. It is also required to perform a small-scale pumping system so that a high-pressure, high-temperature, high-speed pulsed valve provided by Prof. Uzi Even and Mr. Nachum Lavie, a so-called the Even-Lavie valve, is used to produce supersonic molecular beam. The short operation time of the Even-Lavie valve generates very little gas load so that the gas throughput is estimated to be only 0.02 L·Torr/s at 100 bar operating pressure and a 10 Hz repetition rate. It is thus expected that a small throughput of vacuum pumping system will perform to maintain a high vacuum condition (~10^{-6} Torr) in the generation chamber even operating the Even-Lavie valves. A small 200 L/s turbo molecular pump is therefore used for the generation chamber backed with a 250 L/min scroll pump (ISP-250B, ANEST IWATA).

The laser vaporization technique is applied to generate clusters in this machine. The cluster beam can be produced by supersonic expansion of carrier gas (commonly He) from the Even-Lavie valve, which effectively cools down the vaporized species to aggregate and form

the clusters. The cluster generation stage is mounted on an ISO 100 flange, where the Even-Lavie valve, a dual-rod rotation system, cluster generation block (cluster reaction room) are installed. A pulsed Nd^{3+}:YAG laser (Tempest, New Wave Research) is used to vaporize metal target rod, which is mechanically rotated to efficiently provide a plasma with long-term stability. The visible green color of the second harmonics of Nd^{3+}:YAG is employed to help the adjustment of the path of the laser beam. The side faces of the cubic generation chamber mount acrylic-based transparent flanges where quart plates are positioned for the laser beam entry. The Even-Lavie valve with an integrated heating element, which can operate a wide temperature rage of 100–520 K, is applied to inject the vapors of organic molecules (typically benzene) diluted by He or Ar. Thus, the cluster generation state can produce not only metal clusters but also organometallic complexes by a reaction between laser vaporized metal atoms with organic molecular vapors. The operation of the laser pulse and valve pulses are mutually synchronized and it is capable to perform up to repetition rate of 30 Hz.

In order to separate (or extract) the charged species from the generated clusters, a home-build quadrupole deflector is positioned at outlet of the cluster generation stage via a gate valve ($130\phi \times 30$T with a 6ϕ skimmer) designed by R.Yamamoto in a second chamber (ICF 152 cubic chamber). The quadrupole deflector is also design to be a compact size, measured 47 mm in wide and depth, and 52 mm in height. The second chamber is pumped by a 300 L/s turbo molecular pomp (PT300, Mitsubishi) backed with a 250 L/min Scroll pump (ISP-250B, ANEST IWATA).

6.2.2. Time-of-Flight Mass Spectrometry System

In order to analyze the mass distribution of the generated clusters, a time-of-flight mass spectrometer (TOF-MS) was constructed. The TOF-MS system, mainly consist of an

acceleration stage, free flight tube, and ion detector, is also designed to perform a small package. The design of acceleration stage is illustrated in Figure 6.2. The acceleration stage consists of three acceleration plates and one grand plate so that it is built of three acceleration stages. Each acceleration region is a short insulating cylinder made from machinable ceramic. The inside diameter is of each cylinder is 35 mm and length of the tube is designed to be 20 mm for the first acceleration region (repelling region), 18 mm for the second region, and 10 mm the final acceleration region. Treatment of brush-coat of a thick film restive on the each cylinder inside surface was performed to create a glazed resistive surface via process of heating to 800 °C. This resistance is a comprised between two conflicting requirement. High resistance will reduce the current drawn from the high voltage pulser but will also lengthen the voltage rise due to stray capacitance. The beam entrance hole on the first acceleration plate (repelling plate) will produce potential error inside the acceleration stage, thus a skimmer (8ϕ) is used for the beam entrance to correct such potential error. The acceleration stage is mounted on inner face (vacuum side) of an ICF 152 flange with 40ϕ hole at center and the grounded flight tube, where the accelerated ions free fights to a detector, is connected to the other face (air side) of the flange. A microchannel plate (MCT) is used to detect the arrival ions after the free flight.

In the TOF-MS, bringing all the ions of the same mass but different initial positions to the detector at same time, a so-called space focusing is required to obtain high resolution.[1–4] The computer parametric optimization procedure for the designed TOF-MS is successfully performed through collaboration of Prof. Uzi Even (Tel Aviv Univ., Israel). The computer simulation provides that the beat combination of voltages for the various acceleration plates is: 1000 V for the first, 717 V for the second, and 314 V for the final acceleration plate, respectively. For cation of mass number of 1000, flight time is around 23 μs and its pulse

width (of the ion packet) is about 20 ns so that the resolution of ~ $t/\Delta t$ = 1000 is performed. The result estimates that the TOF-MS has an ability to obtain a mass spectrum with a resolution grater than $m/\Delta m$ = 200.

6.2.3. Cluster Deposition and Scanning Probe Microscopy

The cation species extracted from the cluster beams by the quadrupole deflector can be guided via an octapole ion guide and electrostatic lens. In this study, the potable cluster source are tried to connect the scanning probe microscopy (SPM) through collaboration of Prof. H. Onishi's group (Kobe Univ., Japan) so as to gain insight into the adsorption regime of the clusters soft-landed on the SAM matrices.

The extracted cluster cations are leaded to the deposition chamber where a target sample substrate is mounted by use of a series of octapole ion guides and an electrostatic lens. The substrate can be cooled down to ~80 K by direct contact with liquid nitrogen reservoir and the substrate temperature can be controlled by a heating element mounted on the sample holder. The surface area of the sample substrate for SPM measurement is unfortunately very small (3 × 7 mm) so that the focusing of ion beams is needed to increase the cluster flux density on the substrate. For this reason, I employ a conical octapole ion guide, which is newly invented by Röttgen et al., in order to tightly focus the ion beam onto such a small substrate with high transmittance. The illustration and a photograph of the conical octapole ion guide designed in this study is shown in Figure 6.3. The deposition chamber is directly connected to the preparation chamber of the SPM instrument (JSPM-4500A, JEOL) so that it is capable to immediately transfer the cluster-deposited sample substrate through into the analysis chamber for the SPM measurement under high vacuum condition. It should be note that the cluster deposition is carried out with cooling the temperature of the target substrate, however, the

SPM measurement of the cluster-deposited substrate is performed at room temperature.

6.3. Result and Discussion

6.3.1. Cluster Source Performance

Profiles of gas pulses injected from the Even-Lavie valves are evaluated by use of a fast ion gauge analyzer. The analyzer is positioned at center of the generation chamber where the two gas pulses (one is carrier gas containing vaporized species and the other is organic vapor) are intersected to react to organometallcs. Figure 6.4 represents a typical gas pulse at a pressure of 50 atm of He and a pressure of 10 atm of benzene diluted in He, along with the electronic pulse signal. The time delay from the electronic pulse signal rising to peak maximum of gas pulse is estimated to be 127 μs for 50-atm He and 237 μs for 10-atm benzene/He, respectively. Although a sharp pulse of 40 μs at FWHM is detected for the expansion of the neat He gas, benzene-containing He gas pulse provides broad profile of 250 μs at FWHM. During the operation of the two Even-Lavie valves, the vacuum level is retained around 2×10^{-4} Torr, while the base pressure typically reaches $\sim10^{-7}$ Torr in the generation chamber.

Mass distribution of laser-vaporized vanadium (V) target cooled by He pulse gas at a pressure of 50 atm is shown in Figure 6.5. The predominantly observed signal at 5.411 μs is attributed to V^+ (m/z = 51) and its oxide and hydrates are clearly detected in the mass spectrum. The laser-vaporized V atoms will be reacted with oxygen and/or water, which are presumably containing the He carrier gas or the metal rod surface and remanent in the generation chamber. Calibration of time-of-flight to mass number and chemical species obtained by this TOF-MS system is listed in Table 6.1.

6.3.2. Mass Distribution of Vanadium–Benzene Complexes

The vanadium-benzene complexes are produced by the reaction of laser vaporized V atoms carried by 50-atm He gas with benzene vapors diluted with 5-atm He gas. The typical mass spectra for the vanadium-benzene complexes obtained by varying the delay time of high-voltage pulse for the acceleration stage is shown in Figure 6.6. The profile of the mass spectra is highly depending on the delay time. In this study, the pulse width of the high voltage supply is set to 50 μs, the result thus suggests that the ion packet of the vanadium-benzene complexes is widely distributed in the space, and the TOF-MS extracts only fraction of the packet at each delay time. Since the heavy species arrive the acceleration stage later than small masses, increase in delay time clearly provides the mass signals originating from high-mass species. The magic numbered behavior of $V_n(benzene)_{n+1}$ (n = 1–3) is found in the mass spectrum at normalized delay time of 160 μs, a result which is indicating that V-benzene complexes produced in this cluster source form multiple-decker sandwich structure.

The ion current of the ion packet of the V-benzene complexes thus generated is monitored via detecting the neutralization charge during their deposition onto an aluminum-based plate through an electrometer with accelerate potential of −100 V. At the entrance of the quadrupole deflector, the ion current of ~7 nA is measured. The ion current decreases to ~4 nA at the outlet of the deflector and further decrease to ~3.5 pA at the deposition chamber. The cluster ion is mostly lost through the octapole ion guides and electrostatic lens between the quadrupole deflector and deposition chamber.

6.3.3. Microscopic Study of Vanadium–Benzene Complexes Soft-Landed on Organic Monolayer Matrices

The physical topography of the cluster-deposited SAM matrices is investigated by combining the portable cluster source with the SPM instrument. Photography of the

combined apparatus is shown in Figure 6.7. In this study, soft-landing of the vanadium-benzene complexes on to $C_{18}H$-SAM and $C_{10}F$-SAM with a collision energy of ~20 eV are carried out.

Figure 6.8 shows that typical noncontact atomic force microscopic (NC-AFM) image of $C_{10}F$-SAM matrix and plot of arbitrary cross section is listed together. Several darker depressions and step sites on the surface are clearly observed. The cross section presents that the depth of the darker depression is nearly equal to the height of step, a result which is likely indicating that the depressions is corresponding to the vacancy island of the $C_{10}F$-SAM, where the SAM formed on monatomic vacancy of the gold surface. Such vacancy island is probably generated by the reconstruction process of Au(111) surface due to the adsorption of the thiols. These darker depressions are also measured on the surface of $C_{18}H$-SAM matrices. The distribution of depth of the depression on several topographic images for $C_{18}H$-SAM and $C_{10}F$-SAM matrices are shown in Figure 6.9, and the histograms are fit by Gaussian function. The depth distribution obtained is ~0.24 nm for $C_{18}H$-SAM and ~0.22 nm for $C_{10}F$-SAM matrices so that the darker depressions provided in this measurement most probably reflect the vacancy islands.

Figure 6.10 shows representative topographic images of the $C_{18}H$-SAM after the soft-landing of V-benzene complexes at collision energy of 20 eV, obtained by NC-AFM. The arbitrary cross sections are also displayed in Figure 6.10. Several bright spots are clearly observed on the $C_{18}H$-SAM after the deposition of the complexes. The cross section represents that they are corresponding to adsorbates whose heights are around 2–3 nm on the $C_{18}H$-SAM. Similar topographic images are also provided by NC-AFM measurements of the $C_{10}F$-SAM after the soft-landing of V-benzene complexes at collision energy of 20 eV, shown in Figure 6.11. Several bright spots are observed inside the vacancy islands and near

the surface steps on the $C_{10}F$-SAM. The arbitrary cross section analyzes that the heights of adsorbates are around 3–5 nm. On both the $C_{18}H$-SAM and $C_{10}F$-SAM, unfortunately, a molecularly resolve topographic image could not be observed.

In order to identify the columnar adsorbates, the size distributions of the bright spots on each SAM matrices are illustrated in Figure 6.12 and the distributions are fit by Gaussian function. For the $C_{18}H$-SAM, the dimensions of the columnar adsorbates are close to ~0.25 nm in height and ~5.0 nm in width, and the size distribution is narrow. However, the broad distribution in size is provided for the columnar adsorbates on the $C_{10}F$-SAM matrices. The averaged dimensions are measured to be ~0.38 nm in height and ~10.2 nm in width, which are comparatively larger than that for the $C_{18}H$-SAM. It should be note that these bright spots are only observed after the cluster deposition event and the composition of the deposited species are identified by TOF mass spectra (see Fig. 6.6) to be V-benzene sandwich complexes. Moreover, the nondissociative depositions of the $V(benzene)_2$ and $V_2(benzene)_3$ complexes onto the $C_{10}F$- and $C_{18}H$-SAMs at 20-eV collision energy are also confirmed by the IRAS and TDS studies. Thus, the columnar adsorbates on the SAM matrices would be originating from the deposited V-benzene sandwich complexes.

As mentioned above, the SPM measurement is performed at room temperature so that the $V(benzene)_2$ complexes whose desorption temperature is ~290 K on the $C_{18}H$-SAM substrate will be desorbed from the substrate. Therefore, it is expected that the major composition of the columnar adsorbates on the $C_{18}H$-SAM is $V_2(benzene)_3$; Note that $V_3(benzene)_4$ complexes also detected by TOF-MS, however, the abundance is extremely small. The dimension of the $V_2(benzene)_3$ complex measures ~0.7 nm along the molecular axis and the width of the capping benzene ring is estimated to be ~0.5 nm. Assuming that the $V_2(benzene)_3$ complexes are trapped at the vacancy islands, whose depth is ~2.4 nm, with

their molecular axis largely tilts to the surface, NC-AFM measurements provide bright spots with height of ~0.25 nm on the $C_{18}H$-SAM. Such adsorption regime is conceivable because the increase in surface temperature (up to room temperature) after the deposition promotes the surface diffusion of the complexes at terrace site, where the diffusion barrier is relatively small, to trap the diffused complexes at defect sites, i.e. vacancy island, steps, and kinks. As a consequence, the complexes are aggregated each other at the defect sites (mainly vacancy islands) and form the columnar islands on the $C_{18}H$-SAM. The orientational preference of the $V_2(benzene)_3$ complexes with their molecular axis largely tilts to the surface is also supported by the IRAS study (see Fig. 5.2). It has been confirmed that, with increasing temperature, the $V_2(benzene)_3$ complex tilts its molecular axis greatly on the $C_{18}H$-SAM substrate. The schematic illustration of the adsorption regime of V-benzene complexes on the $C_{18}H$-SAM at room temperature concluded by microscopic studies is shown in Figure 6.13.

In the case of the deposition onto the $C_{10}F$-SAM, in contrast, the complexes form the columnar islands of varied sizes. Furthermore, the columnar islands grow to almost ~10 nm in width which is larger than the width of the vacancy island, while the columnar islands whose width is larger than the vacancy is not observed for the $C_{18}H$-SAM. The island grow rate would be intercorrelate with the mobility of the complexes on the surface, therefore, the change in the island sizes between the two SAM matrices indicates that surface diffusion kinetics of the complexes on the $C_{10}F$-SAM is different from that on the $C_{18}H$-SAM. Differences of the activation barrier for the thermal diffusion of the complexes between on the two SAM matrices may provide measurable changes in the formation of the islands.

6.4. Conclusion

The portable cluster source equipped with a quadrupole deflector and TOF-MS system is newly designed. The small packed TOF-MS system provides mass spectra with a sufficient resolution ($m/\Delta m$ = 200) to analyze the mass distribution of typical clusters by use of three acceleration stages. The microscopic studies of the $C_{10}F$- and $C_{18}H$-SAM substrates after soft-landing of V-benzene complexes are performed by combining the portable cluster source into the SPM instrument. The soft-landed complexes are forming the columnar islands at the vacancy island of the SAM surface at room temperature. Change in island size between the $C_{10}F$-SAM and $C_{18}H$-SAM matrices is observed, a result which may be reflecting the differences of the activation barrier for the thermal diffusion of the complexes between on the two SAM matrices.

References

1. Even, U.; Dick, B. *Rev. Sci. Instrum.* **2000**, *71*, 4415.

2. Even, U.; Dick, B. *Rev. Sci. Instrum.* **2000**, *71*, 4421.

3. Wiley, W.; McLaren, I. H. *Rev. Sci. Instrum.* **1955**, *26*, 1150.

4. Chandezon, F.; Huber, B.; Ristori, C. *Rev. Sci. Instrum.* **1994**, *65*, 3344.

Table 6.1. Calibration of Time-of-Flight to Mass Number for Newly Designed TOF-MS

time of flight (μs)	mass number (*m*/*z*)	cation species
5.411	51	V
6.175	67	VO
6.263	69	$V(H_2O)_1$
7.011	87	$V(H_2O)_2$
7.681	105	$V(H_2O)_3$
8.295	129	$V(H_2O)_4$
8.863	141	$V(H_2O)_5$
9.395	159	$V(H_2O)_6$

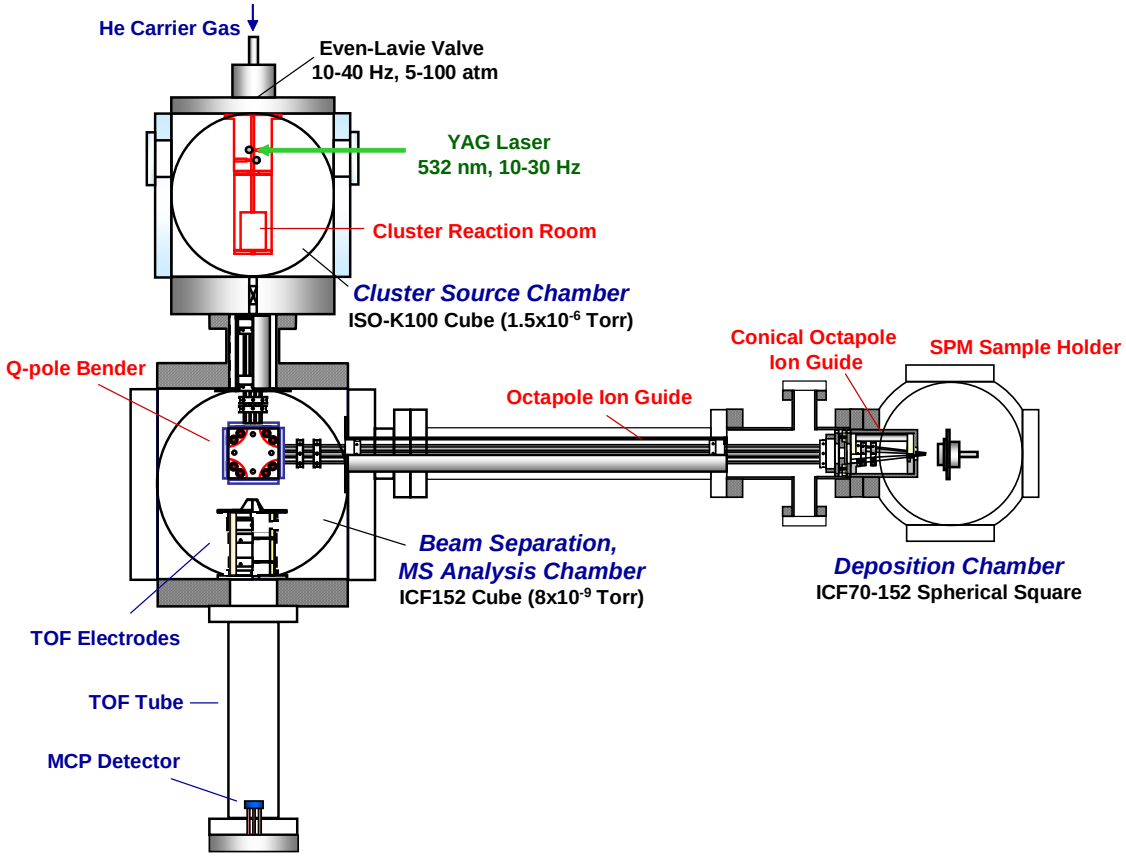

Figure 6.1. Schematic diagram of a newly designed portable cluster source.

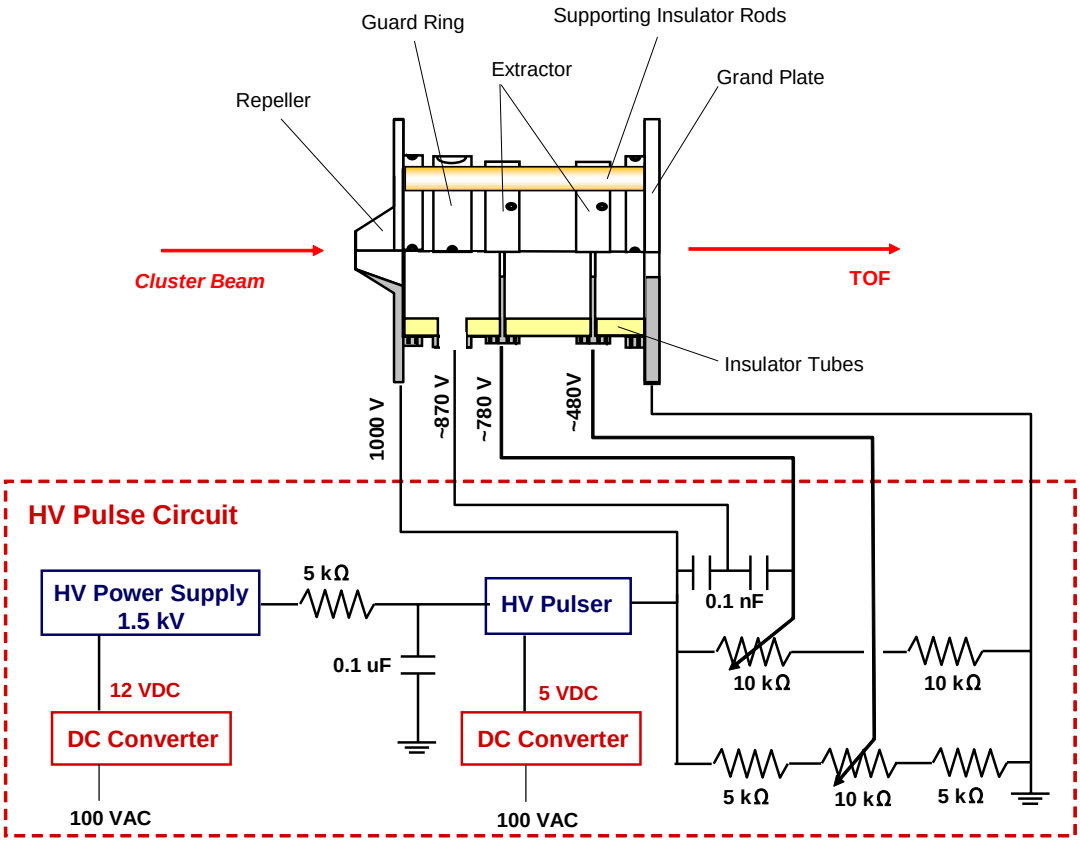

Figure 6.2. Schematic diagram of acceleration stages for home-build time-of-flight mass spectrometry.

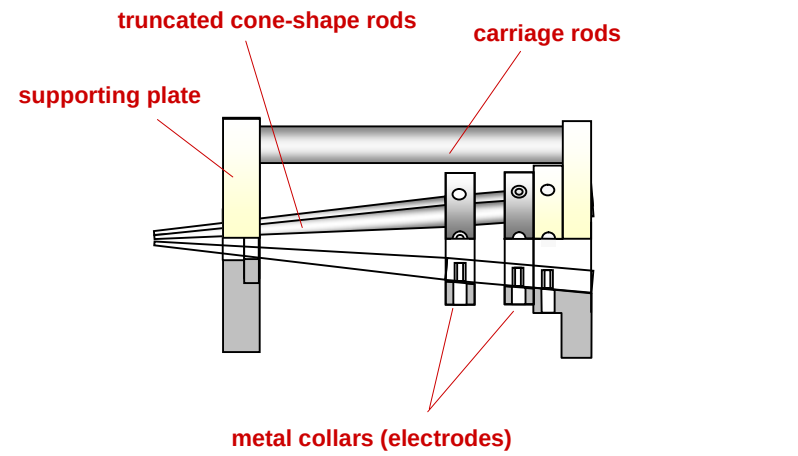

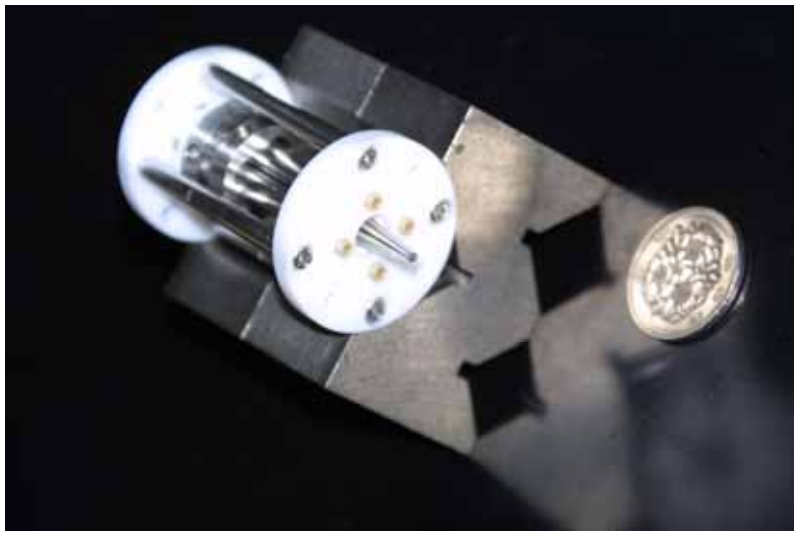

Figure 6.3. Schematic and photographic images of conical octapole ion guides

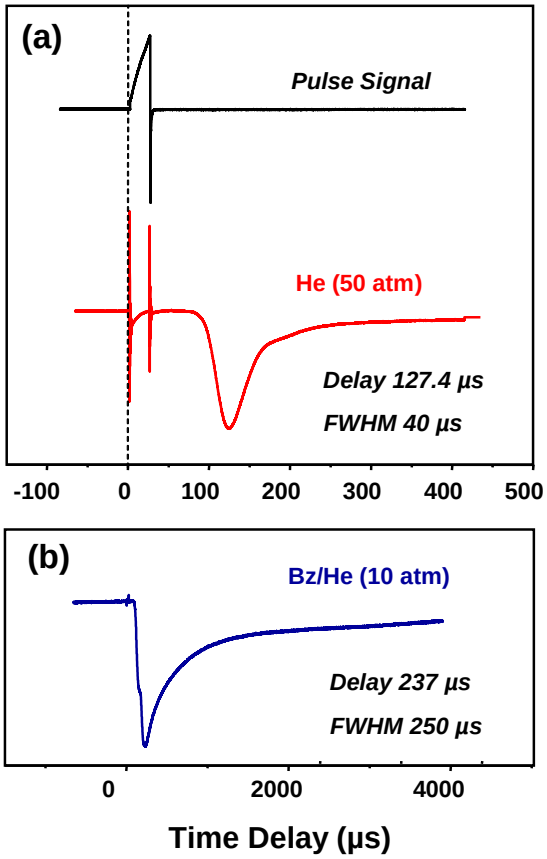

Figure 6.4. Profiles of gas pulses injected from the Even-Lavie valves.

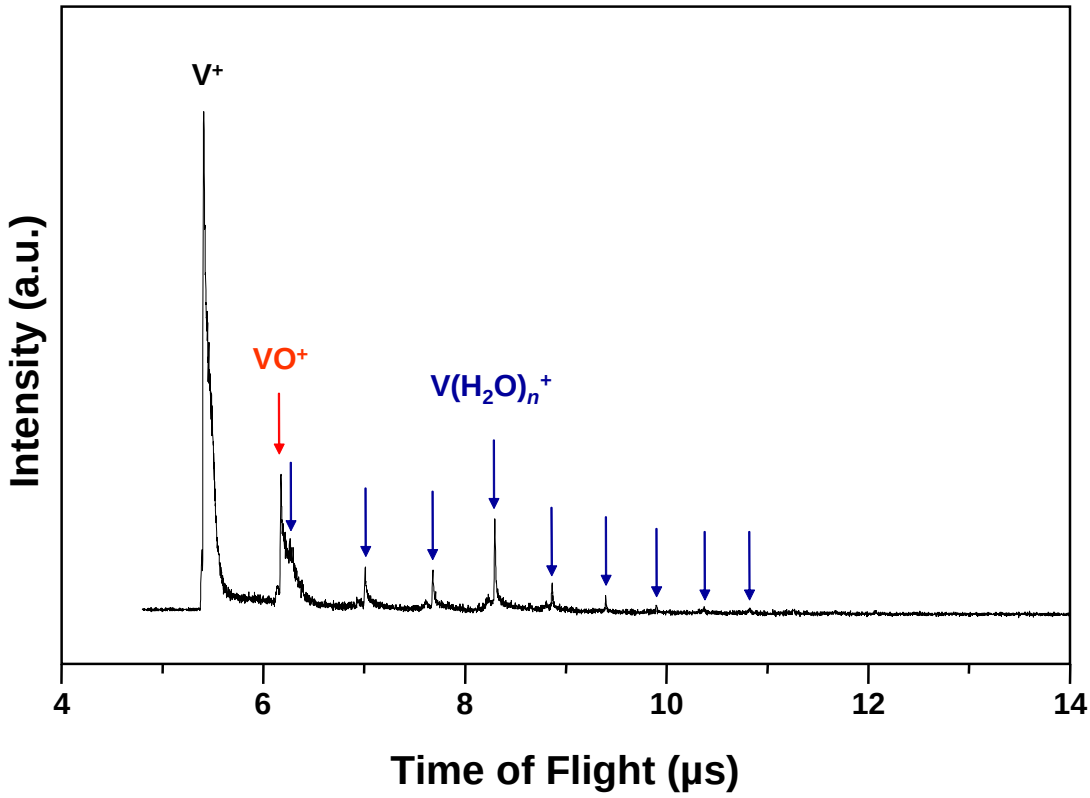

Figure 6.5. Mass spectrum of laser-vaporized vanadium (V) target cooled by He pulse gas at a pressure of 50 atm.

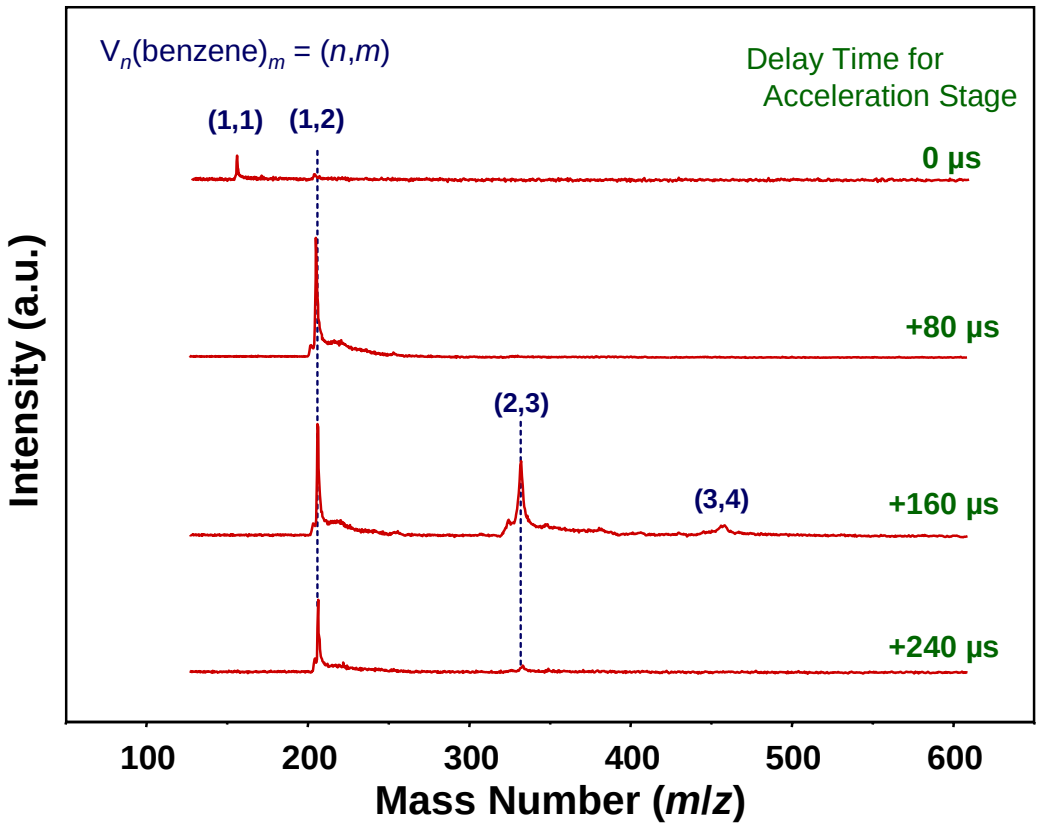

Figure 6.6. The typical mass spectra for the vanadium-benzene complexes obtained by varying the delay time of high-voltage pulse for the acceleration stage.

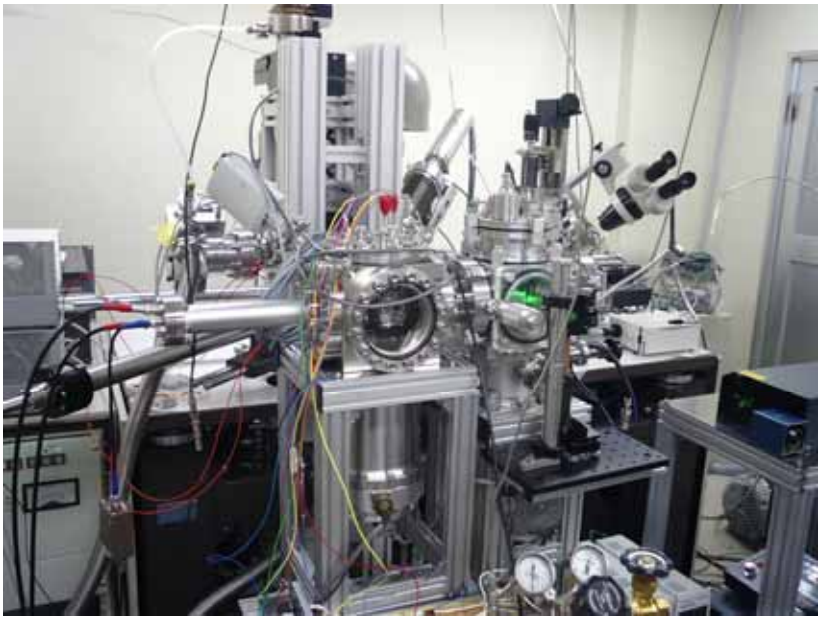

Figure 6.7. Photographic images of the portable cluster source combined with a scanning probe microscopy instrument.

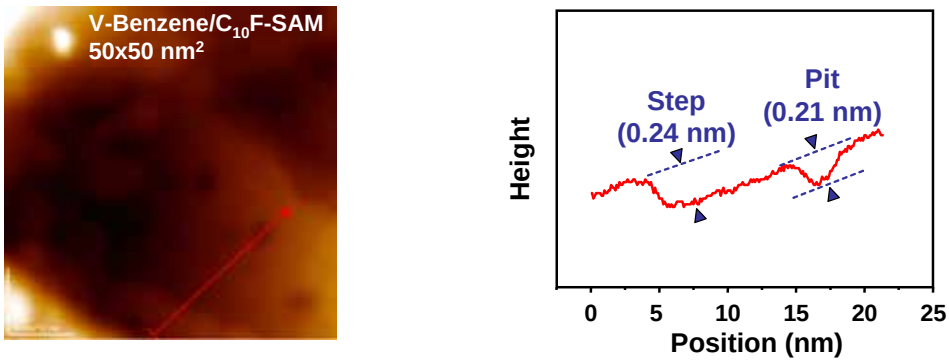

Figure 6.8. Typical topographic image of C_{10}F-SAM measured by NC-AFM and a cross section obtained on red arrow.

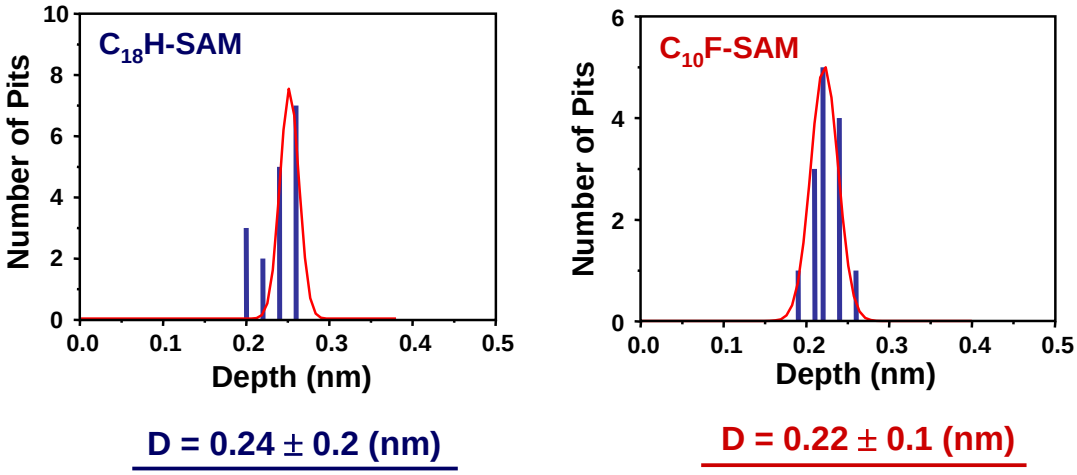

Figure 6.9. The distribution of depth of the depression on several topographic images for C_{18}H-SAM and C_{10}F-SAM matrices.

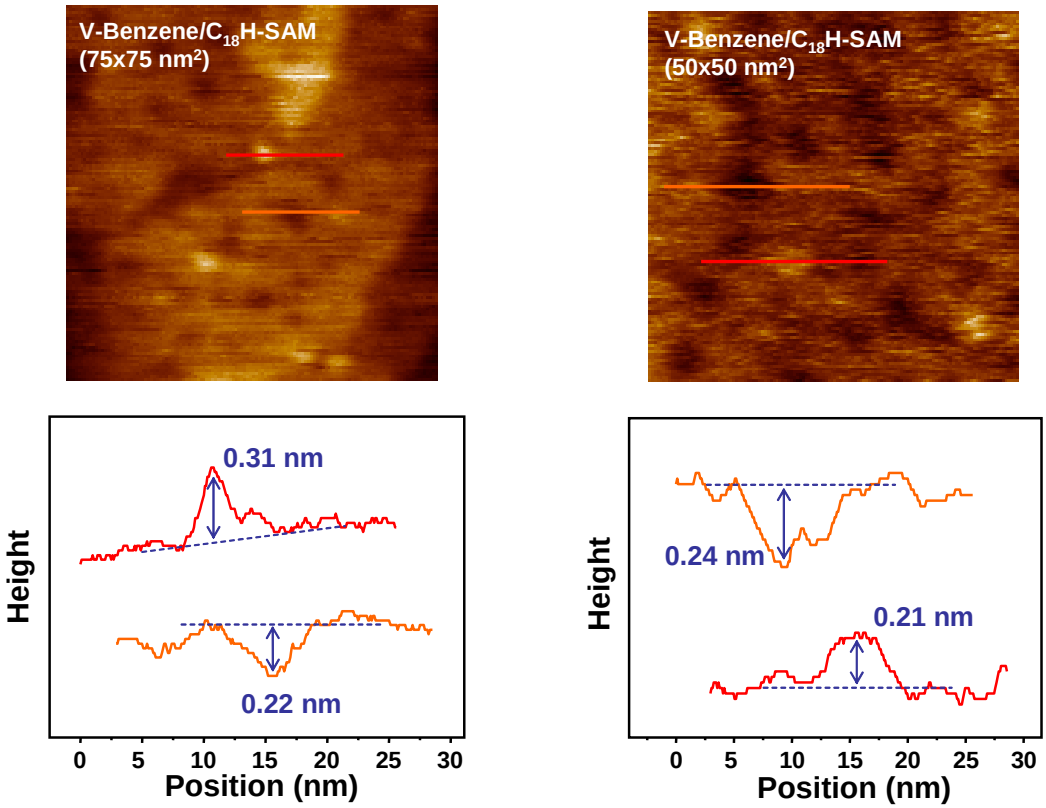

Figure 6.10. Topographic images of V-benzene/C_{18}H-SAM measured by NC-AFM and cross section obtained on red and orange arrow, respectively.

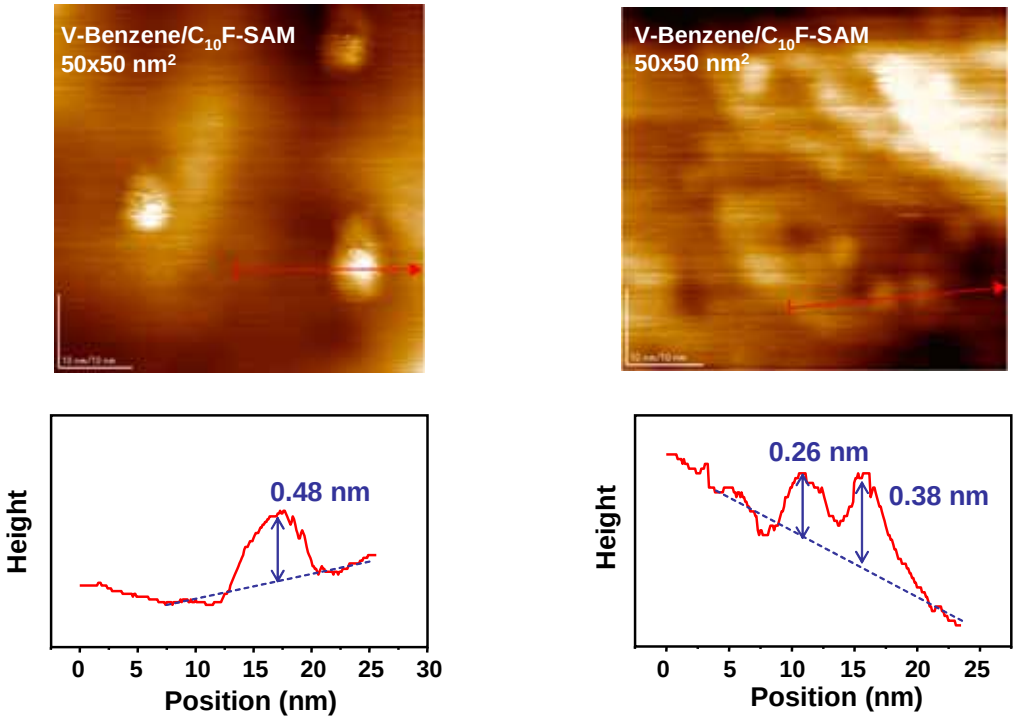

Figure 6.11. Topographic images of V-benzene/C_{10}F-SAM measured by NC-AFM and cross section obtained on red and orange arrow, respectively.

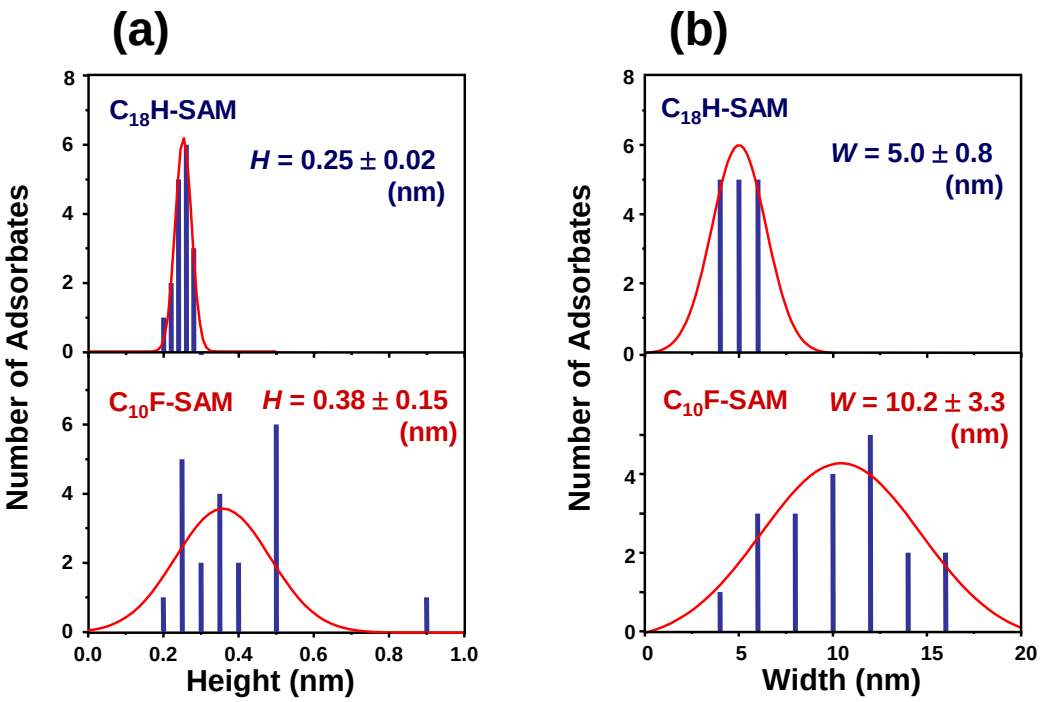

Figure 6.12. The size distribution of bright spots on several topographic images for C_{18}H-SAM and C_{10}F-SAM matrices. Height (a) and width (b) of columnar adsorbates on the SAM matrices are measured, respectively.

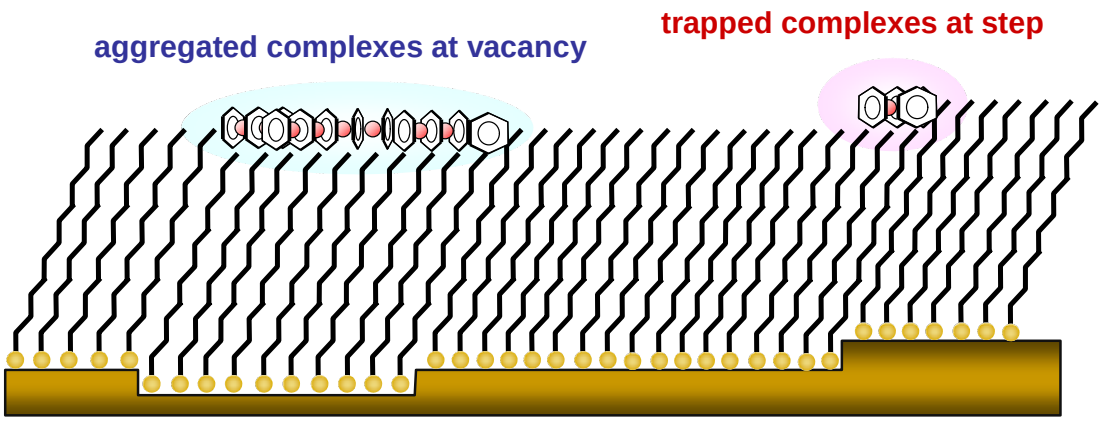

Figure 6.13. The schematic illustration of the adsorption regime of V-benzene complexes on the $C_{18}H$-SAM at room temperature concluded by microscopic studies.

CHAPTER 7

General Conclusions

In this thesis, I have established novel matrix-isolation procedure for gas-phase synthesized clusters by using organic monolayer surfaces as supporting matrices. Among the functional clusters previously synthesized in gas phase, I adopted one-dimensional transition-metal–benzene sandwich complexes for the isolation targets. Soft-landing technique was employed to perform nondissociative deposition of the gas-phase synthesized, size-selected clusters onto the organic surfaces at hyperthermal collision energies of 10–20 eV. The resulting geometry and orientational preference of the matrix-isolated complexes were elucidated by means of infrared reflection absorption spectroscopy. I further discussed the thermal chemistry and thermal stability of the matrix-isolated complexes base on the experimental results of thermal desorption spectroscopy. The individual results are summarized as follow.

Firstly, I developed the soft-landing isolation of gas-phase synthesized transition-metal–benzene complexes of the form $M(benzene)_2$ (M = Ti, V, Cr) onto a series of *n*-alkanethiolate self-assembled monolayers (C_n-SAMs, n = 8, 12, 16, 18, and 22) at hyperthermal collision energy (10–20 eV). The complexes keep their native sandwich structures intact on the SAM matrices even after the hyperthermal collision event and the high incident energy in the soft-landing process results in the penetration of the complexes into the C_n-SAM matrix. The incorporated complexes are highly oriented with their molecular axis canted 70–80° off the surface normal, a phenomenon which is probably due to the attractive CH-π interaction between the capping benzene rings of the complex and the lateral methylene groups of the alkanethiolates. In addition, the adsorption heat of the complexes penetrating into the C_n-SAM increases with the chain-length of the SAM. The $M(benzene)_2$ complexes penetrating into the long-chain SAMs possess unusually large adsorption heats, comparable to a typical adsorption heat of chemisorption (E_d = ~130 kJ/mol), so that the thermal desorption

of the complexes is suppressed, even at room temperature. The thermal deposition of the $Cr(benzene)_2$ complexes are also carried out via physical vapor deposition technique. Thermal deposition of the $Cr(benzene)_2$ complexes makes physisorption of the complexes on the surface of the $C_{18}H$-SAM with a random orientation and small desorprion activation energy (E_d = ~70 kJ/mol). Consequently, it was confirmed that the room-temperature isolation of the sandwich complexes could be successfully provided only after hyperthermal collision event.

Secondly, I elucidated the effect of fluorination of organic monolayer matrices on the resulting soft-landing isolation regime of sandwich complexes. The gas-phase synthesized chromium–benzene 1:2 cation complexes, $Cr^+(benzene)_2$ were size-selectively deposited onto the $C_{10}F$-SAM matrix with the hyperthermal collision energy of 20 eV. The complexes were neutralized even on the fluorinated SAM matrix, and retain their native sandwich structure intact. The hyperthermal collision event in the soft-landing process results in penetration of incoming complexes into the SAM matrix, while the extremely low energy (thermal) deposition (~25 meV) of $Cr(benzene)_2$ complexes via PVD technique poses physisorption of the complexes on a top of the SAM. Although the complexes are weakly physisorbed on the $C_{10}F$-SAM with their molecular axis largely canted to the surface plane, the complexes embedded in the $C_{10}F$-SAM matrix are oriented with their molecular axis approximately perpendicular to the surface. Such orientational preferences is probably due to the repulsive interaction between the π cloud of capping benzene rings of the complex and the outmost CF_3 group and side-chain C-F groups of the fluorocarbon axes of the $C_{10}F$-SAM matrix, respectively. In addition, the complexes penetrating into the SAM matrix exhibits unusual large activation energy for desorption of over 190 kJ/mol, with the result that the thermal desorption of the complexes can be suppressed over room temperature. It can be conclude

that the orientaional preference as well as thermal stability can be control well by modification of organothiolates forming the SAM matrices.

Thirdly, I endeavored the matrix-isolation of multiple-decker V_2(benzene)$_3$ complexes and successfully achieved the isolation of the complexes in the C_{18}H-SAM matrix. The infrared spectrum of the multiple-decker V_2(benzene)$_3$ complexes are obtained for the first time by use of the IRAS measurement. An agreement of the obtained IRAS spectrum with calculated IR spectrum demonstrates that the V_2(benzene)$_3$ complexes retain their one-dimensional multiple-decker structure intact. Thermal desoption study reveals that the matrix-isolated V_2(benzene)$_3$ complexes resist the thermal desorption up to a high temperature of ~350 K. The achievement of soft-landing isolation of gas-phase synthesized multiple-decker V_2(benzene)$_3$ sandwich complexes, presented in this study, with high thermal stability is anticipated to open up new possibilities for exploiting these complexes as molecular-scale photo-magnetic building blocks in applications for future cluster-based materials.

Finally, I designed the portable cluster source equipped with a quadrupole deflector and TOF-MS system. The small packed TOF-MS system provides mass spectra with a sufficient resolution ($m/\Delta m$ = 200) to analyze the mass distribution of typical clusters by use of three acceleration stages. The microscopic studies of the C_{10}F- and C_{18}H-SAM substrates after soft-landing of V-benzene complexes are performed by combining the portable cluster source into the SPM instrument. The soft-landed complexes are forming the columnar islands at the vacancy island of the SAM surface at room temperature. Change in island size between the C_{10}F-SAM and C_{18}H-SAM matrices is observed, a result which may be reflecting the differences of the activation barrier for the thermal diffusion of the complexes between on the two SAM matrices.

As stated above, I have established a new matrix-isolation procedure for gas-phase synthesized clusters by use of organic monolayer surfaces as supporting matrices. It is the first demonstration of trapping the gas-phase clusters with their native structures intact on a solid surface around room temperature or above. For the transition-metal–benzene sandwich complexes, orientaional preference as well as thermal stability can be controlled by varying the organic molecules forming the organic monolayer, a finding which will provide a possibility to finely-tune the functionality, i.e. optical and magnetic response of the cluster-assembled surfaces.

In closing, I would like to prospect new directions of promising researches based on my doctoral works. Soft-landing isolation technique presented in this study will open up a new field, where the gas-phase synthesized, various kind of clusters can be characterized by suitable conventional and advanced surface science techniques to evaluate their potential ability for functional materials. The greatest advantage of the newly established soft-landing isolation is that the gas-phase clusters can be extracted onto substrates *as it is* with high thermal stability, the clusters, therefore, can retain their original properties elucidated in gas phase even in the matrix-isolated state. Thus, substances, which is newly brought about by gas-phase chemistry, can be given the opportunity to be the candidates considered for nanostructured advanced materials by means of soft-landing isolation technique.

CHAPTER 8

Bibliography

Papers

1. Nagaoka, S., Okada, E., Doi, S., Mitsui, M., and Nakajima, A.

   Trapping of V(benzene)$_2$ Sandwich Clusters in a *n*-Alkanethiol Self-Assembled Monolayer Matrix

   European Physical Journal D, Vol.34, No.1–3, pp. 239–242, (2005).

2. Nagaoka, S., Matsumoto, T., Okada, E., Mitsui, M., and Nakajima, A.

   Room-Temperature Isolation of V(benzene)$_2$ Sandwich Clusters via Soft-Landing into *n*-Alkanethiol Self-Assembled Monolayers

   The Journal of Physical Chemistry B, Vol.110, No.32, pp. 16008–16017, (2006).

3. Mitsui, M, Nagaoka, S., Matsumoto, T., and Nakajima, A.

   Soft-Landing Isolation of Vanadium-Benzene Sandwich Clusters on a Room-Temperature Substrate Using *n*-Alkanethiolate Self-Assembled Monolayer Matrixes

   The Journal of Physical Chemistry B, Vol.110, No.7, pp. 2968–2971, (2006).

4. Nagaoka, S., Matsumoto, T., Ikemoto, K., Mitsui, M., and Nakajima, A.

   Soft-Landing Isolation of Multidecker V_2(benzene)$_3$ Complexes in an Organic Monolayer Matrix: an Infrared Spectroscopy and Thermal Desorption Study

   Journal of the American Chemical Society, Vol.129, No.6, pp. 1528–1529, (2007).

5. Nagaoka, S., Ikemoto, K., Matsumoto, T., Mitsui, M., and Nakajima, A.

   Thermal and hyperthermal collision-energy depositions of transition-metal–benzene sandwich complexes onto an *n*-octadecanethiol self-assembled monolayer

   [submitted to The Journal of Physical Chemistry C].

Presentations at International Conferences

1. Nagaoka, S., Matsumoto, T., Mitsui, M., and Nakajima, A.

   "Soft-Landing Isolation of Organometallic Sandwich Clusters in Self-Assembled Monolayer Matrices"

   ISSPIC 13 (XIII International Symposium on Small Particles and Inorganic Clusters)

   July 2006, Göteborg (Sweden).

2. Nagaoka, S., Matsumoto, T., Mitsui, M., and Nakajima, A.

   "Soft-Landing Isolation of Organometallic Sandwich Clusters in Self-Assembled Monolayers: Adsorption State and Desorption Kinetics of the Supported Clusters"

   ICCS 2006 (International Symposium on Clusters at Surfaces)

   May 2006, Warnemünde (Germany).

3. Nagaoka, S., Matsumoto, T., Mitsui, M., and Nakajima, A.

   "Soft-Landing of One-Dimensional Organometallic Clusters onto a Self-Assembled Monolayer Matrix"

   PACHIFICHEM 2005

   December 2005, Hawaii (USA).

4. Nagaoka, S., Matsumoto, T., Mitsui, M., and Nakajima, A.

   "Soft-Landing of Vanadium-Benzene Sandwich Clusters onto *n*-Alkanethiol Self-Assembled Monolayers"

   JST-JIS-NDS (Japan Science and Technology Agency Joint International Symposium on Creation of Nanoscale Designed Surface and their Electronic and Catalytic Properties)

   September 2005, Tokyo (Japan).

5. Nagaoka, S., Matsumoto, T., Mitsui, M., and Nakajima, A.

   "Thermal Stability of V(benzene)$_2$ Sandwich Cluster on Self-Assembled Monolayer"

ISSPIC 12 (XII International Symposium on Small Particles and Inorganic Clusters)

September 2004, Nanjing (China).

Presentations at Domestic Conferences

Talks

1. Nagaoka, S., Ikemoto, K., Mitsui, M., and Nakajima, A.

   "Soft-Landing Isolation of Organometallic Sandwich Clusters in Organic Monolayer Matrices"

   The 1st Symposium on Molecular Science

   September 2007, Sendai.

2. Nagaoka, S.

   "Development of Soft-Landing Isolation Technique by Use of Origanic Monolayer Matrices"

   Symposium on Advanced Laser Spectroscopy for Young Scientists

   December 2006, Yokohama.

3. Nagaoka, S., Matsumoto, T., Mitsui, M., and Nakajima, A.

   "Desorption Kinetics and Adsorption State of Gas-Phase Clusters Soft-Landed on a Self-Assembled Monolayer Surface"

   The 86th Spring Meeting of the Chemical Society of Japan

   March 2006, Chiba.

4. Nagaoka, S., Matsumoto, T., Mitsui, M., and Nakajima, A.

   "Soft-Landing Isolation of Organometallic Cluaters in Long-Chain Alkanethiolate Self-Assembled Monolayers"

   General Symposium on Molecular Structures (Bunshi-Kouzou-Sougo-Touron-Kai)

September 2006, Tokyo.

Posters

1. Nagaoka, S., Ikemoto, K., Mitsui, M., and Nakajima, A.

   "Soft-Landing Isolation of Gas-Phase Synthesized Clusters in Organic Monolayer Matrices"

   The 5th Annual Meeting of Society of Nano Science and Technology

   May 2007, Tsukuba.

2. Nagaoka, S., Matsumoto, T., Mitsui, M., and Nakajima, A.

   "Adsorption States and Thermal Stability of Organometalic Clusters Soft-Landed on a Self-Assembled Monolayer Surface"

   General Symposium on Molecular Structures (Bunshi-Kouzou-Sougo-Touron-Kai)

   September 2006, Shizuoka.

3. Nagaoka, S., Matsumoto, T., Mitsui, M., and Nakajima, A.

   "Chain Length Effect of Alkanethiol Self-Assembled Monolayers on Thermal Stability and Orientation of Organometallic Sandwich Clusters"

   The 3rd Annual Meeting of Society of Nano Science and Technology

   May 2006, Sendai.

4. Nagaoka, S., Okada, E., Doi, S., Mitsui, M., and Nakajima, A.

   "Adsorption and Desorption Dynamics of Organometallic Clusters on Solid Surfaces"

   The 20th Symposium on Chemical Kinetics and Dynamics

   July 2005, Tokyo.

Academic Awards

2005 Young Best Presenter Award

The 3rd Annual Meeting of Society of Nano Science and Technology

2006 CSJ Student Presentation Award

The 86th Spring Meeting of the Chemical Society of Japan

2007 Fujihara Award

Fujihara Scholarship Foundation of Keio University